Fabrication of in-situ MgB2 thin films on Al2O3 substrate using off-axis PLD technique

Yi Sun Wu
University of Wollongong

Fabrication of *in-situ* MgB_2 thin films on Al_2O_3 substrate using off-axis PLD technique

A thesis submitted in partial fulfillment of the requirements
for the degree of

Master of Science
by Research

from

University of Wollongong

by

Yi Sun Wu

at

Institute for Superconducting and Electronic Materials

Faculty of Engineering

August 2007

CANDIDATE'S CERTIFICATION

I hereby declare that the research for this submission was carried out by the candidate at Institute for Superconducting and Electronic Materials, the Faculty of Engineering, the University of Wollongong, is wholly my own work unless other wise referenced or acknowledged. The document has not been submitted for any other academic institution.

Yi Sun Wu

31st July, 2007

Acknowledgement

First of all, I would like to express my sincere appreciation and gratitude to my supervisors, Prof. Dou and Dr. Y. Zhao, for their instructions and supports through out my Master study. They provided invaluable guidance, constant encouragement and support throughout the course of this thesis work.

The Australian Research Cuncil (ARC), the University of Wollongong and the Institute for Superconducting & Electronic Material provided financial support to the research work and my stipend.

Special thanks are due to Dr. David Wexler, Dr. Alexey Pan, Dr K. Konstandinov and Dr. Joseph Horvat for their work on training and helps in the usage of XRD, MPMS, SEM, PPMS facilities. TEM specimens were prepared by Dr C. Kong at UNSW. I also want to thank Dr Tania for her help in my English scientific writing skill. She has proof read every single piece of my thesis.

Contents

Abstract

In Chapter 1, I briefly discuss some fundamental theories and the history of superconductivity. A few examples are given for superconductor applications. At Chapter 2, a literature review of MgB_2 is presented, with some discussion on its discovery, as well as the current research on this binary superconductor. In Chapter 3, the experimental system and other types of laboratory measurement and analysis equipment are introduced, such as those used for critical temperature T_c and critical current J_c measurements, microstructural analysis using X-ray Diffraction (XRD), Scanning Electron Microscopy (SEM), etc. From Chapter 4 through Chapter 7, various ways of improving the fabrication of MgB_2 thin films are discussed along with the corresponding results.

In Chapter 4, I first report investigations on the vacuum level and background pressure in order to create an optimised environment inside the chamber for the pulsed laser deposition (PLD) of MgB_2 thin films on Al_2O_3 (Sapphire) substrates. I found that a vacuum of 9×10^{-8} Torr inside the deposition chamber was necessary before deposition to generate a stronger plasma of the ablating materials, but that a high purity argon background gas had to be introduced up to a pressure of 120m Torr to fabricate high quality MgB_2 thin films. This result was employed in the experiments in the rest of this report.

In Chapter 5, the effects of changing the annealing parameters, time (τ_{ann}) and temperature (T_{ann}), are reported. The combined results from T_c measurements and

XRD showed that the films with longer dwell times, up to 9 minutes at a moderate sintering temperature, have higher T_c and better crystal growth. We found that for films sintered at 700 °C, critical current densities, J_c, as high as 2×10^{-6} Acm^{-2} were achieved at 10K and 0.5T. However, J_c drops as the magnetic field increases. It is proposed that the improved J_c in low fields was due to the fine grains and enhanced density of the sample.

In Chapter 6, I discuss the fabrication of MgB_2 thin films with the addition of elemental Si. Silicon is a semiconductor and is very reactive with Magnesium to form Mg_2Si, which can act as a source of pinning centres in our thin films, making it possible to improve the J_c dependence in magnetic field. The drawback of this is higher resisitivity and weaker grain connectivity, so a moderate amount of Si addition must be chosen. Also, the Si was added by using a switching target mechanism which will produce thin films of partial multilayer structures. Although the time for the Si deposition was short, the Si layers embedded in between the MgB_2 layers were thin and usually broke during a high temperature sintering process. However, the defects which formed in between these layers generally had a two dimensional structure and their effect on the pinning properties due to this geometry is also discussed. A film with about 5 wt% of Si added was observed to have slightly decreased T_c and weaker field dependence.

List of Figures

List of tables

Introduction

High temperature superconductors (HTS) are in demand for various applications, owing to their physical properties, which allow them to work in higher temperatures and thus save much of the power that is consumed in the cooling systems in most electronic devices. Magnesium diboride (MgB_2) is a newly discovered HTS superconductor (although some researchers prefer to call it a Medium Temperature Superconductor) that has attracted ongoing international effort from scientists and researchers towards investigating it. MgB_2 superconductor has amenable physical properties that hold great potential for its application in superconducting electronic devices, when compared to other materials currently in use as superconducting circuit elements. MgB_2 has been revealed as a phonon-mediated superconductor similar to niobium, but its higher transition temperature, T_c, larger energy gap, and relatively longer coherence length are the promising features making it more favourable for use in most superconducting circuits.

Since its superconducting properties were discovered, it has been suggested that MgB_2 can play an important role in active and passive high frequency electronic devices. Its large coherence length and moderately high critical temperature make it a suitable candidate for stable Josephson junctions, which are the fundamental elements for a wide range of superconducting electronic, including highly magnetic-field sensitive superconducting quantum interference devices (SQUIDs). These devices are currently made from niobium, but it must be cooled with liquid helium to about 4K, which requires very high power consumption on cryogen cooling. The significant

advantage of the high 39K T_c of MgB_2 is that it enables electronics to operate at 20 − 25K, which is achievable by compact coolers.

Thin film synthesis is the fundamental step to the realization of electronic devices. However, there are difficulties in the preparation of MgB_2 thin films, with these problems including the high volatility and high reactivity with oxygen of Magnesium, so that MgB_2 films deposited under current technology have reduced transition temperatures and poor crystalline structure, or require *ex-situ* annealing in Mg vapour. Various methods for the preparation of MgB_2 have so far been used, and MgB_2 thin films with T_c close to that of bulk have been reported e.g [1] in previous experiment using *ex-situ* annealing deposition, but the technical drawback is that the films obtained under *ex-situ* annealing conditions have a strong critical current, J_c, field dependence and lack the multilayer structure which is necessary for MgB_2 Josephson junctions.

We therefore focus on the *in-situ* annealing PLD method, although the films generated have so far shown a considerable suppression in T_c, which for these films is between 25 − 30K. Although the T_c requires improvement, the PLD films created by *in-situ* annealing appear to be more attractive due to the comparatively simple equipment used, which is technically capable of implementing multilayer structures for Josephson junctions. Previous studies in our group have proved that the suppressed T_c is due to contamination of Mg with oxygen and incomplete crystallization of the film [2, 3]. Yet recent developments have shown that the $T_{c\ \mathrm{onset}}$ of the *in-situ* annealed films can be improved to 34.5K along with a combination of

good superconducting properties. According to a comparative study between different preparation methods, the *in-situ* film has much higher disorder, providing stronger electron scattering [4]. This effectively reduces the temperature dependence of the critical magnetic field density and raises the critical current performance. Several types of MgB_2 have already been tested. The results show the attractive potential of MgB_2 films, but there are still problems, such as T_c suppression, the effects of impurities, and the influence of grain structure and microstructure associated with the material preparation conditions, which need to be investigated and modified before MgB_2 thin films can be applied to electronic devices. In this project, we set out to address these problems by systematic investigations and have tried to contribute to a solid material basis on which practicable MgB_2 electronic devices can be developed.

Reference

[1] W. N. Kang, et al., "MgB_2 Superconducting Thin Films with a Transition Temperature of 39 Kelvin," *Science,* vol. 292, pp. 1521-1523, 2001.

[2] Yue Zhao, Mihail Ionescu, Josip Horvat, and S. X. Dou, "Comparative study of in situ and ex situ MgB_2 films prepared by pulsed laser deposition," *Supercond. Sci. Technol. ,* vol. 17, pp. S482–S485, 2004.

[3] Yue Zhao, Mihail Ionescu, Alexey V Pan, Shi Xue Dou, and E. WCollings, "*In situ* annealing of superconducting MgB_2 films prepared by pulsed laser deposition," *Supercond. Sci. Technol. ,* vol. 16 pp. 1487–1492, 2003.

[4] Yue Zhao, Mihail Ionescu, J. Horvat, and S. X. Dou, "Off-axis MgB_2 films using an *in situ* annealing pulsed laser deposition method," *Supercond. Sci. Technol.,* vol. 18, pp. 395–399, 2005.

Chapter 1

Introduction to superconductivity and its applications

1.1 History of the discovery of superconductors

In 1911, while the Dutch Physicist H. Kamerlingh Onnes, who first succeeded in liquefying helium, was investigating the properties of materials at liquid helium temperatures, he discovered that there was a certain temperature, called the *critical temperature,* T_c, below which the electrical resistance of mercury became zero and the conductivity, the inverse of the resistivity, $\sigma = 1/\rho$, tended to infinity. He gave this phenomenon the name *superconductivity* [1]. The critical temperatures for other superconducting elements were later found to vary from less than 1K to tens of Kelvin.

1.2 Fundamentals of superconductivity theory

In the presence of an applied magnetic field B_a, the critical temperature of a superconductor is lower than when there is no field. As the applied field is increased, T_c decreases. When the applied field reaches a certain critical value B_c, the critical temperature T_c becomes zero, which means that the superconducting state does not exist at any temperature and superconductivity has been completely destroyed. The conductivity of a superconductor can not be defined since it has zero resistance $\sigma = 1/\rho$ ($\sigma \to \infty$, $\rho \to 0$). However, currents have been observed to flow for many years

without loss in superconducting rings. Such a current is called a “supercurrent”, and some characteristic factors associated with supercurrents are described briefly in the following sections.

1.2.1 The superconducting electrons – Cooper pairs

When a metal is cooled below the critical temperature, there is a mechanism in which the free electron gas that characterizes the normal state transforms itself into a quantum fluid of coherent electron pairs in the reciprocal space. Each individual pair is formed when one electron of a given momentum and spin couples with another electron of exactly the opposite momentum and spin giving a net momentum of zero. These charge carriers are called the “Cooper pairs”.

1.2.2 Coherence length

The flow of a Cooper pair can be visualized in terms of the first electron traveling through a lattice space consisting of a region of positive ions (Fig. 1-1a). The first moving electron creates a slight distortion of the lattice. The distortion increases the density of positive ions in that region (Fig. 1-1b), and the cloud of positive charge relaxes slowly, therefore attracting the second following electron towards the first electron [2].

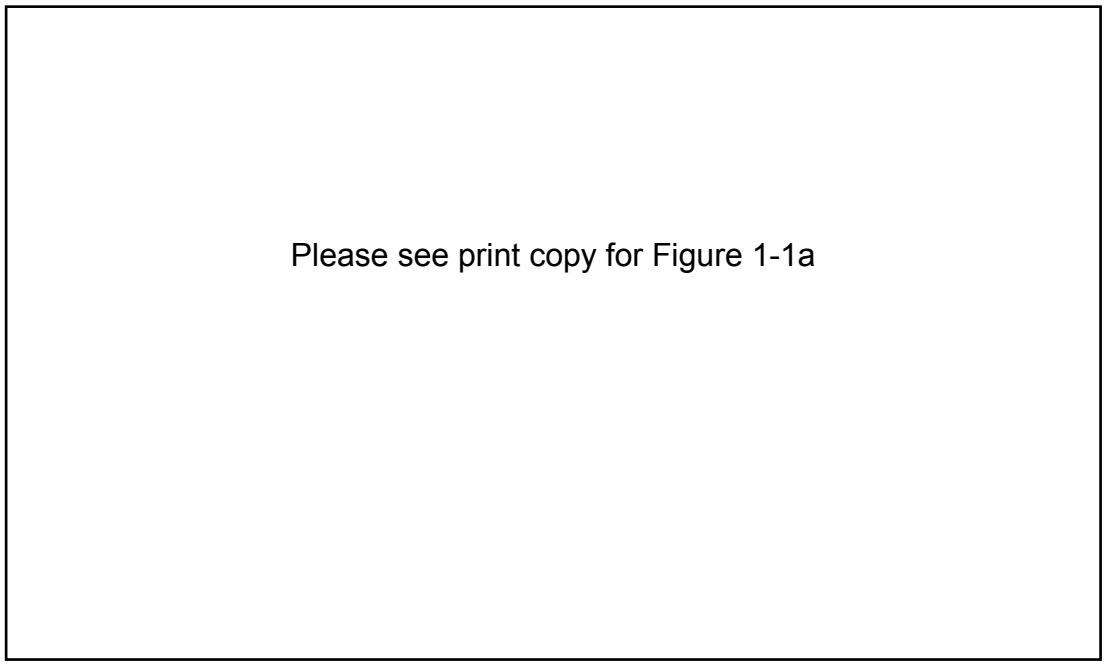

Fig. 1-1a The metal structure considered to be a lattice of cations through which delocalized electrons can flow.

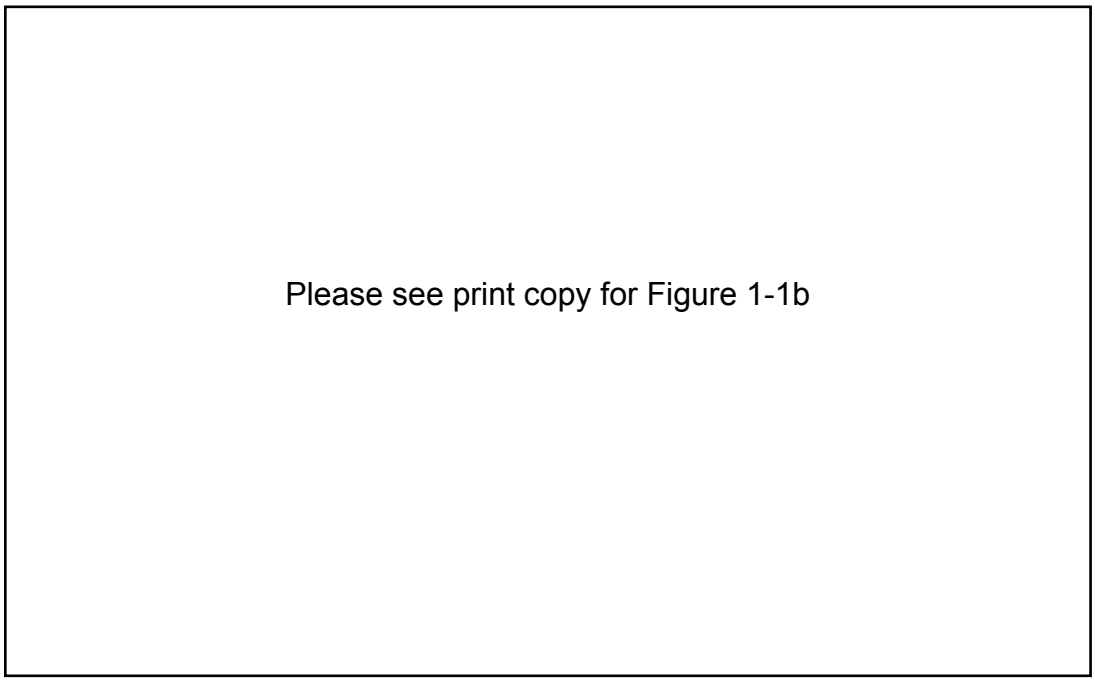

Fig. 1-1b A concentrated region of positive charge that will propagate along the lattice through interaction with the electron. Both figures cited from [2].

The distance between the two electrons in a Cooper pair is generally called the "coherence length ξ", which has a value varying between a few hundreds to more than

ten thousand angstroms in metals. The partners in the Cooper pair are only a few angstroms away from the nearest electrons in other pairs. This makes the mechanism of such a fluid flow different from that of the normal electron gas. However, be aware that the term "coherence length" also denotes the characteristic length ξ_{GL} over which the Ginsburg Landau (GL) order parameter Φ varies without an appreciable energy change, as well as the size of the radius of the core of a vortex, ξ_R.

The coherence length ξ is the first fundamental length scale derived from GL theory [3, 4]:

$$\xi^2(T) = \frac{\hbar^2}{2m^* a(T)} \ .$$

Where m^* is the mass of a superconducting electron in a Cooper pair and $a(T)$ is a temperature dependent parameter in the GL equation

$$a(T) \approx a_0[(T/T_c)\text{-}1] \ .$$

1.2.3 Superconducting state of metals

In the quantum phenomenon of superconductivity, the net momentum is zero, since the two electrons in each Cooper pair have opposite momenta and spins. The associated wavelength is infinite by the de Broglie equation, $\lambda = \hbar/p$, but typically the wavelength is of the order of the sample size. De Broglie had proposed that normal conduction electrons with the Fermi velocity v_F are scattered by impurities or lattice imperfections. The resistivity is related to the electron mean free path l_e between two scattering events by $\rho = mv_F/ne^2l_e$, where mv_F is the Fermi momentum p_F of the

electron and *n* the electron density. However, this is certainly not the case for Cooper pairs, since there is no momentum associated with them and hence there is no mechanism which could give rise to resistivity. Such a material is thus defined to be in its superconducting state [4].

1.2.4 The Meissner-Ochsenfeld Effect

In 1933, H. W. Meissner and R. Ochsenfeld discovered that when a superconductor is cooled to below its critical temperature under a certain external magnetic field, the field lines are expelled from the interior of the superconductor and thus the applied field inside the superconductor is zero [5, 6]. This effect was named the *Meissner effect* and was known to occur because the screening current induced on the surface by the external field generates an interior field which flows in a direction such as to exactly cancel the applied field within the material. But it does not occur in a perfect diamagnet in the normal state. The Meissner effect is also recognized as a factor that determines whether a material is a superconductor.

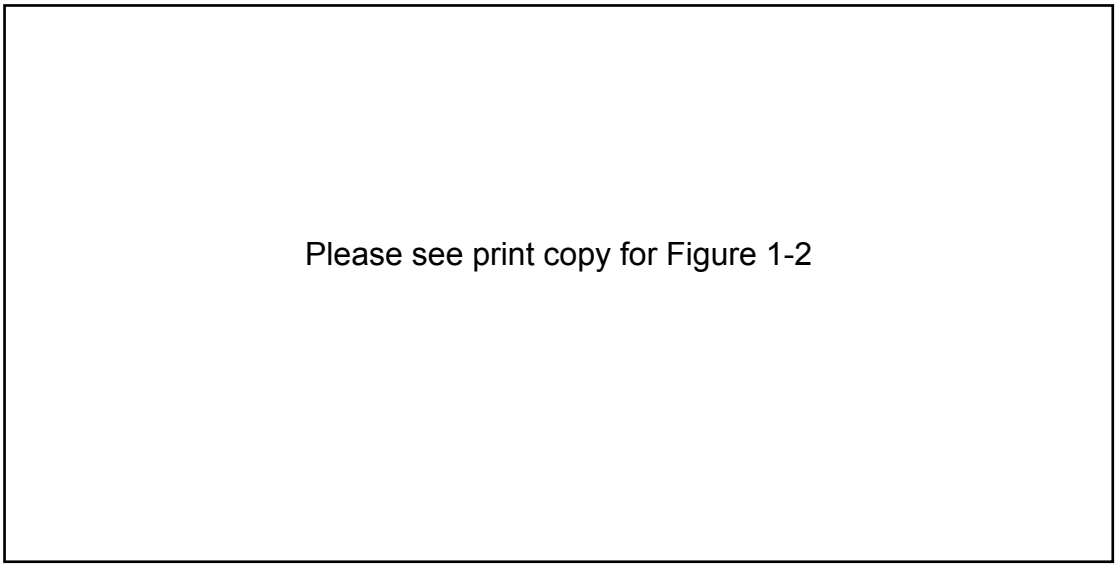

Fig.1-2 Meissner effect exhibits the repulsion of external flux from the core [6].

One simple experiment to demonstrate the Meissner effect in a laboratory is to place a small permanent magnet on the surface of a superconductor sample. If the superconductor is not cooled or the sample is a perfect conductor the magnet will sit there forever with its magnetic field penetrating into the sample, as no electrons will undergo the necessary phase change. However, if the superconductor sample is cooled to below its T_c, electric current will run on the surface of the sample creating an opposing magnetic field that interacts with the existing field from the magnet. By doing so, a repulsive force is generated to cancel out the field in the interior of the sample, and the small magnet is seen to be levitated as shown in Figure 1-2 below.

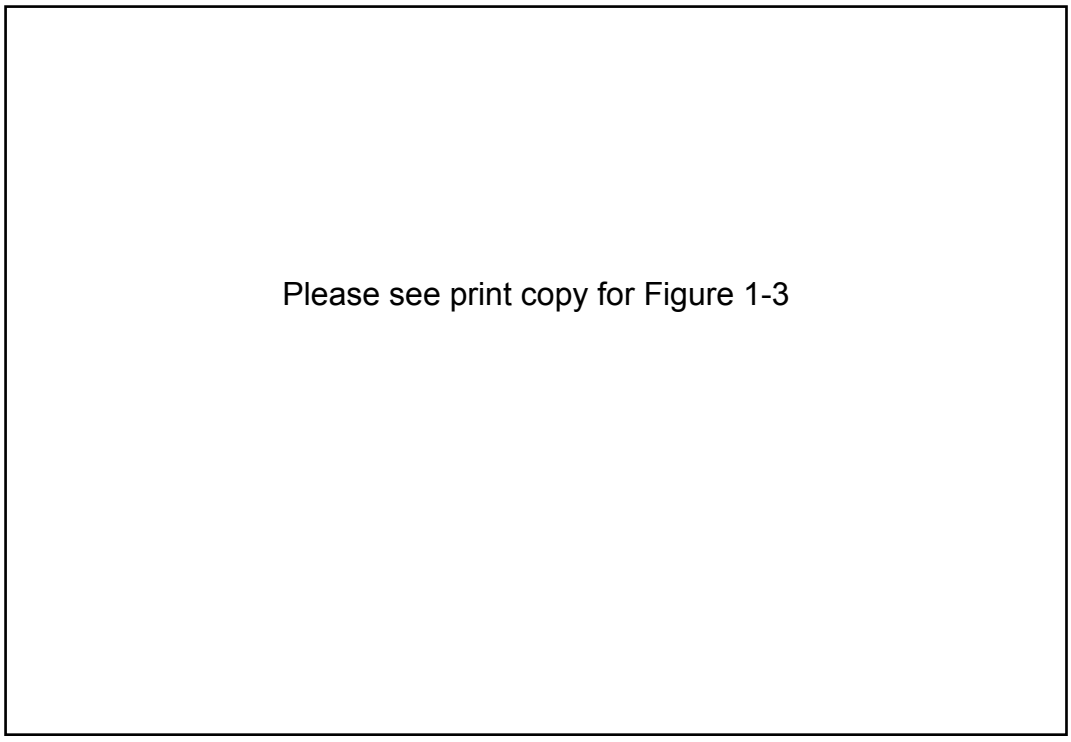

Fig.1-3 A Magnet is levitated from the surface of a cooled superconductor due to magnetic field expulsion. Figure cited from [5].

1.2.5 The London penetration depth

The Meissner effect means that no flux can penetrate under the surface of a superconductor provided that the external field is below a critical strength. Yet this seems to require the supercurrent to flow in an infinitely thin layer under the surface of a superconductor in a complete state $M + H = 0$, which is not the case. In fact, the flow of supercurrent which gives rise to magnetization is confined to flow within a certain depth of the superconductor, and this is called the London penetration depth, λ, of the magnetic field. A magnetic field $B(x)$ applied in a perpendicular direction to the surface and the current density $J(x)$ accordingly obey exponential decay with the distance x inside the surface of a superconductor [3]

$$B(x) = B_0 e^{-x/\lambda}$$

$$J(x) = J_c e^{-x/\lambda}.$$

The London penetration depth is regarded as the second fundamental length scale in GL theory [3, 7]:

$$\lambda^2 = \frac{m^*}{\mu_0 e^{*2} \Phi^2} = \frac{m^*}{\mu_0 e^{*2} n_s} \ .$$

Where e^* is the superelectron charge and the square of the GL order parameter $\Phi(\underline{r}) = \Phi e^{i\Theta}$ equals the supercurrent electron density:

$$\Phi(\underline{r})^2 = \Phi^2 = n_S \ .$$

1.2.6 Ginsburg Landau parameter

The London penetration depth λ together with the coherence length ξ defines the Ginzburg-Landau parameter $\kappa = \lambda/\xi$ [4, 8], and the critical value $\kappa = 1/\sqrt{2}$ splits superconductors into two types:

$$\kappa \leq 1/\sqrt{2} (Type 1)$$
$$\kappa \geq 1/\sqrt{2} (Type 2)$$

The Ginzburg-Landau parameter is one of the characteristics of a superconductor.

1.3 Type-I and Type-II superconductors

Type I superconductors are pure metals. These usually have a very low critical field and will be useless in applications which require operation in high magnetic fields, such as the construction of superconducting magnets. Metal alloys and the element niobium are examples of type II superconductors, which have two critical fields: the lower, B_{c1}, and the upper, B_{c2}. Their magnetization curve exhibits a more complex dependence on the external magnetic field. For both types, the areas under their *M*-*B* curves are the same. This is how one can obtain the thermodynamic critical field B_c in type II superconductors. It is related to the product of B_{c1} and B_{c2} by:

$$B_{c1} B_{c2} = B_c^2 \ln \kappa$$

where κ is the Ginzburg-Landau parameter described in the last section [4]. The value of B_c does not vary much in type II superconductors in low magnetic fields. This implies that in high T_c superconductors, the higher the B_{c2}, the lower the B_{c1}.

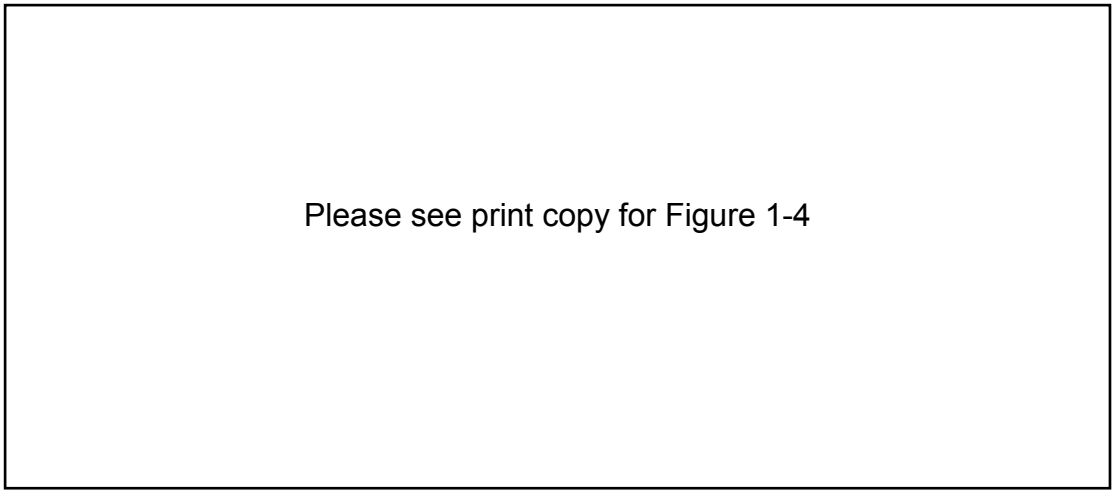

Fig.1-4 Change of magnetization inside type I and type II superconductors under an applied field B_a. Figure cited from [8].

Moreover, only type I superconductors, which are primarily pure metal elements, exhibit the complete Meissner effect. Alloys and metals which have large resistivity in the normal state and partially exhibit the Meissner effect under an external field $B_{c1} < B_a < B_{c2}$ are type II superconductors.

1.3.1 Destruction of superconductivity by magnetic field and current

In the superconducting state below T_c some magnetic energy is lost to the expulsion of the magnetic flux. If the external field B_a continues to increase up to a point where the loss in magnetic energy outweighs the gain in condensation energy E_{cond} from the phase transition into the superconducting state, the superconductor will become only partially superconducting (type II) or return to its normal state (type I). The condensation energy is expressed as the energy released per unit volume by transforming normal electrons into Cooper pairs [3, 4]

$$E_{cond} = B_c^2/2\mu_0$$

Similarly, excessive current passing through the material will also create a magnetic field larger than the critical field around the surface and destroy the superconducting state. This limits the maximum current flow per unit area that the material can sustain. The key to magnet applications of superconductors lies within high critical fields and current densities.

1.3.2 Mixed state in type II superconductors

'Mixed state' refers to the partial superconductivity described in the last section for a type II superconductor which exhibits two critical magnetic fields, B_{c1} and B_{c2}. Total flux cancellation occurs only if the external field B_a is less than B_{c1}. However, if B_a is increased between B_{c1} and B_{c2}, the external field partially penetrates into the material, with the field lines confined to tubes called *flux tubes* or *vortices*. The volume confined within each vortex has normal resistivity, but the surrounding region is still in the superconducting state and free of resistivity. As the external field B_a becomes larger, the vortices become more closely spaced, until they overlap when the external field B_a eventually exceeds the upper critical field $B_{c2.}$ When $B_a > B_{c2,}$ all of the material returns to its normal state. At any temperature below T_c, type I superconductors undergo a first order phase transition from the superconducting to the normal state at B_c, whereas that is a second order transition for type II superconductors. In the type II case for $B_a < B_{c2}$, the GL equation describing the motion of a Cooper pair $q = 2e$ in the magnetic field is limited to first order in its

parameter Φ, and by taking the lowest energy state of this equation, the value of *a(T)* can be expressed in terms of the upper critical field:

$$\frac{e\hbar B_{c2}(T)}{m^*} = -a(T) \ .$$

By substituting *a(T)* into the first length scale ξ, a relation between upper critical field B_{c2} and coherence length ξ can then be found [4, 7]:

$$B_{c2}(T) = \frac{\Phi_0}{2\pi} \frac{1}{\xi^2(T)} \ .$$

Φ_0 represents the quantum of flux transported by each vortex,

$$\Phi_0 = h/2e.$$

1.4 General applications of superconducting thin films

It is essential to realize that there are problems in studying thin films before we produce the films. The structure and properties of thin films are known to be highly dependent on the surface of the substrate on which they are deposited. This is especially true for the films in this work, which have an average thickness around 500nm. The physical properties of films are to a large extent attributable to the influence of the state of the substrate, such as the density of imperfections that exists inside the substrate and whether any gas is absorbed into the substrate through molecular interactions. In this report, I shall briefly review the basics of the film preparation methods by which our films were produced and how the properties and structures of films were examined, with discussions on the respective merits of these preparation methods. The applications of superconductors are described in most standard textbooks [9], so I here list only one thin film application.

1.4.1 Josephson junction

The research on thin film applications is mostly in the field of superconducting electronics, which is one of the most important areas where superconductivity based technology is being developed. These applications are mainly based on constructing Josephson junctions and related device structures.

Josephson junctions are constructed of two superconducting films separated by an extremely thin layer of insulating oxide. This sandwiched structure with the insulator

embedded between two superconductors can act as the fastest switching element in a suitable submicroscopic circuit.

Superconducting Quantum Interference Devices (SQUIDs) are also based on the same quantum phenomenon. SQUIDs are finely processed superconducting loops through which the change in magnetic flux can be detected in quantized units Φ_0 of 2×10^{-15} Weber. These devices are highly sensitive to magnetic flux and are used in delicate precision instruments for metrology.

1.4.2 Application in supercomputers

Today's fastest supercomputers are capable of running at teraflop speeds, which is trillions of operations per second. It has been speculated that nanometer sized devices with unusual switching mechanisms, such as Josephson junctions joined with superconductors, will be necessary to achieve such blistering speeds. However, scientists are currently researching the even faster petaflop supercomputers. Researchers in Northrop Grumman Corporation have predicted that 100 billion Josephson junctions on 4000 microprocessors are imperative for operations at 32 petabits per second [10].

Researchers at the Israeli Weizmann Institute have also predicted that digital information can be stored and processed by the tiny magnetic fields that penetrate type II superconductors [10]. However, despite the fact that superconductors have been proved to have the greatest potential to construct fast operating supercomputers,

other technologies, such as quantum transistors, high density molecule-scale processors, and DNA based processing, also display the potential to achieve petaflop operations, and it is not yet a foregone conclusion that superconductor technology will be employed for the construction of future computers.

Reference

[1] Tipler and P. Allen, "Modern physics," 2003.

[2] "An introduction to the phenomenon of superconductivity," *http://www.chemsoc.org/exemplarchem/entries/igrant/main_noflash.html*.

[3] J. Charles P. Poole, "Handbook of Superconductivity," 2000.

[4] Michel Cyrot and D. Pavuna, "Introduction to Superconductivity and High-T_c Materials," 1992.

[5] "Colorado Superconductor, Inc.," *http://www.users.qwest.net/~csconductor/Experiment_Guide/Meissner%20Effect.htm*, 2001.

[6] R. Nave, "HyperPhysics***** Condensed Matter " *http://hyperphysics.phy-astr.gsu.edu/hbase/solids/scdis.html#c1*.

[7] A.M. Campbell and J. E. Evetts, "Critical currents in superconductors," 1972.

[8] F. Sonneman, "Type I and Type II Superconductors," *http://quench-analysis.web.cern.ch/quench-analysis/phd-fs-html/node26.html*, 2001.

[9] J. E. C. Williams, "Superconductivity and its applications ", 1970.

[10] Q. W. Yao, "Study of synthesis, structures and superconducting properties of magnesium diboride MgB_2 material," *MPhil Thesis*, 2004.

Chapter 2

Literature review of magnesium diboride

2.1 Discovery of MgB_2 superconductor

Magnesium diboride was commonly known to scientists in the late 1950s, but its superconducting properties had been overlooked until January 2001 [1], when researchers in Japan had announced their discovery that MgB_2 had a superconducting critical temperature, T_c, of 39K. This is much lower than the T_c values observed in most cuprates, but its superconducting properties have attracted ongoing research efforts worldwide [2-5], due to the fact that it is a non-oxide superconductor and superior in performance to other materials with the same crystal structure, which are generally poor in superconducting applications requiring performance in magnetic fields.

2.2 Structure and physical properties of MgB_2

Magnesium and boron are relatively abundant elements and easy to obtain commercially, so its remarkable performance as a superconductor operating near liquid hydrogen temperature (~20K) opens up a large area for industrial applications. The above-mentioned high T_c is probably due to the high vibration energy in the boron planes, where the strong Cooper pairs (coupled electron pairs) are carried

through the material. By a strong electron-phonon interaction the electrons overcome their natural repulsion and are brought together by crystal lattice vibrations. Extensive reviews on its superconductivity based on Bardeen, Cooper, Schrieffer (BCS) theory provide a background on this superconductor [6, 7].

2.2.1 Crystal structure of MgB_2

MgB_2 is a simple binary compound and has a hexagonal AlB_2 type structure similar to those of other kinds of boride. Its unit structure consists of alternating hexagonal layers of magnesium atoms and graphite-like honeycomb layers of boron atoms. The boron planes are separated by layers of magnesium, and the magnesium atoms are closely packed with each magnesium atom situated in between the centers of the hexagons forming each of the boron lattice planes. In each boron layer, each of the hexagons consists of six boron atoms, giving an overall 1:2 Mg-B ratio in the unit cell (Fig. 2-1). The unit cell lattice parameters for MgB_2 are a = 3.086 Å and c = 3.521 Å. The entire material structure of MgB_2 is anisotropic [8, 9]: the in-plane B-B distance is significantly shorter than the distance between layers.

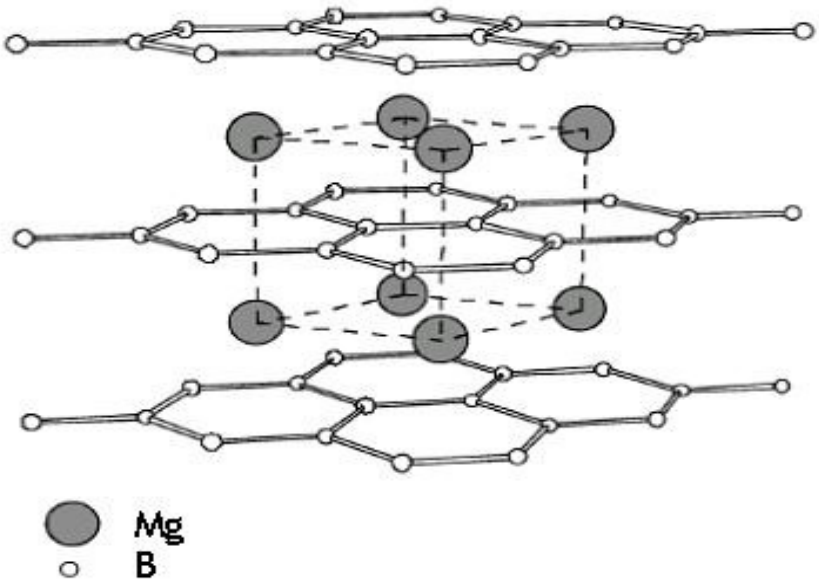

Fig.2-1 MgB_2 crystal structure.

2.2.2 Transport properties in polycrystalline MgB_2

MgB_2 has a comparatively large coherence length of 50Å compared to other high temperature superconductors (HTSs) [10]. This is also much larger than its grain boundary width, and therefore the current flow in polycrystalline MgB_2 will be affected only by its pinning properties, not by the degree of grain alignment. This makes MgB_2 useful in forming round wires by the powder-in-tube method for high critical current density, J_c, carrying applications [3].

However, critical current density can be reduced by orders of magnitude if the grain boundaries of polycrystalline MgB_2 are altered to exhibit induced weak link behaviour [11]. These effects are usually caused by impurity phases such as magnesium oxide

(MgO) which is omnipresent in many forms of MgB_2 superconductors. To avoid these unwanted phases has now become a central issue in commercial MgB_2 development.

2.2.3 Anisotropy of MgB_2

The MgB_2 layered structure has anisotropic properties with respect to magnetic fields and currents in various directions [9, 12]. MgB_2 thin films are textured, as the grains line up against the flat substrates, so anisotropy is particularly revealed in these samples [13, 14]. MgB_2 has been established as a two-gap superconductor with σ and π bands [6, 15]. The latter band can be suppressed in low magnetic field, and change in H_{c2} occurs in high fields subjected to change in the σ-bands.

$$H_{c2} = \frac{B_{c2}}{\mu_0}$$

Previous investigations by applying magnetic fields in the *ab*-plane and *c*-axis directions in two MgB_2 single crystals, one of which had a contracted *a*-axis, suggested that the electron phonon-coupling constant plays an important role in the T_c suppression [8], but increase of H_{c2} anisotropy and lattice distortion always result from impurity substitution, which introduces modification of the Fermi velocity and the density of energy states. However, textured and epitaxial MgB_2 thin films have recently been used to produce special anisotropic control devices.

2.3 MgB_2 Preparation

Different ways have been used to prepare MgB_2 samples since its discovery. Several of the main development streams include: magnesium diffusion into boron, the powder-in-tube method, and the laser deposition method. Elemental doping has also been adopted and studied to enhance the performance.

In terms of its physical shapes, different forms of MgB_2: bulks, tapes, wires, and thick and thin films, have been fabricated for different research and industrial purposes. The crystallization of MgB_2 is generally divided into two processes of thermal treatment called the "in situ" and "ex situ" methods, which will be briefly introduced in the next chapter [16].

2.4 Current Research on MgB_2

2.4.1 Chemical substitution of MgB_2

The method of chemical substitution has been proven to be useful in elaborating physical properties in many superconductors. However, MgB_2 was found to be compatible with many materials at high temperature, which makes its application an advantage, as MgB_2 would be less reactive with the materials that it would come in contact with in electronic devices. Results from previous experiments to determine the chemical compatibility of MgB_2 with other materials at sintering temperatures of 600˚C and 800˚C have been summarized in Table 2-1 [17]. These results show that MgB_2 is chemically compatible with most other likely materials in that temperature range.

Please see print copy for Table 2-1

Table 2-1 Reactivity of MgB_2 with various electronic materials [17].

2.4.2 MgB_2 Residual Resisitivity Ratio

The Residual Resisitivity Ratio (RRR) has been found to be from 4 to 20 depending on the purity level of the boron [18]. This result covers almost all the RRR values found in the literature. This shows that high purity boron is necessary to obtain high values of RRR. The highest RRR of 20 was obtained for a stoichiometric compound of isotopically pure boron.

2.4.3 Dependence of J_c in MgB_2 on annealing temperature (T_{ann}) and time (t_{ann})

The effects of annealing on the superconductivity of MgB_2 thin films as a function of T_{ann} and t_{ann} have been reported by W.N. Kang et al. [19]. In their experiment, different ex situ post-annealing conditions were employed, and they found that the best superconductivity was obtained for the films annealed at 900˚C for 30mins. J_c values of the various samples were estimated by measuring the magnetic field dependence of the magnetization loop. The highest J_c observed under these annealing conditions was 2.5×10^7 Acm^{-2} at 5K and zero applied field. Based on their observations, they claimed that the film (900˚C, 30mins) had very strongly connected grains with a high density of pinning sites.

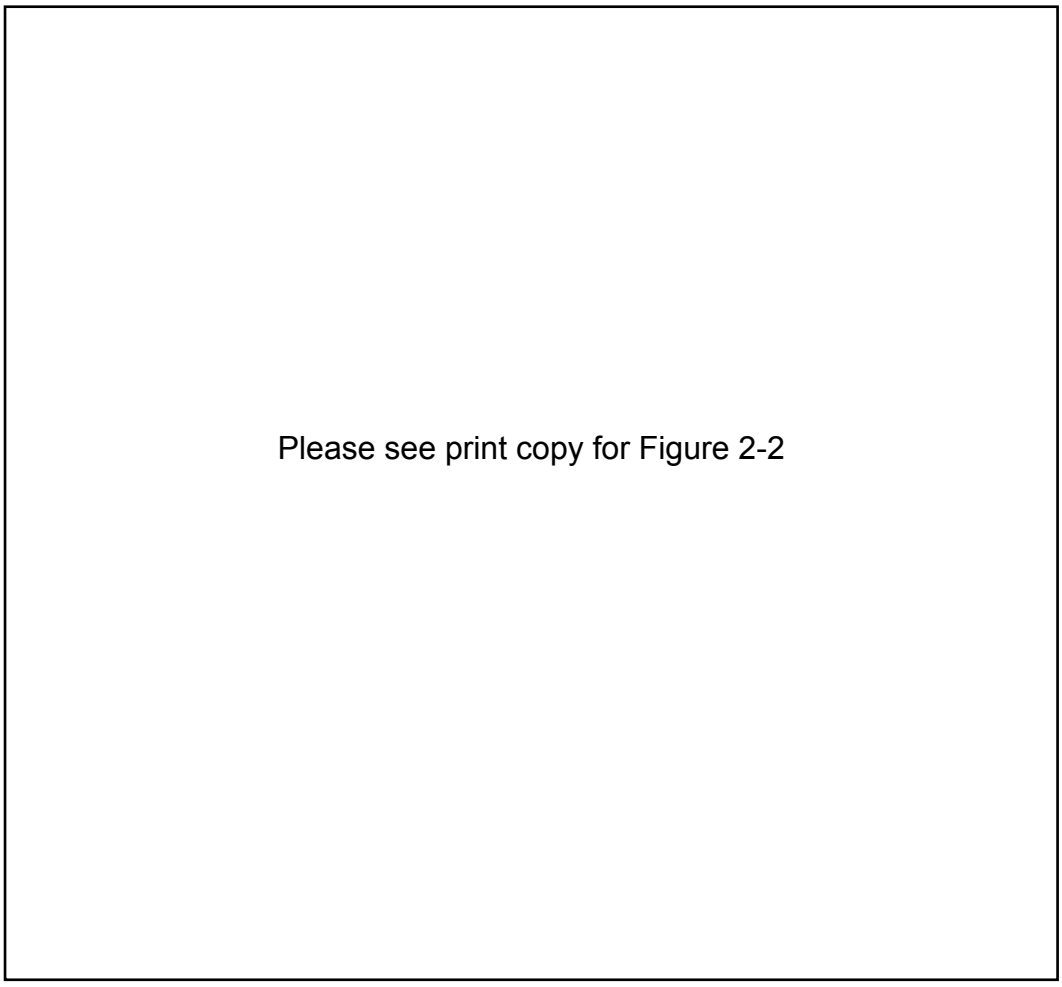

Fig. 2-2 Magnetic field dependence of J_c at 5K for various films grown at 700-950˚C for 30min and at 900˚C for 30-120min. Figure cited from [19].

2.4.4 Enhanced J_c properties of MgB_2 films due to elemental doping

Elemental doping is found to be an effective way to improve the properties of superconducting materials. In 2002, Dou et al. [4] discovered that SiC-doped MgB_2 samples had significantly enhanced flux pinning and irreversibility fields. They found that the enhancement due to SiC doping was consistent in both magnetic and transport J_c. The J_c values measured for 10 wt% SiC-doped MgB_2 wires were over 1.3×10^5 and 1×10^5 A/cm$^{2\,at}$ 5K and 4.5T and 20K and 2T, respectively. The T_c was also found to drop by only 1.5K for the 10 wt% SiC-doped samples, which is much less than with carbon substitution for boron in MgB_2.

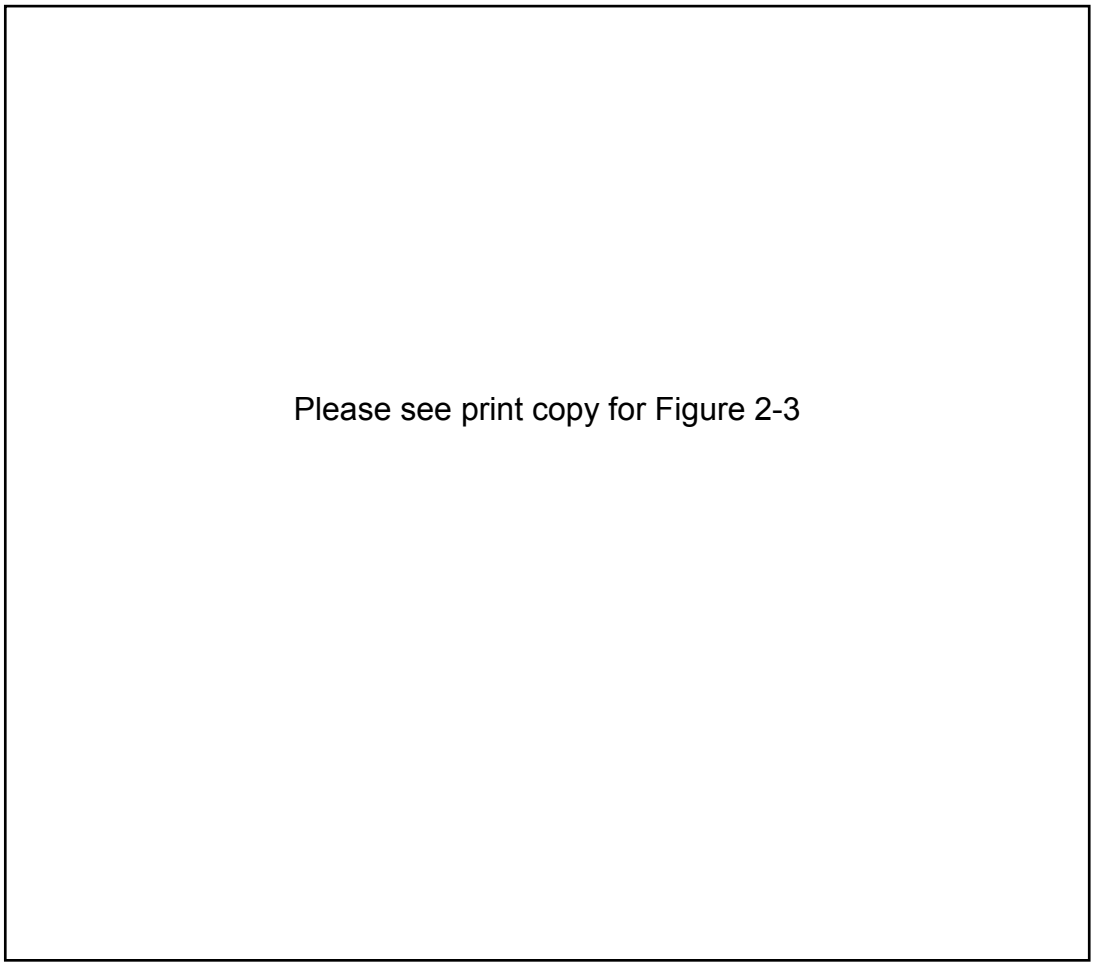

Fig. 2-3 Transport J_c for SiC doped and pure MgB_2 wires. Inset shows T_c for these samples. Figure cited from [4].

2.5 Some expectation of MgB_2 applications

Similar to other high-temperature superconductors (HTS), MgB_2 superconductor needs many major modifications of its superconductivity parameters so as to improve sample quality before it can be used in electronic devices. The detailed descriptions of the potential applications of MgB_2 are published elsewhere [20, 21], and I only mention the topic here as a brief introduction.

2.5.1 Microwave loss by surface resistance

Applications of MgB_2 in passive high frequency-devices have emerged from recent studies. These devices, such as microwave and terahertz resonators, antennas, filters and RF cavities, demand a low microwave surface resistance, R_s, which is regarded as the sum of a BCS surface resistance R_{BCS} [22] and a residual resistance R_{res}. The residual component R_{res} can be lowered by reducing the surface imperfections R_{imp} and decreasing trapped magnetic flux, which varies as $R_{flux} \propto H/H_{c2}$, where H is the magnetic field that induces trapped fluxoids. Hence, good H_{c2} behaviour in MgB_2 films could effectively reduce the microwave surface resistance.

2.5.2 Non-linear response of superconducting films to high- frequency devices

Another major factor which is required for our films for applications in high-frequency devices is a nonlinear response. This is important since a large nonlinear

response means that a high level of undesirable intermodulation products will be produced. Calculations have shown that MgB_2 and Yttrium Barium Copper Oxide superconductor (YBCO) have the same intrinsic nonlinear response to microwaves, but the intrinsically low nonlinear response of MgB_2 is much easier to achieve than with HTS cuprates. The nonlinear response is closely associated with the weak-links across grain boundaries, which is a particular problem in HTS high-frequency devices, whereas MgB_2 will benefit from its non-weak-link material structure. However, the nonlinear response properties of MgB_2 films we studied so far are not much better compared to HTS. We think this may be attributable to extrinsic sources of nonlinear responses such as impurities developed near the film surface during the film preparation process, so further optimization is therefore required to eliminate these defects.

2.5.3 Superconducting Fault Current Limiter (FCL)

In 2006 several MgB_2 FCL prototypes were built under the LIMSAT Italian project [21]. These non-inductive windings were tested with AC transport currents in liquid He and Ne for a range of frequencies from 2 to 500Hz and reached a critical current on the order of 600A, which was in accord with what was expected from the transport properties of the conductor.

2.5.4 Magnetic Resonance Imaging (MRI)

MgB_2 conductors have been contemplated in an MRI magnet design by ASG superconductors. They planned to put the MgB_2 magnet on the MRI market after the magnet was finally assembled and showed positive results [21]. They confirmed that the magnet could reach its nominal current of 90A and a central field of 0.5T. This is very possibly the first large scale commercial application of MgB_2 superconductor on the market.

Reference

[1] Nagamatsu J, Nakagawa N, Muranaka T, Zenitani Y, and A. J, *Nature,* vol. 410, p. 63, 2001.

[2] D.C. Larbalestier, M. O. Rikel, L.D. Cooley, A.A. Polyanskii, J.Y. Jiang, S. Patnaik, X.Y. Cai, D.M. Feldmann, A. Gurevich, A.A. Squitieri, M.T. Naus, C. B. Eom, and E. E. Hellstrom, "Strongly linked current flow in polycrystalline forms of the new superconductor MgB_2," 2001.

[3] P. C. Canfield, D. K. Finnemore, S. L. Bud'ko, J. E. Ostenson, G. Lapertot, C. E. Cunningham, and C. Petrovic, "Superconductivity in Dense MgB_2 Wires," *PHYSICAL REVIEW LETTERS,* vol. 86, 2001.

[4] S. X. Dou, S. Soltanian, J. Horvat, X. L. Wang, S. H. Zhou, M. Ionescu, and H. K. Liu, "Enhancement of the critical current density and flux pinning of MgB_2 superconductor by nanoparticle SiC doping," *APPLIED PHYSICS LETTERS,* vol. 81, pp. 3419-3421, 2002.

[5] T. Masui, S. Lee, and S. Tajima, "Origin of superconductivity transition broadening in MgB_2," *Physica C,* vol. 383 pp. 299–305, 2003.

[6] F. Bouquet, R. A. Fisher, N. E. Phillips, D. G. Hinks, and J. D. Jorgensen, "Specific Heat of $Mg_{11}B_2$: Evidence for a Second Energy Gap," *PHYSICAL REVIEW LETTERS,* vol. 87, 2001.

[7] W. N. Kang, C. U. Jung, Kijoon H. P. Kim, Min-Seok Park, S. Y. Lee, Hyeong-Jin Kim, Eun-Mi Choi, Kyung Hee Kim, Mun-Seog Kim, and S.-I. Lee, "Hole carrier in MgB_2 characterized by Hall Measurements," *arXiv:cond-mat/0102313 v3,* 21 Feb 2001.

[8] T. Masui*, S. Lee, and S. Tajima, "Effect of the growing process on the electronic properties of MgB_2 single crystals," *Physica C,* vol. 392–396 pp. 281–285, 2003.

[9] Yu. Eltsev *, S. Lee, K. Nakao, N. Chikumoto, S. Tajima, N. Koshizuka, and M. Murakami, "Anisotropic superconducting properties of MgB_2 single crystals," *Physica C,* vol. 378–381, pp. 61–64, 2002.

[10] Kijoon H. P. Kim, W. N. Kang, Mun-Seog Kim, C. U. Jung, Hyeong-Jin Kim, Eun-Mi Choi, Min-Seok Park, and S.-I. Lee, "Origin of the high DC transport critical current density for the MgB_2 superconductor," *cond-mat/0103176,* 2001.

[11] Shi X. Dou, Joseph Horvat, Saeid Soltanian, Xiao L. Wang, Meng J. Qin, Shi H. Zhou, Hua K. Liu, and P. G. Munroe, "Transport Critical Current Density in Fe-Sheathed Nano-SiC Doped MgB_2 Wires," *IEEE TRANSACTIONS ON APPLIED SUPERCONDUCTIVITY,* vol. 13, pp. 3199-3202, 2003.

[12] S. Serventi, G. Allodi, R. De Renzi, L. Romano`, P. Manfrinetti, A. Palenzona, A. Amato, and C. Baines, "Anisotropy and two-gap contributions to flux lattice in MgB_2 superconductor and $Mg_{1-x}Al_xB_2$ alloys," *Physica B,* vol. 374–375, pp. 235–238, 2006.

[13] C. Ferdeghini *, V. Ferrando, G. Grassano, W. Ramadan, V. Braccini, M. Putti, P. Manfrinetti, and A. P. b, "Transport properties of c-oriented MgB_2

thin films grown by pulsed laser deposition," *Physica C* vol. 372–376, pp. 1270–1273, 2002.

[14] Won Nam Kang, Hyeong-Jin Kim, Eun-Mi Choi, Kijoon H.P. Kim, and S.-I. Lee, "Growth and transport properties of *c*-axis-oriented MgB_2 thin films," *Physica C* vol. 378–381, pp. 1246–1251, 2002.

[15] S. Tajima, T. Masui, H. Uchiyama, J.W. Quilty, Yu. Eltsev, S. Lee, A. Yamamoto, and H. Mori, "Electronic state of MgB_2 superconductor," *Current Applied Physics* vol. 2, pp. 315–319, 2002.

[16] Yue Zhao, Mihail Ionescu, Josip Horvat, and S. X. Dou, "Comparative study of in situ and ex situ MgB_2 films prepared by pulsed laser deposition," *Supercond. Sci. Technol. ,* vol. 17, pp. S482–S485, 2004.

[17] R.J. Cava*, H.W. Zandbergen, and K. Inumaru, "The substitutional chemistry of MgB_2," *Physica C* vol. 385, pp. 8–15, 2003.

[18] R.A. Ribeiro *, S.L. Bud'ko, C. Petrovic, and P. C. Canfield, "Effects of boron purity, Mg stoichiometry and carbon substitution on properties of polycrystalline MgB_2," *Physica C* vol. 385 pp. 16–23, 2003.

[19] W.N. Kang *, Eun-Mi Choi, Hyeong-Jin Kim, Hyun-Jung Kim, and S.-I. Lee, "Growth of superconducting MgB_2 thin films via postannealing techniques," *Physica C* vol. 385, pp. 24–30, 2003.

[20] H. Yamamoto, A. Tsukamoto, H. Hasegawa, K. Saitoh, Y. Fukuda, and M. Okada, "Fabrication and characterization of resonant devices using superconducting MgB_2 thin films," *Physica C,* 2007.

[21] Valeria Braccini, Davide Nardelli, Roberto Penco, and G. Grasso, "Development of ex situ processed MgB_2 wires and their applications to magnets," *Physica C* vol. 456 pp. 209–217, 2007.

[22] E. W. Collings, M. D. Sumption, and T. Tajima, "Magnesium diboride superconducting RF resonant cavities for high energy particle acceleration," *Supercond. Sci. Technol.,* vol. 17, pp. 595-601, 2004.

Chapter 3

Thin Film Formation Process and Experimental Systems

3.1 Methods of MgB_2 thin film preparation with a pulsed laser deposition (PLD) system

3.1.1 Introduction to the PLD system used for thin film preparation

Pulsed laser deposition is a versatile technique for creating thin films and multilayer structures [1-3]. The PLD method of thin film growth involves evaporation of a solid target in an ultra-high vacuum chamber by means of short and high-energy laser pulses. In a typical PLD process, a target component consisting of the sample source is placed inside a vacuum chamber. The high frequency pulsed radiation from the laser beam vaporizes the surface of the target, and the vapour condenses on a substrate. The targets are not deformed by heat energy apart from the species being evaporated from the surface. The main components used in this part of the experimental system are a laser generator capable of producing high frequency pulses, laser optics and a deposition chamber evacuated to an ultra-high vacuum.

The system set-up is quite simple, but the principle behind the pulsed laser deposition process involves very complex physical phenomena. Several stages are involved

through the entire process of thin film formation, from the laser-material interaction to the transfer of the ablated material through the plasma plume onto the heated substrate. The fundamental process is that energy is transferred to the atoms through the impact of the radiation on the solid target surface and forms a high-pressure gas from the target material. The ablated highly energetic species interacts with the background gas to form a plasma plume, and the ablated material is transferred through the plasma plume onto the substrate surface. These stages are critical for the formation of quality epitaxial crystalline, stoichiometric, uniform, and small surface roughness thin films and some are still being debated.

3.1.2 Advantages of the PLD technique

The PLD method has a number of unique features which make it more advantageous than other current deposition techniques, such as sputtering, molecular beam epitaxy (MBE), and chemical vapor deposition (CVD). Commercially, its experimental set-up is relatively cheap, and a PLD system can produce films with comparable quality to those produced in an MBE system, which has a far more expensive technical set-up.

Other advantages of PLD in terms of efficiency and cost reside in the fact that the laser is the source that creates the plume species and works independently from the deposition system [4]. Hence, it is possible to produce complex multilayer films by switching various targets into and out of the focal point of the laser beam. Also, the beam can be diverted into different paths using good optical apparatus with low energy retardation on reflection and transmission, resulting in a clustered system,

which is capable of several separate depositions, making up an efficient deposition laboratory.

The mass and pressure of the ambient gas affect the energy of the ablated particles and will have a direct influence on the energy of the particles arriving at the substrate. Different species can be removed from stoichiometric targets, whereas other deposition methods require co-deposition of separate Mg and B sources due to their different vapor pressures. For the transfer of a target material which contains a highly volatile element, an additional target of the element can be used to compensate for the excessive loss during deposition. In our case, the high Mg vapor pressure requires an additional Mg cap to be deposited on the film surface from an Mg-rich target to compensate for the high loss of magnesium through this volatility.

Besides what has been described above, the main advantage of PLD derives from the laser material removal mechanism: materials are removed from the target based on a photon interaction to create a vapor or plume of material by rapid explosion of the target surface. A substrate is placed a short distance from the target to collect the ejected plume produced by this laser-induced expulsion. In comparison, the vapor produced using other evaporation methods is composed of different elements, but depends on the vapor pressures of the elements in the target. Thus, the desired stoichiometry for films of multi-element materials is generally easier to obtain using PLD than with other deposition technologies.

3.2 Formation and growth of thin film

3.2.1 Energy transfer through interaction

It is thought that the complex ablation mechanisms of materials involve collisions, thermal excitations, exfoliation, and hydrodynamics. Despite the descriptions of these phenomena, however, the energy transfer stage can generally be explained by the fact that the flux densities of the focused laser beam are sufficiently high to activate the surface atoms into gas of atoms and ions [5]. The ablation rate depends on the influence of the laser shining on the target surface, and the ablated plume of the dissociated materials from the target has the same stoichiometry as in the target.

3.2.2 Dynamics of the ablation materials

The spot size of the laser on the target surface and the temperature of the plasma gas formed have significant effects on the uniformity of film growth. The emitted materials (atoms, ions, clusters, etc.) tend to peak forward and swiftly move towards the substrate during ablation. A plasma plume is formed due to the interaction between the exploding species and the background gas. It has been found that the angular spreading of ablation can be reduced by placing a mask directly in front of the substrate. The angular spread of the ablation materials can also be controlled by the target to substrate distance.

3.2.3 Deposition on the substrate surface

This is the most important stage to determine the quality of the thin film. At this stage, the substrate experiences various types of modification by impingement of the emitted particles onto the substrate surface, and these high energy particles arriving from the plasma may cause sputtering of some of the surface atoms of the substrate, so that a collision region is formed between the incident flow and the sputtered atoms. During this stage, the two processes compete and a thermally stabilized condition is established within this region. Film growth depends on the condensation rate of the ablation particles.

When condensation is higher than the rate at which particles are sputtered, a thermal equilibrium condition can be reached quickly. The condensation rate is thought to be highly dependent on the ablation rate, and for this reason we used a 248nm wavelength laser to give short pulses (20 ns) of radiation at a repetition rate of 10Hz to make an effective ablation of the target material. Once thermal equilibrium is obtained, film growth on the substrate surface will be at the expense of the direct flow of the ablation particles.

3.2.4 Nucleation and growth of crystalline film

There are many factors originating from both the condensing material (density, kinetic energy of the vapour, sticking coefficient, etc.) and the substrate that affect the nucleation process and the growth of crystalline films, but the two main factors contributing to the growth mechanism are the growth temperature on the substrate and the critical size of the nucleus. The correct critical nucleus size refers to the smallest

separate islands of the film that can grow on the substrate surface. The important initial stages of island formation remain an open question, but it has been explained [6] that the critical size of the nucleus is related to the temperature at which growth occurs.

The nucleation process can be explained in classical nucleation theory [7], which indicates that a relatively large critical nucleus size and small supersaturation results in three-dimensional growth. In the high supersaturation regime at low growth temperatures where the critical nuclei are very small, two-dimensional growth dominates. At the beginning of the growth process, some gaseous atoms or ions which start to condense onto the surface of the substrate form small and movable islands which can grow by accepting new adhering particles: this is the nucleation phase.

An important question has been raised on the shape of these growing small islands. It has been demonstrated that a significant nucleation rate will occur above a critical supersaturation and that 3D island formation will take place if the wetting layer is thick enough to reduce interaction with the substrate, so that liquid drops of the condensed particles tend to merge together themselves, rather than involving atoms of the substrate. However, if diffusivity between drops of the species and the substrate is high, the condensed particles tend to combine with the substrate atoms, so the growth of a wetting layer will be in the form of two dimensional islands or platelets. Obviously, if in the ongoing growth process the new particles still tend to combine with the surface of the wetting layer, then layer-by-layer nucleation will occur for the incompletely wetted substrate.

As already described previously, the way in which a film is formed has a direct influence on its properties. Here it is the nucleation and growth stages that control the final properties of the film.

Growth of a crystalline film depends on the mobility of the newly added vapour atoms. The adatoms will normally diffuse through a few atomic distances into the newly formed film before becoming stable at a fixed position within the film. The surface diffusion capability of these adatoms is determined by the substrate temperature. The crystal growth is more rapid at higher substrate temperatures, and the defect level is lower, whereas a more disordered structure arises at lower temperature due to impingement by energetic particles that overwhelm the crystal growth process. This often results in less alignment or even amorphous characteristics in the grain structure.

Smooth and uniform thin films with nano-scale structures can be obtained by a layer-by-layer nucleation process. This can be achieved by having a very low deposition rate, which is induced by short laser pulse duration, and hence the temporal spread of the ablated materials is small. Highly energetic ablated species can also help to raise the substrate surface temperature, and this means that the pulsed laser deposition is applicable for crystalline films deposition.

3.3 The PLD set-up in ISEM

3.3.1 Schematic layout of the PLD system in ISEM

The PLD deposition system used in this work was built by ISEM staff. A schematic layout of both the PLD system and the pumping system used in this work is shown in Figure 3. The targets are installed on a 6-pole carousel, and the substrate is mounted on a disk substrate holder on top of a resistive heating wire, in a 52L spherical high vacuum chamber. A K-type thermocouple is placed in the middle of the substrate holder and closely attached to the hot plate. Another thermocouple is attached to the substrate holder surface with silver paste for calibration of the surface temperature at the sample.

Two shields are placed between the target and the substrate. One is a fixed shield with a 30 mm diameter opening. This opening area is designed such as to allow the exposure of the active target to the laser spot, as well as protecting the other targets on the carousel from cross-contamination during the ablation of the active target. The other shield is movable and can be switched to cover the entire front surface of the substrate. This shield works as a shutter to protect the substrate or the sample by blocking the plume when cleaning or target changing is in process.

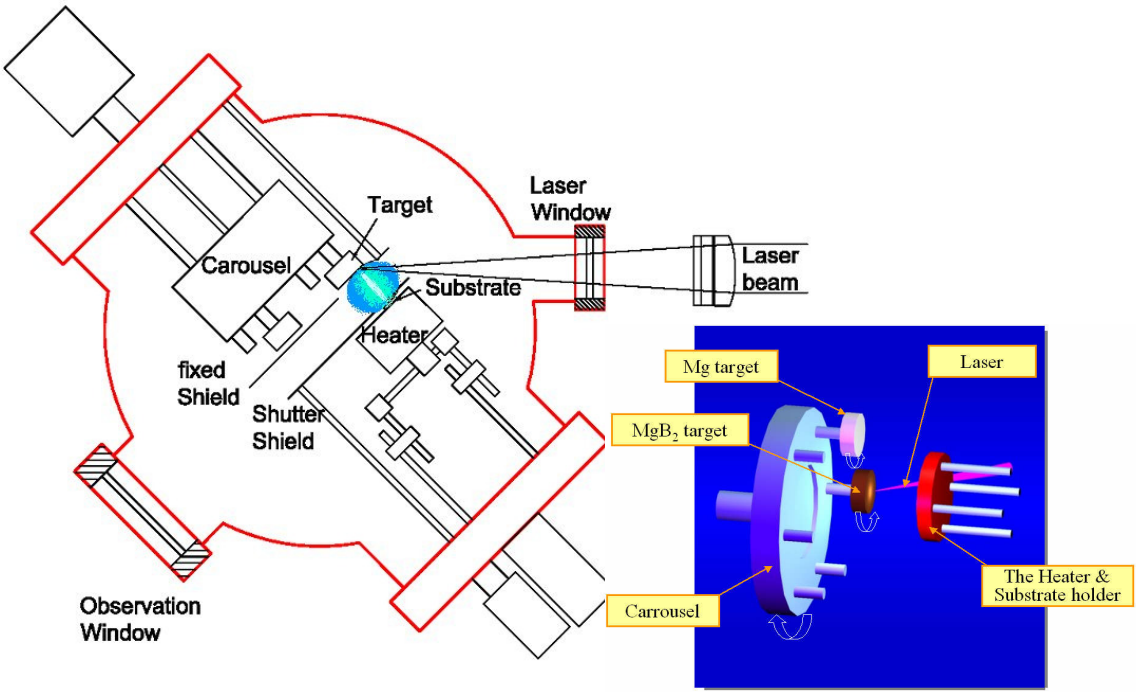

Fig. 3-1 A schematic diagram of the PLD se-tup used for the common on-axis deposition geometry for MgB_2 in-situ annealed film. The inset figure is a 3-D illustration of the interior of the chamber system. The target-substrate distance is adjustable by changing the height of the heater supporting frame before mounting the part in the chamber.

3.3.2 The vacuum system

Before carrying out the deposition, the chamber is usually evacuated to a vacuum level of at least $9x10^{-8}$ Torr or better after more than 16 hr baking at 200˚C under vacuum. Argon (purity 99.995%) was used as the background gas. Potent up and down stream control of the background gas pressure (~120mTorr) during the deposition is achieved by adjusting a pin valve on the argon delivery system and by throttling the gate valve on the pumping port.

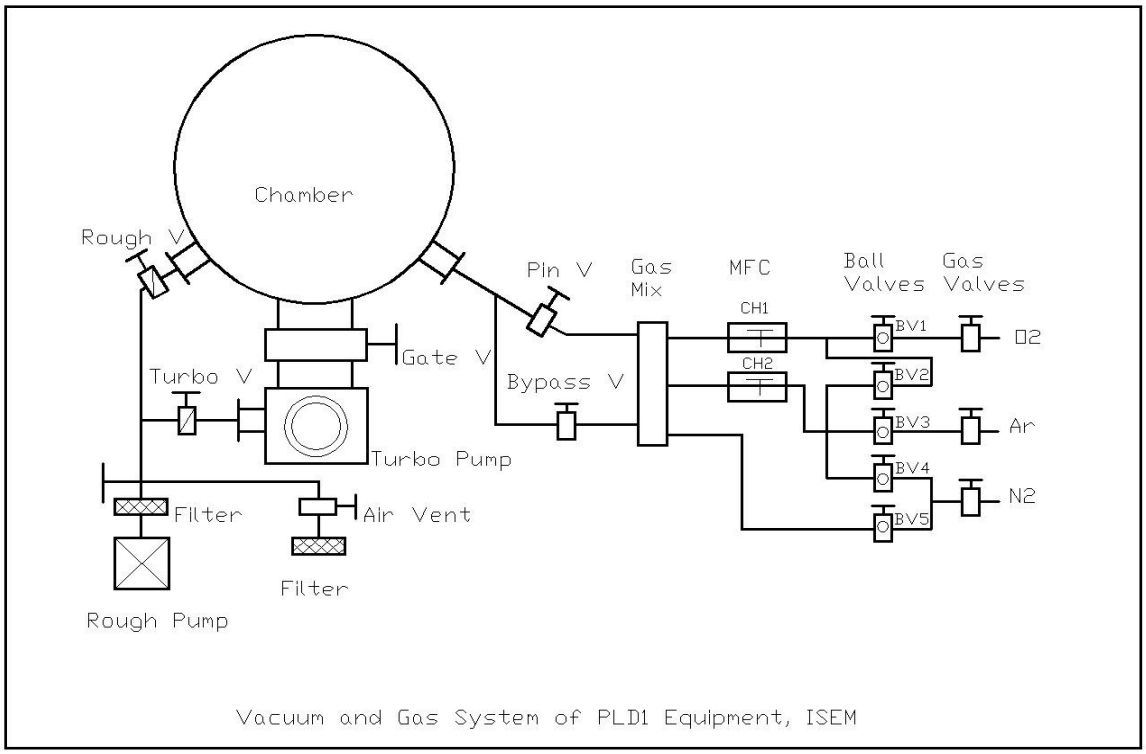

Fig. 3-2 A brief schematic layout of the PLD vacuum system showing all the pumping mechanisms, ISEM, UOW.

3.3.3 Preparation for deposition

The light source used for these deposition experiments was generated by a KrF excimer laser manufactured by Lambda Physik Complex 301 (λ = 248nm), with a pulse duration of about 20 ns (FWHM). The laser has a maximum pulse repetition rate of up to 10 Hz, and a maximum energy of 1,100mJ/pulse can be delivered on each pulse. Both the repetition rate and the high voltage can be adjusted from the laser control panel during deposition. The laser beam was trimmed by a diaframe to remove the blurred beam edges. The energy flow after the diaframe is about 46% of the initial

one. A spherical convex lens with a focal length of 700 mm was used to focus the trimmed laser beam. The convex lens was positioned outside the chamber, so that the focused beam hit at exactly 45°from the target surface normal. The plume was then generally perpendicular to the target surface. The energy attenuation through the lens and the window is less than 10%.

The substrates used in this work were mainly Al_2O_3. They were *c*-oriented with one side polished to an average roughness R_a of less than 1 nm. The selection of Al_2O_3 for our sample substrates was because of the low reactivity with MgB_2 at temperatures below 950℃. The substrates were cut from 2 inch Al_2O_3 wafers into 7 x 5 mm^2 rectangles with a diamond cutter.

Commercial targets of both stoichiometric MgB_2 and high purity Mg were employed for the *in situ* film and Mg cap layer deposition. The MgB_2 target used had 84% density and was provided by SCI Engineered Materials, while the Mg target was of 99.9% purity and supplied by Goodfellow Inc. The XRD pattern of the polycrystalline MgB_2 target indicates unoriented MgB_2 grains and trace amounts of impurity (Fig. 3-7). A single crystal Si target with purity better than 99.9% was also used for the Si added film deposition.

3.4 The function of the argon background gas

The background gas we used for deposition was high purity argon (99.99%). The high energy Mg+B species ablated from the target encounters a series of collisions with the background gas and generate a plume (MI: M+ green, MII: M2+ blue) which was in accordance with the background gas used in previously reported MgB_2 thin film preparation [8-10]. In order to optimize the pressure conditions for deposition, the chamber was filled to several different argon pressures. These studies on the influence of the argon background gas show that the emission spectrum detected from the MgB_2 plume has higher intensity of the Mg I green line (517nm) than that of the Mg II blue line (448.1nm) at a low buffer pressure of $\leq$ 10mTorr. The Mg II intensity increases with increasing argon pressure and becomes almost an order of magnitude larger when the argon pressure is increased up to 150mTorr. This is in agreement with observations of the change of plume color from blue to green when the argon pressure is insufficient inside the chamber. Hence the argon pressure plays a significant role, as a blue laser plume favors the formation of superconducting MgB_2 thin films [9, 10].

At high pressure, the expansion of the plume develops into a shock wave through interaction with the background gas [9]. In this regime, the plume causes the ambient gas to be compressed and heated, resulting in the slowing down of the plume, when the pressure of the gas surrounding the edge of the plume is comparable to the plume pressure itself. The shock wave also produces a redistribution of kinetic and thermal energies between the plume and the ambient gas. As the plume slows down, the kinetic energies of the species are converted to thermal energy of the plume, causing it to heat up. This results in the enhancement of excitation and ionization of the impinging atoms and the reduction of the kinetic energy of the ablated species.

Since highly energetic particles of materials such as Mg can cause re-sputtering on the surface, affecting the stoichiometry of the growing film, the slowing down effect helps to reduce the release of Mg during deposition, while the arrival of species that are excited or ionized to a higher degree is beneficial, because it enhances surface mobility and favors the growth of thin films at lower substrate temperatures through the release of thermal energy in the impact region. It is thus of great importance for the control of MgB_2 film growth.

A shock wave develops under a large number of collisions between the ejected species and the ambient gas atoms. By considering that the particles' mean-free-path is inversely proportional to the ambient gas pressure, an approximately inverse proportionality is expected for the distance-related pressure threshold for shock wave formation. This observation is in accordance with the successful deposition of as-grown MgB_2 superconducting films by increasing the argon gas pressure to a few tens of Pascals with a target-substrate distance of ~15mm [11].

A similar experiment on the influence of argon gas was also carried out by Y. Zhao [4]. His experiment shows that the outer edge of the plume turns a brighter blue color as the argon pressure was increased from 1×10^6 to 290mTorr. The plume grows up to a pressure of 200mTorr and then decreases with further increases in the argon pressure. An optimum deposition pressure of 120mTorr, with a laser energy of 350mJ/pulse and a target-substrate distance of 23mm, was obtained and then used to carry out the depositions.

3.5 Reviews on methods of high temperature annealing

3.5.1 The in situ annealing procedure

For the in situ annealing procedure, a precursor film was first deposited on the substrate from ablation of a stoichiometric MgB_2 target. When the first layer of MgB_2 precursor film was deposited, an additional Mg layer was then also deposited on top of the precursor film by ablating a pure magnesium target. After the deposition, the atmospheric pressure was increased to 760Torr argon gas. The substrate holder was heated up to 420-800°C, and the samples were maintained at that temperature for a range of annealing dwell times, from 1min to 60mins. It was found difficult to avoid temperature overshoot and to keep it constant within the first few minutes of annealing, but the oscillation within a small range ~5°C and the average temperature during this time was taken as the annealing temperature.

Different heating rates were attempted in previous experiments, from the rapid one where the sample was heated up at around 110°Cmin^{-1} (t_{ramp}= 4mins) to the slower ones at 25-63°Cmin^{-1} (t_{ramp}=7-17mins), and the influence of the heating rate on $T_{c\ \mathrm{onset}}$ was examined [12]. It was shown that the $T_{c\ onset}$ (17K) of a film with a slower heating rate (63°Cmin^{-1}) is rather lower than that (21K) of the rapidly heated one (110°Cmin^{-1}). The drop in $T_{c\ onset}$ was attributed to an increase in the temperature lag between the thermocouple used to calibrate the temperature and the sample at the high heating rate. However, a high $T_{c\ onset}$ and narrow transition width were obtained from a reasonably slow heating rate of 38°Cmin^{-1}. After the dwell, the power was automatically

switched off by the preset timer to allow the sample to cool down freely at a cooling rate of around 50°Cmin^{-1}.

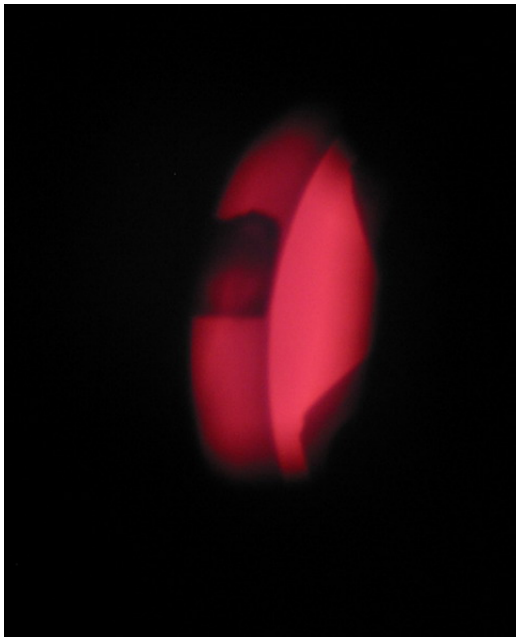

Fig. 3-3 A photo image of a film sample on the heater during the high temperature annealing.

3.5.2 The ex situ annealing procedure

Traditionally, both the in situ and ex situ methods are based on the powder in tube method, but while the ex situ method uses fully reacted MgB_2 powders, the in situ uses a mixture of non-reacted Mg and B. The ex situ annealing procedure he used is not included as part of the work in this report, and I only mention it as a comparison with reference to his paper [4].

In his work, a boron target of around 40% density was ablated to deposit a boron precursor film on a sapphire substrate at 250˚C inside a 10^{-7}-10^{-6}Torr evacuated chamber. The precursor film was then wrapped in Ta foil and sealed inside a stainless steel tube by hot impact-forging. The wrapped boron film was loaded into the tube together with Mg pellets. Then the tube was connected to the purging system, and purged with argon 3 times, then filled with argon to 1 atmosphere to ensure that there would be no oxidation inside the tube. The tube was then heated to white-hot color by a gas torch and sealed by hammering. After the sealed end was cut off, the tube was gradually inserted into a 900˚C tube furnace, which had a temperature control calibrated by a thermocouple with an accuracy of ± 1˚C, and kept for 30min, excluding the 5min insertion and extraction of the tube into and out of the furnace.

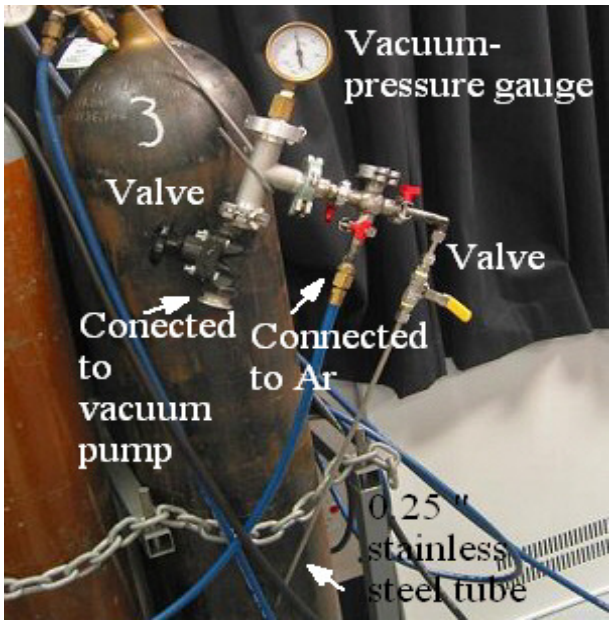

Fig. 3-4 The homemade sealed-in-argon apparatus for the ex situ annealing of MgB_2 film [4].

3.5.3 Experimental reviews between in situ & ex situ annealed films by PLD

Two types of MgB_2 film prepared by pulsed laser deposition with in situ and ex situ annealing processes were studied, and significant differences in their superconducting properties were found and reported in a previous studies [13]. Despite the suppressed T_c and surface quality of the in situ annealed film, which have already been mentioned, the in situ preparation method has other advantages over the ex situ for the application of MgB_2 films in superconducting electronics.

The surface features of the two types of film revealed that the in situ film has a much better, finer grained structure (with a smaller grain size ~3nm), which is more desirable for efficient pinning [13]. This improved structure probably resulted from the comparatively low annealing temperature and short annealing time, whereas the ex situ film had a random grain orientation and larger grains. In the resistivity transition measurements, the ex situ film has higher T_c and a narrower transition width in the *R-T* curve, but the diamagnetism transition in the *M-T* curve for the in situ film is actually sharper, indicating that the superconducting phase is more homogeneous in the in situ film. Comparative J_c measurements [13] also showed that the in situ film had much weaker field dependence than the ex situ film.

3.6 Microstructure characterization

3.6.1 Scanning Electron Microscopy (SEM) observations

There are many tools that can be used to view microscopic objects. Among them, the Scanning Electron Microscope (SEM) covers a wide range of magnifications, from about × 10 to × 1,000,000. The following sections briefly describe some of the important SEM features, such as imaging of the structure, etc.

3.6.1.1 Microstructure characterization

Inside a scanning electron microscope, an electron gun is used to generate the electron beam. There are roughly two types of electron guns: the thermionic emission gun and the field emission gun. The electron microscope used for microstructure analysis in this work was a JOEL JSM-6460A field emission SEM equipped with an energy dispersive spectroscopy (EDS) system. It has an electron emission gun which consists of three electrodes: a LaB_6 cathode filament (with tungsten type filaments occasionally employed), a Wehnelt cylinder, and an anode. The thermoelectrons are first emitted from the filament, and an accelerating voltage is applied between the filament and anode to energize the thermoelectrons which form an electron beam. During the formation of this electron beam, a bias voltage is also applied between the filament and Wehnelt to collect the thermoelectrons into a crossover point. The LaB_6 filament, which can produce a very small crossover point, is a very bright source.

3.6.1.2 Surface topography

The electrons from the electron beam interact with the atoms composing the specimen surface, producing various kinds of information [14]. The information emitted when

scanning the specimen is converted into an amplified electric signal, which is then fed into an observational cathode ray tube (CRT), which can adjust the scanning spot (usually several nanometers in diameter). This spot is shown spontaneously as the electron beam scans the specimen surface, thus the information emitted is displayed on the CRT as an image. In our SEM images, the specimen surface topography can be seen from the secondary electron image, with the magnification of the displayed image defined as the ratio of the size of image on the CRT to the size of the scanning spot of the electron beam.

The main problem in the observation of our MgB_2 films is that the films were deposited on insulator substrates, which induced an accumulation charge on the film surface, causing excessive brightness, image drifting, and blurring on the secondary electron image. To reduce the amount of accumulated charge, our films were electrically connected to the SEM aluminum specimen stage by using conductive tapes which flipped over on the surface of the films. Another effective way to reduce surface charge is to reduce the spot size during the SEM analysis. For our JOEL JSM-6460A SEM, we lowered the spot size parameter, in order to reduce the charging effects.

3.6.1.3 Energy Dispersive Spectroscopy (EDS)

There are mainly two types of information about the composition of samples that can be obtained [4]:

(1) Qualitative analysis: The elements contained in the samples are identified by detecting and analyzing the characteristic x-rays emitted.

(2) Quantitative analysis: The relative weight concentration of the elements.

To do EDS, the electron beam has to be very finely focused to perform an elemental analysis of a very small area on the sample surface. In our JOEL SEM, the sample surface was first observed with secondary electron imaging. The point to be analyzed was indicated by the crosshairs of the cursor lines displayed on the image. The electron beam was positioned at the designated point on the sample, a qualitative analysis was performed, and the distribution of any of the corresponding elements could also be observed by selecting a specified characteristic x-ray energy peak.

A problem that needs to be considered when using EDS is the depth of the interaction zone, which can be controlled by adjusting the acceleration voltage. The interaction zone should not exceed the actual film thickness, to avoid the possibility that a signal from the substrate is mixed into that from the MgB_2 film. However, in order to induce the characteristic X-ray, the acceleration voltage should be higher than the X-ray excitation energy for major peaks of the corresponding elements in the EDS spectrum.

3.6.2 X-ray diffraction analysis

In this project, in order to identify the different phases present in our samples, it is necessary to use the x-ray diffraction method for analysis of the chemical compounds which may directly influence the properties of our samples. X-ray diffraction has long been known as a simple and convenient method of crystalline analysis since most of

the solid materials have crystalline phases. Each pure crystalline substance has its own pattern via x-ray interaction. For a polycrystalline sample, each of the different existing phases therefore produces a pattern independent of the others, allowing a full identification of all the polycrystalline phases.

Standard diffraction patterns have been collected and stored from single and multi-component crystalline phases. These standard patterns allow searching and matching to be done on patterns experimentally obtained from different kinds of sample, which is particularly useful for diffraction on powder samples, because these usually contain a random distribution of all possible crystal orientations.

3.6.2.1 General X-ray diffraction theory

The general theoretical consideration behind x-ray diffraction is that all crystals are considered to have a regular pattern of atomic arrangement formed from repetition of the unit cell. This is important, as it governs the characteristics of a substance for x-ray diffraction. The x-ray wiggles the surrounding electrons as it hits the atom, the electrons oscillate at the same frequency as that of the incoming x-ray ($f = E/h$), and emissions are given off from the excited electrons as waves to release the energy. Most of these waves add up to give destructive interference in different directions and cancel out one another, since the atoms are in a regular pattern [15], they therefore will cause constructive interference in a few directions and reinforce one another. This composes the reflected beam to be detected.

3.6.2.2 Bragg's law

Since the atoms are set in planes, the reflected beam can be unambiguously regarded as arising from a series of parallel planes inside the crystal. The inter-planar spacing can be related to the energy/wavelength of the x-ray beam using Bragg's law:

$$2dsin\theta = n\lambda$$

where d is the inter-planar spacing, θ the angle of incidence for constructive interference, n an integer giving the order of diffraction, and λ the wavelength of the light.

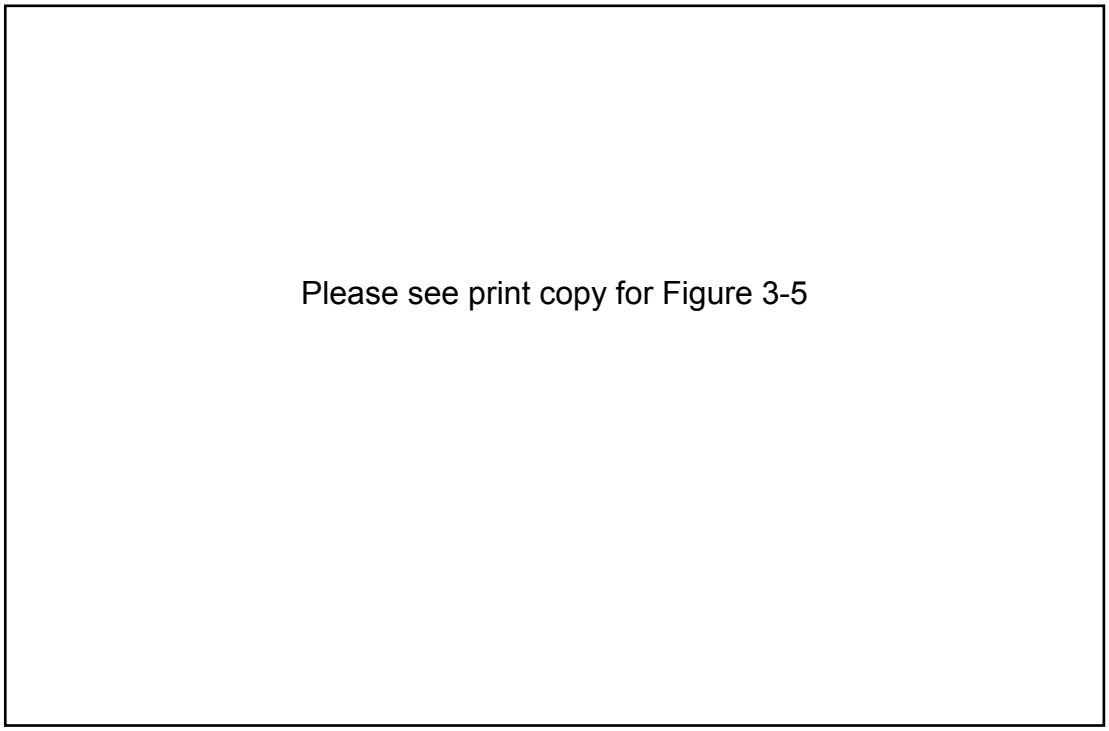

Fig. 3-5 Graphical description of Bragg's theory. Figure cited from [16].

The possible *d*-spacing between crystal planes with same orientation are defined by the standard three indices *h, k, l,* which determine the shape of a unit cell. Hence, the

different phases within a bulk or polycrystalline sample can be identified from the inter-planar *d*.

3.6.2.3 Mechanical components (Goniometer)

The main components of the goniometer, which is shown in the following figure, include a sample holder, a detector, and an x-ray tube. The reflection geometry used in all our measurements is that of the standard theta: 2-theta goniometer, within which the x-ray tube remains stationary throughout the scanning. For our MgB_2 and Al_2O_3 samples, the scan range was set to be 20˚-80˚ and the scan step size was 0.02˚, with a scan rate of 0.2˚/min. After each scan at a particular angle, the sample holder then moved by θ = 0.02˚, and the detector simultaneously moved by 2θ until the full scan range was completed.

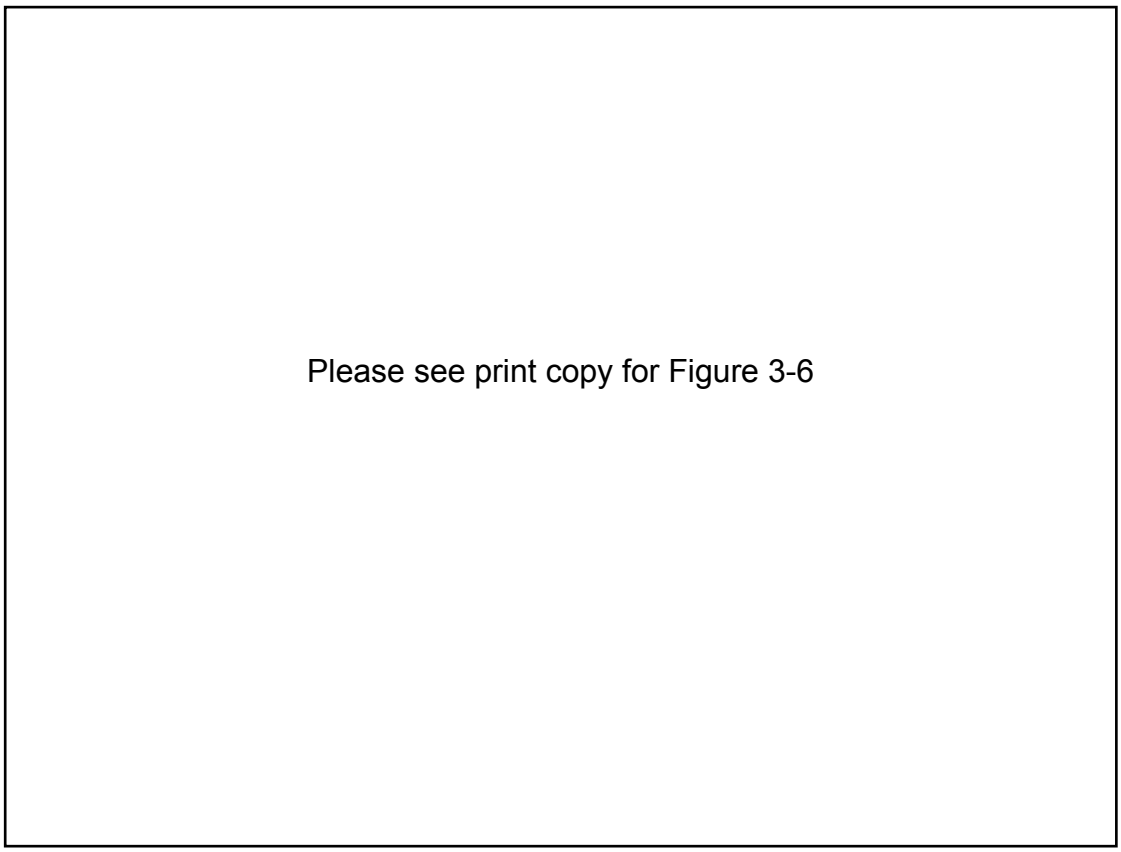

Fig. 3-6 Layout of the standard geometry of theta: 2-theta goniometer. Figure cited from [17].

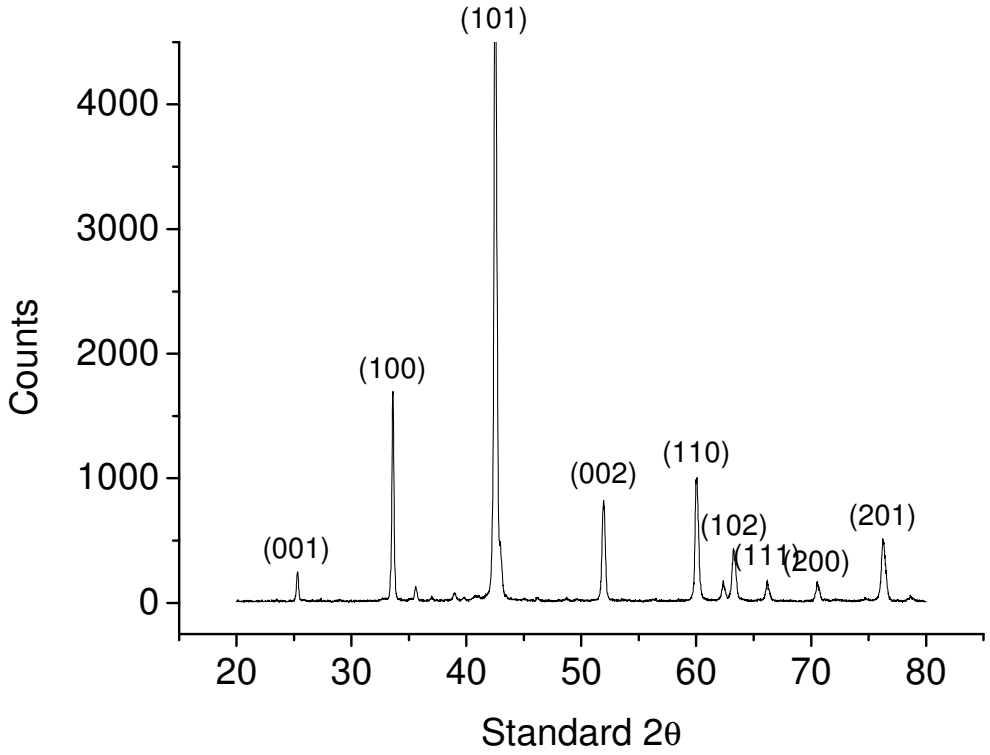

Fig.3-7 An XRD spectrum of the stoichiometric MgB_2 target shows detection of different MgB_2 lattice planes.

3.7 Magnetic and transport properties measurements

3.7.1 Resisitivity measurement by transport current method

A four probe method can be applied to determine the critical current of MgB_2 thin films. The sample is mounted on a brass sample holder, which provides sample support and a relatively large thermal mass for a stable sample temperature. A transport dc current is introduced by attaching current leads to both ends of the sample by silver paste. Voltage taps are attached onto the sample in between the current leads,

and as the current runs through the sample, the voltage across the sample is measured simultaneously in a PPMS-9T system (Quantum Design). The resistivity of the sample is measured as a function of temperature, and field can be applied in both perpendicular and parallel directions to the surface of the sample by changing the orientation of the sample on the brass holder.

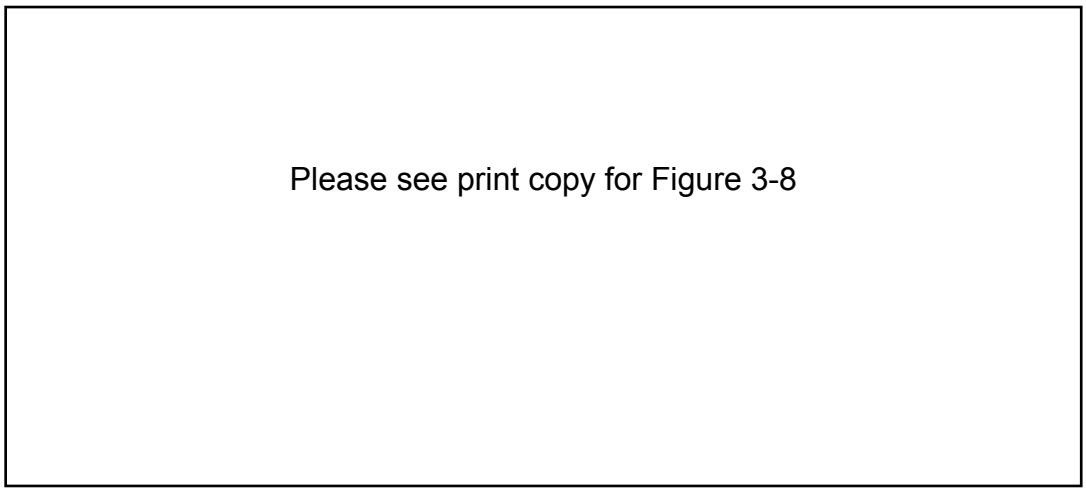

Fig.3-8: Illustrations of four-probe set-up for transport measurement in the Physical Properties Measurement System (*PPMS*). *The left is the B⊥/film case and the right B//film Figure cited from* [4].

3.7.2 DC-magnetization method

The critical temperature of MgB_2 superconducting films and the field dependence of the magnetic moment were obtained using the dc-magnetization method in a Quantum Design Magnetic Properties Measurement System (MPMS). Since the induced magnetization measurement does not require current leads and attachment of voltage taps, much smaller samples can be tested, and all parts of the superconducting sample contribute to the magnetic moment, unlike the transport method in which only chains

of connected grains that provide current paths contribute to determining the critical current density.

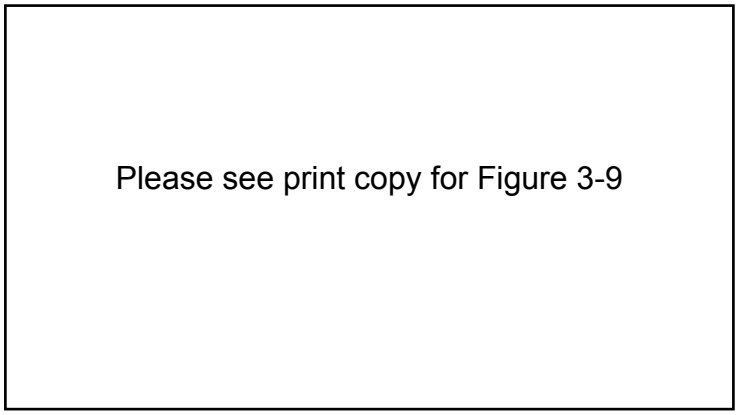

Fig. 3-9 Magnetic Property Measurement System (*MPMS*) *from Quantum Design. Figure cited from* [4].

A SQUID magnetometer in the system with a sensitivity as low as $1\times10^{-4}Am^{-1}$ is used to measure the magnetic moment of the superconducting sample. A magnetic field of 25 Oe is applied perpendicularly to the surface of the sample. The accuracy of the applied field depends on the alignment of the sample and has a minimum deviation of 2mT due to the hysteresis in the magnet.

To avoid magnetic flux being trapped in the sample while it passes through the magnet during insertion, the field inside the system is first set back to zero, so that the sample will be in its virgin state, and then the temperature is cooled down to 5K, the temperature at which the measurement takes place. The applied field now is ready to reach up to the desired value for the measurement. The magnetic moment is measured stepwise for increasing and decreasing field. The maximum field value which we used

for our experiments was 5T. A magnetic field is applied in the opposite direction to reverse the field portrait in the sample after the field is switched off, and the magnetic moment is now measured for the same field values for decreasing field. J_c at different temperatures can be determined from the magnetization difference ΔM using the Bean-model relation:

$$J_c = \frac{\Delta M}{a \times b \times d} \times \frac{6a}{(3a - b)b} \ .$$

The letters a, b and d refer to the length, width, and thickness of the superconducting part of the sample.

Reference

[1] C Ferdeghini, V Ferrando, G Grassano, W Ramadan, E Bellingeri, V Braccini, D Marr´e, P Manfrinetti, A Palenzona, F Borgatti, R Felici, and T.-L. Lee, "Growth of c-oriented MgB_2 thin films by pulsed laser deposition: structural characterization and electronic anisotropy," *Supercond. Sci. Technol.,* vol. 14, pp. 952–957, 2001.

[2] Dave H. A. Blank, Hans Hilgenkamp, Alexander Brinkman, Dragana Mijatovic, Guus Rijnders, and H. Rogalla, "Superconducting Mg–B films by pulsed-laser deposition in an *in situ* two-step process using multicomponent targets," *APPLIED PHYSICS LETTERS,* vol. 79, pp. 394-396, 2001.

[3] Dragana Mijatovic *, Alexander Brinkman, Guus Rijnders, Hans Hilgenkamp, Horst Rogalla, and D. H. A. Blank, "Superconducting thin films of MgB_2 by pulsed-laser deposition," *Physica C* vol. 372–376 pp. 1258–1261, 2002.

[4] Y. Zhao, "Fabrication and Characterization of Superconducting PLD MgB_2 Thin Films," *PhD Thesis,* 2005.

[5] D. B. Chrisey and G. K. Hubler, "Pulsed Laser Deposition of Thin films," 1994.

[6] W. Z. Yu, "Theory of fabrication, techniques and application of thin films," 1998.

[7] O. S. Heavens, "Thin Film Physics," 1970.

[8] G. D'Amico, A. Di Trolio*, A. Morone, S. Orlando, and A. Santagata, "Optical characterization of magnesium diboride plasma plume induced by pulsed laser ablation," *Applied Surface Science* vol. 208–209, pp. 96–100, 2003.

[9] S. Amoruso, M. Armenante, R. Bruzzese, N. Spinelli, R. Velotta, M. Vitiello, and X. Wang, "Pressure effects during excimer laser ablation of magnesium diboride targets," *Applied Surface Science,* vol. 208-209, pp. 39-44, 2003.

[10] V.N. Tsaneva*, N.A. Stelmashenko, I.N. Martev, Z.H. Barber, and M. G. Blamire, "Characterisation of the optical emission of the plasma plume during pulsed laser deposition of superconducting MgB_2 thin films," *Vacuum* vol. 69 pp. 267–271, 2003.

[11] G Grassano, W Ramadan, V Ferrando, E Bellingeri, D Marr´e, C Ferdeghini, G Grasso, M Putti, P Manfrinetti, A Palenzona, and A. Chincarini, "As-grown magnesium diboride superconducting thin films deposited by pulsed laser deposition," *Supercond. Sci. Technol. ,* vol. 14, pp. 762–764, 2001.

[12] Yue Zhao, Mihail Ionescu, Alexey V Pan, Shi Xue Dou, and E. WCollings, "*In situ* annealing of superconducting MgB_2 films prepared by pulsed laser deposition," *Supercond. Sci. Technol. ,* vol. 16 pp. 1487–1492, 2003.

[13] Yue Zhao, Mihail Ionescu, Josip Horvat, and S. X. Dou, "Comparative study of in situ and ex situ MgB_2 films prepared by pulsed laser deposition," *Supercond. Sci. Technol. ,* vol. 17, pp. S482–S485, 2004.

[14] Oatley and C. William, "The scanning electron microscope " 1972.

[15] K. D. Leaver and B. N. Chapman, "Thin Films," 1971.

[16] "PANalytical," *http://www.panalytical.com/index.cfm?pid=314*, 2007.

[17] E. D. Specht, C. J. Sparks, and C. J. McHargue, "Determination of residual stress in Cr-implanted Al_20_3 by glancing angle x-ray diffraction," *Appl. Phys. Lett.* , vol. 60 pp. 2216-2218, 4 May 1992.

Chapter 4

Working pressure optimization of off-axis deposition of *in situ* MgB_2 films

Introduction

MgB_2 has so far been considered to have the highest transition temperature among all the non-oxide materials, and its fabrication in the form of thin films is regarded as of significant importance for a large area of electronic applications. Different methods have been carried out and proved to provide fairly good quality MgB_2 thin films. In this chapter, we describe the fundamental techniques of off-axis PLD, report on the effects of vacuum conditions and introduce the use of argon background gas at various pressures: 80mTorr, 120mTorr, and 160mTorr with observation of the physical changes in the plasma plume during the laser ablation process.

Production of thin film by off-axis deposition

In the traditional on-axis deposition geometry, the substrate surface is placed parallel to and facing directly in front of the target surface, and, with no doubt, this will achieve a higher growth rate in the deposition process. However, this geometry cannot yet be considered optimum for producing high quality thin film, owing to the

drawbacks in the surface quality, which gives rise to the application of off-axis deposition geometry. The off-axis deposition geometry was first introduced in sputtering deposition to avoid the film coming into contact with too many fragments and particulates sputtered from the target.

Fundamental principles of the off-axis deposition technique

Big fragments and particulates of the target material are always generated during PLD deposition. However, the droplets usually come straight off at nearly a right angle to the target surface, and the trajectory of these heavy species usually will not be affected by the background gas. Therefore, to prevent these droplets that are detached from reaching the film surface, in off-axis geometry, the substrates are usually placed at an angle of 90º instead of facing the target. The basic mechanism for off-axis deposition is the scattering of light species. The light species can easily be scattered and travel in a randomized path through interaction between the plume and the background gas, whereas the trajectory of big fragments and droplets will not be deflected much by the background gas, so that they pass by the film surface. As a result, dramatic improvement of the film surface roughness is observed by using off-axis deposition [1]. There are two main issues that arise in connection with the off-axis geometry which may prevent the successful deposition of good quality MgB_2 thin films and prevent good superconducting properties:

(1) Significant reduction of the deposition rate:

In the deposition process involving active elements, a longer deposition time induces a higher chance of reactions between the fresh elements and oxygen, which could also be absorbed by the fresh film surface, and increases the level of impurities such as MgO. This is particularly true for magnesium from the Mg-B target, which is highly reactive with oxygen.

(2) Difficulty in controlling the uniformity of the growing film:

During deposition, different parts of the substrate are at different distances from the target, so the deposition rate could therefore be very different in different parts of the substrate. Ions or atoms with different masses will be scattered to different extents in the argon atmosphere. As a result, due to the special off-axis geometry, the lighter particles which experience stronger scattering will be deposited on the substrate on the side nearer the target, and the heavier particles will be concentrated on the parts that are further away from it, reducing the homogeneity.

As for the first issue, the base vacuum was evacuated to at most 10^{-8} Torr before each run to reduce the level of impurity molecules present in the background gas. This can generally lower the amount of impurity contamination of the films. The second issue was solved by placing the substrate at a position closer to the centre of the plume and nearer to the target so as to increase the homogeneity. As there has been limited work carried out on off-axis deposition of MgB_2 films so far, our analysis is mostly based on the results from the present work. A more detailed description of off-axis deposition will be provided in chapter 5.

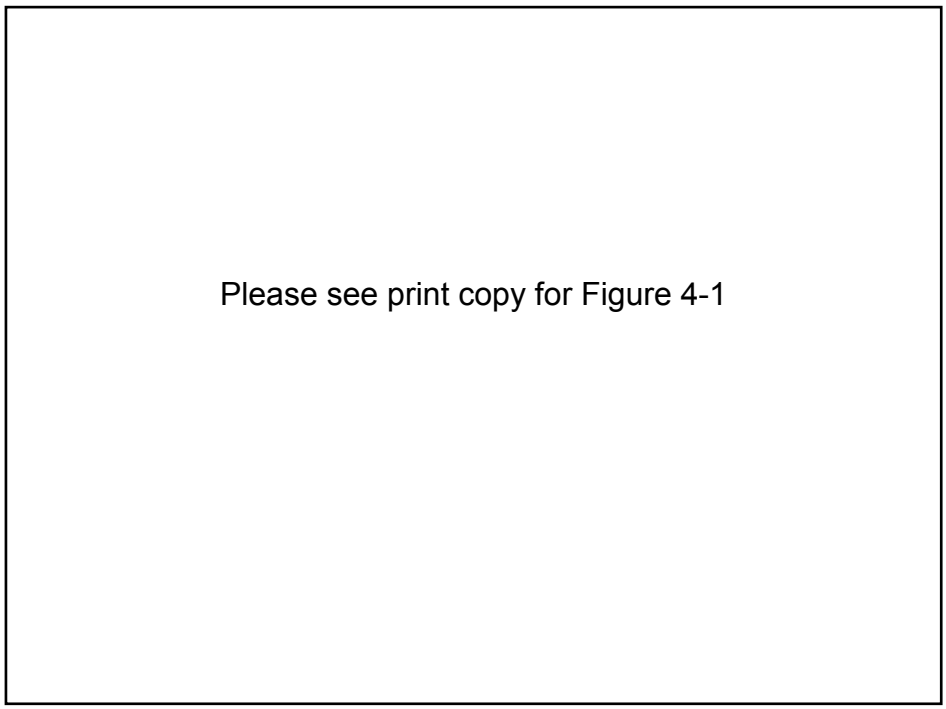

Fig. 4-1 Graphical representations of traditional on-axis PLD system. Figure cited from [2].

Experiment

The full description of the PLD work is given in Chapter 5 and here we mainly concentrate on the preparation and the effects of vacuum and deposition pressure. The PLD process was conducted in a spherical chamber with a volume of ~52 L (see Fig. 4-1). Before deposition, the chamber was evacuated to a base vacuum of ~8×10^{-8} Torr and then filled up with pure argon to a pressure of 120 mTorr to provide the background gas. The substrate was heated up to 250 °C and kept stable at the deposition temperature. The targets used in the experiments were stoichiometric MgB_2 (84% density) and high purity magnesium (99.9%). Both were set on a rotating

carrousel in the chamber, as shown in Fig. 4-2, with their target surfaces perpendicular to the substrate surface. The substrates used were sapphire *c*-cut Al_2O_3-C (0001) with a thickness of ~0.33 mm, and every substrate used in each deposition was cut manually to an average area of about 7×5 mm^2. The substrate was mounted on the edge of the heater with silver paste, and the target to substrate distance was 23mm as measured from the centre of the substrate.

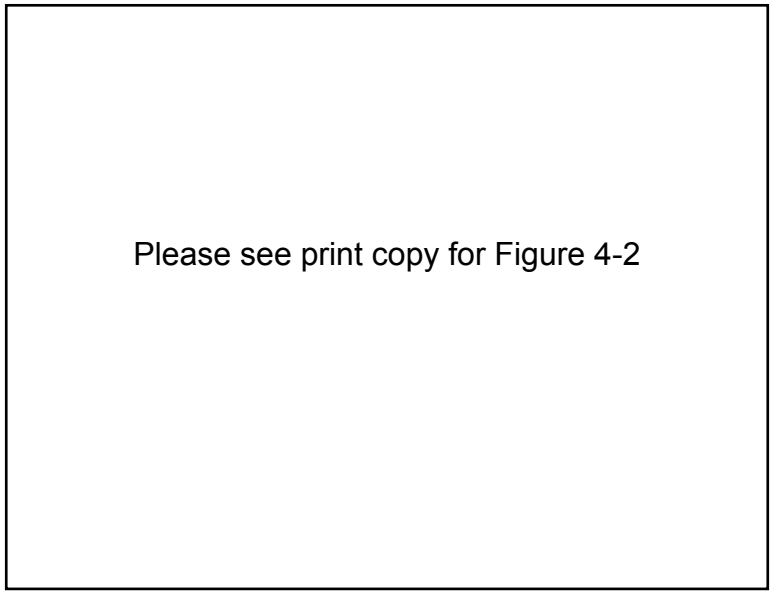

Fig. 4-2 Details of the geometry of the interior deposition chamber. Figure cited from [1].

Effect of the vacuum conditions and the deposition pressure

For MgB_2 films to be deposited on the substrate surface, a good vacuum has to be created inside the chamber before deposition. Different methods have been carried out and proved to provide fairly good quality MgB_2 thin films. As-grown superconducting

films are particularly useful for the fabrication of junctions and multi-layer devices [3], and can be easily produced by pulsed laser deposition in argon buffer gas [4]. The main difficulty of this process lies in the high volatility of magnesium. The prospective solution to this is the control of the argon buffer gas in the MgB_2 film growth process by PLD [4, 5].

It has also been found that a blue plasma plume is important for the production of superconducting films [6, 7], and the interactions between the background gas and the ablated material have been studied for different materials [5]. The effect of the vacuum conditions on the ablation induced from a stoichiometric MgB_2 target is shown in Figure 4-3. It can be seen that there is a significant effect on the plume developed during deposition: the plume is weak and appears greenish at a base vacuum of 7×10 mTorr, whilst at a better vacuum below 9×10 mTorr, the plume looks stronger and is blue in color.

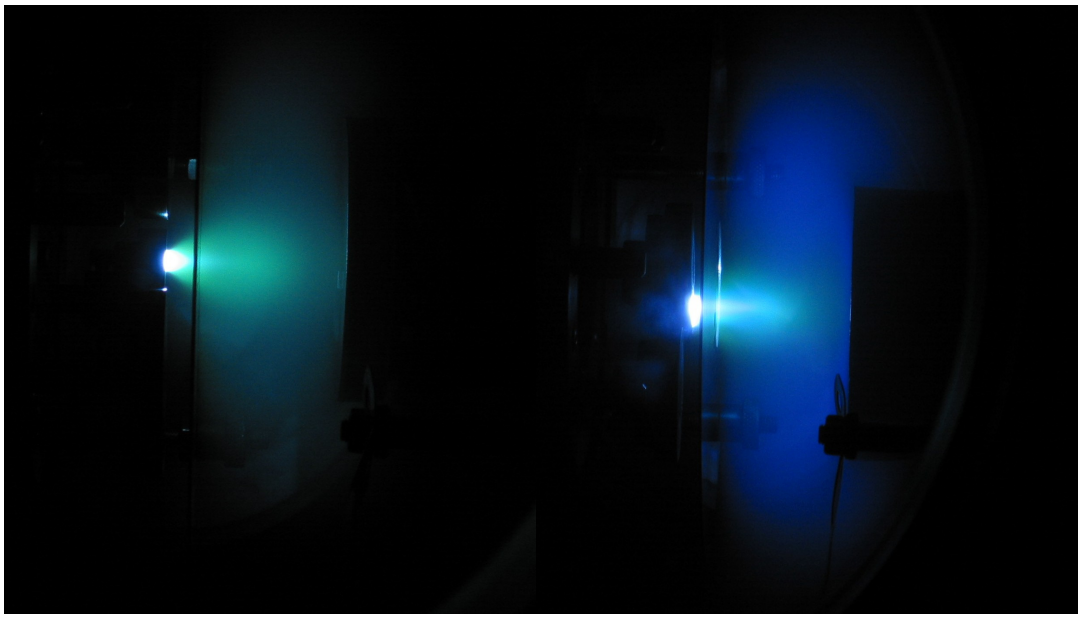

Fig. 4-3 Ablating MgB_2 target in a 120 mTorr argon pressure. Left, the base vacuum was $7x10^{-7}$ Torr, and right, $9x10^{-8}$ Torr. The laser energy was 500 mJ/pulse.

Results and Discussion

Based on this observation, our experiments described in following chapters were all carried out after a vacuum of nearly $9x10^{-8}$ Torr was created inside the chamber. The next step was to change the argon pressure and see if there is a significant influence on the quality of the sample. Figure 4-4 shows how the laser plumes from targets of pure magnesium and stoichiometric MgB_2 change with different argon deposition pressures. It can be seen clearly that the outskirts of the plume expand and turn from a pale green color to bright blue.

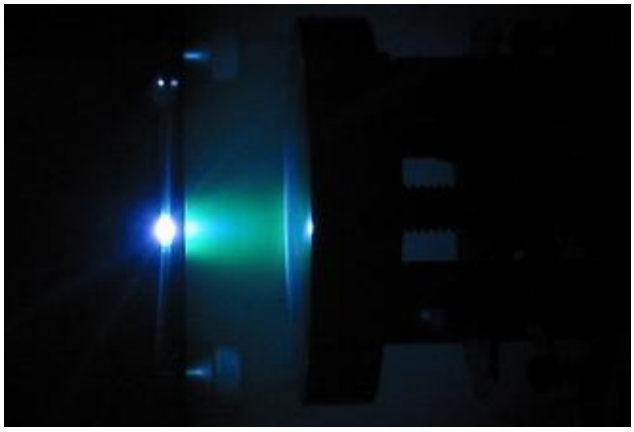

(a) *Mg target; 80mTorr argon atmosphere.*

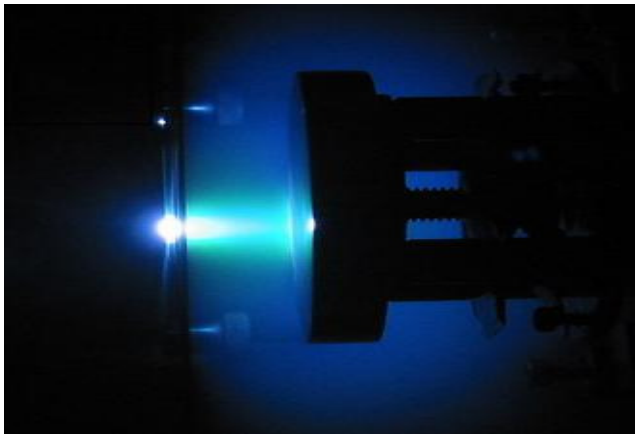

(b) *Mg target; 120mTorr argon atmosphere.*

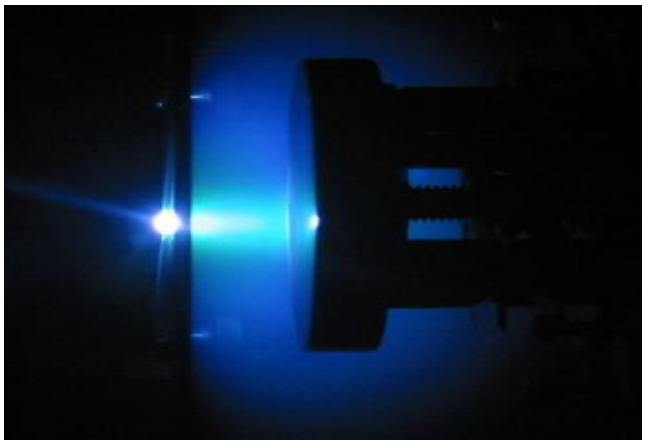

(c) *Mg target; 160mTorr argon atmosphere.*

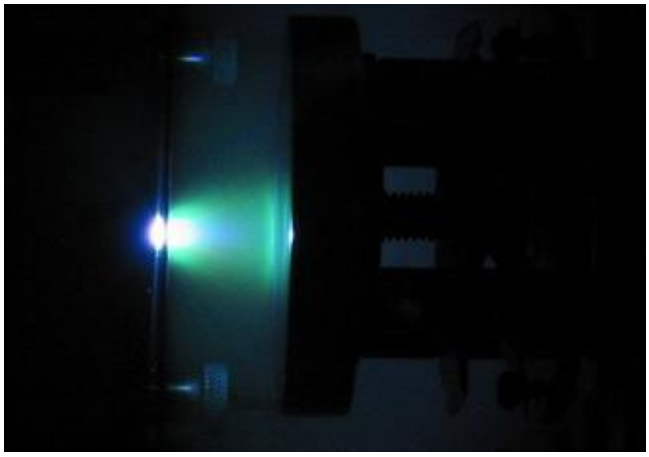

(d) *MgB_2 target; 80mTorr argon atmosphere.*

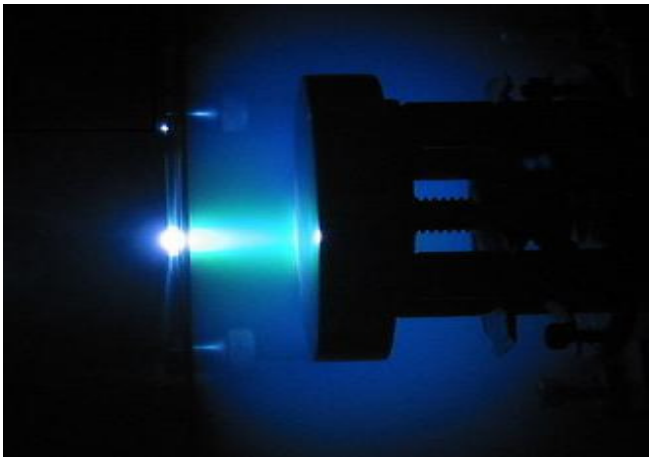

(e) *MgB_2 target; 120mTorr argon atmosphere.*

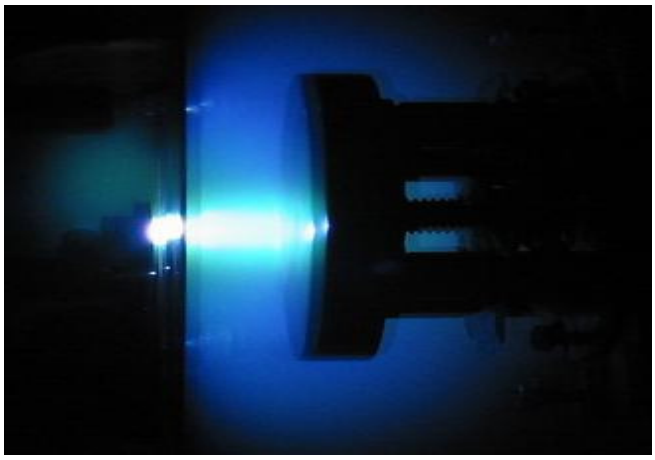

(f) *MgB_2 target; 160mTorr argon atmosphere.*

Fig. 4-4 Laser ablation from Mg and MgB_2 targets at different argon pressures.

The change in the plume emission related to the Ar gas pressure could be because of that the shock wave formation influences the distribution of kinetic and thermal energies between the plume and the ambient gas, causing the plume to heat up and results in enhancement of excitation and ionization of the plume atoms [8].

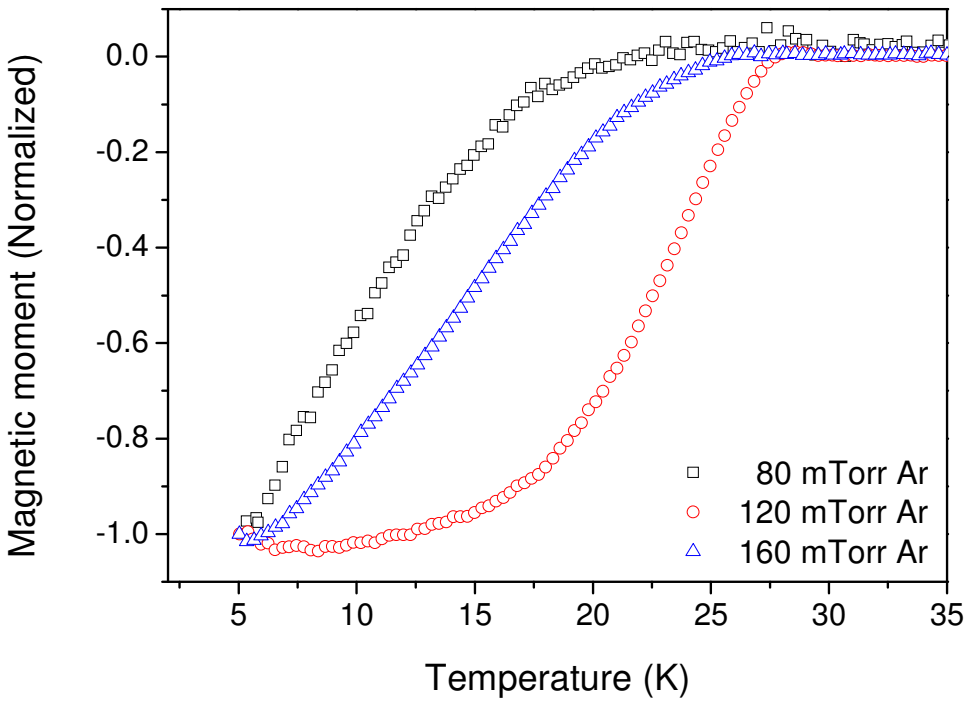

Fig. 4-5 Magnetic T_c curves of MgB_2 thin films at different Ar deposition pressures.

In Figure 4-5, the T_c of our 3 separate samples was measured after a short *in situ* annealing process at a moderate temperature and was found to be highest in the sample deposited at 120mTorr Ar pressure. The x-ray diffraction patterns of these samples are shown in Figure 4-6. Note that a higher level of impurities is observed at higher Ar pressure. From these results we found that 120mTorr Ar is the optimum pressure in the present experiment. It is predicted that energetic particles can cause re-sputtering for the most volatile elements, like Mg, upon impact on the substrate

surface and significantly influence the stoichiometry of the growing film [5]. Thus at larger Ar pressure, the ambient gas can slow down the plume, reduce the release of Mg from the deposit and increase the extent of excited or ionised species arriving the surface to enhance the surface mobility which favours film growth. However, the shock wave effect will tend to occur at larger distance from the target for lower Ar pressure due to its distance–related pressure threshold nature. As a result, there is a best buffer pressure, as a function of the target-to-substrate distance. Based on our observations in this experiment, we assume that 120mTorr Ar is the most suitable buffer pressure for our target-to-substrate distance of 25mm, and which optimizes the amount of plume atoms with lower kinetic energy and excited higher degree.

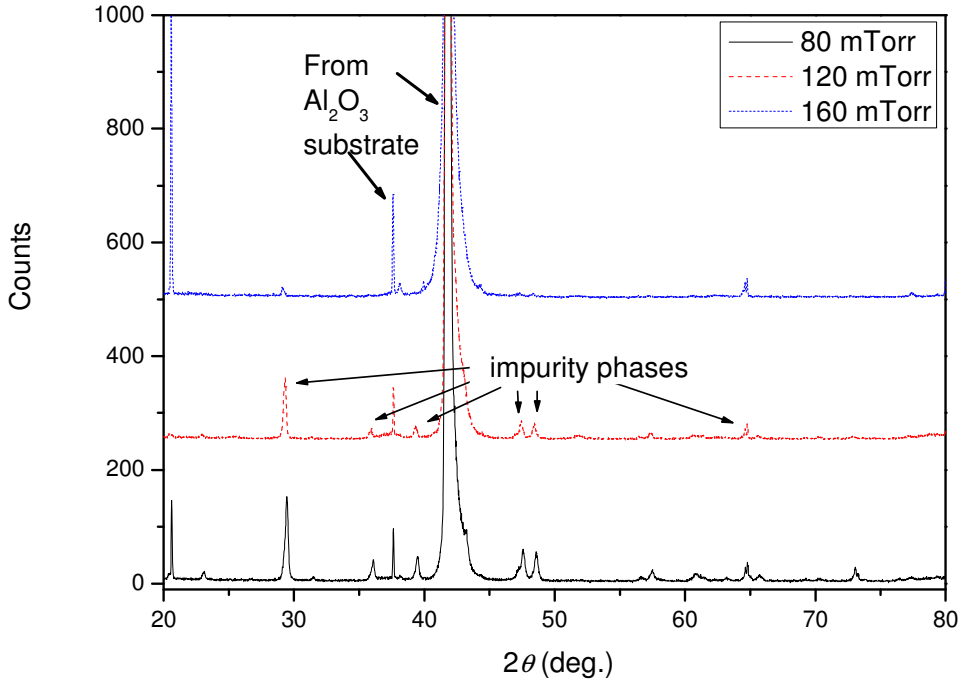

Fig 4-6 XRD diffraction spectra of MgB_2 thin films at different deposition pressures.

No X-ray diffraction lines of MgB_2 were detected for these samples, meaning that the superconducting MgB_2 phase only exists in very small grains or in an amorphous-like structure.

Conclusion

The effect of argon pressure on the plasma plume was investigated and the vacuum required before introducing the argon gas was determined for PLD of MgB_2 to be $9x10^{-8}$ Torr. Comparing the present $T_c(P)$ data and other results obtained in this work, we notice that the working pressure of argon has a significant influence on the superconductivity of our MgB_2 thin films. We found the optimum working pressure of argon for MgB_2 thin film deposition to be 120mTorr. Our thin films which will be discussed in the following chapters were deposited under this pressure.

Reference

[1] Yue Zhao, Mihail Ionescu, J. Horvat, and S. X. Dou, "Off-axis MgB_2 films using an *in situ* annealing pulsed laser deposition method," *Supercond. Sci. Technol.,* vol. 18, pp. 395–399, 2005.

[2] Y. Zhao, "Fabrication and Characterization of Superconducting PLD MgB_2 Thin Films," *PhD Thesis,* 2005.

[3] Kenji Ueda and M. Naito, "Growth of Superconducting MgB_2 Thin Films," *cond-mat/0203181,* vol. 45.

[4] G Grassano, W Ramadan, V Ferrando, E Bellingeri, D Marr´e, C Ferdeghini, G Grasso, M Putti, P Manfrinetti, A Palenzona, and A. Chincarini, "As-grown magnesium diboride superconducting thin films deposited by pulsed laser deposition," *Supercond. Sci. Technol. ,* vol. 14, pp. 762–764, 2001.

[5] S. Amoruso, M. Armenante, R. Bruzzese, N. Spinelli, R. Velotta, M. Vitiello, and X. Wang, "Pressure effects during excimer laser ablation of magnesium diboride targets," *Applied Surface Science,* vol. 208-209, pp. 39-44, 2003.

[6] G. D'Amico, A. Di Trolio*, A. Morone, S. Orlando, and A. Santagata, "Optical characterization of magnesium diboride plasma plume induced by pulsed laser ablation," *Applied Surface Science* vol. 208–209, pp. 96–100, 2003.

[7] V.N. Tsaneva*, N.A. Stelmashenko, I.N. Martev, Z.H. Barber, and M. G. Blamire, "Characterisation of the optical emission of the plasma plume during pulsed laser deposition of superconducting MgB_2 thin films," *Vacuum* vol. 69 pp. 267–271, 2003.

[8] N. Arnold, J. Gruber, and J. Heitz, "Spherical expansion of the vapor plume into ambient gas: an analytical model " *Applied Physics A: Materials Science & Processing,* vol. 69, pp. S87-S93, 1999.

Chapter 5

Optimization of off-axis in situ MgB_2 films using different annealing conditions

In this chapter, we report on work carried out to optimize the annealing conditions following an off-axis deposition of MgB_2 thin films. A series of MgB_2 precursor films were deposited on the same sapphire substrates prepared and under the same deposition conditions established in chapter 4, but followed by *in situ* annealing with different conditions under an argon gas pressure of 760 Torr inside the deposition chamber. The influence of two important annealing parameters, which are the holding time, τ_{ann}, and the sintering temperature, T_{ann}, on the superconductivity were investigated. The optimal annealing, conditions were those giving the best superconducting film, with both magnetic and resistive T_c of 34K-35K and transition widths ΔT_c of 6.2 K and 0.2 K in the magnetic M-T and resistivity ρ-T measurements, respectively. Resistivity measurements in different applied fields provided evidence that the film had a strongly suppressed anisotropic ratio. A high critical current density (J_c) of ~ 0.1 MA/cm^2 at a magnetic field near 5T at 15K was detected, suggesting potential applications of this film with low energy dissipation at high temperature. The $H_{c2}(0)$ values were worked out by extrapolation from the BCS formula, and the H_{c2} anisotropic factor η turned out to be nearly equal to unity. Microstructural analysis using X-ray diffraction indicates that the film is highly c-oriented, with mainly MgB_2 (002) peaks observed in the XRD spectrum.

Introduction

Since the superconductivity of MgB_2 was discovered in 2001 [1], considerable efforts have been made to prepare MgB_2 superconductors in the form of thin films of ~ 1μm thickness for microelectronic applications. Various methods, such as pulsed laser deposition (PLD), molecular beam epitaxy (MBE) [2], chemical vapour deposition (CVD) [3], and hybrid physical-chemical vapour deposition (HPCVD) [3], have been tested to produce commercially available MgB_2 thin films. But the PLD method is comparatively simple and technically capable of producing multilayer films. In accordance with the previous literatures on PLD [4-9], non-superconducting Mg-B or B precursor films were commonly prepared by deposition from stoichiometric MgB_2 or Boron targets. These films must subsequently be annealed at very high temperature in order to complete the formation of the MgB_2 superconducting phase with an epitaxial-like structure, which is favourable for carrying high current densities in the superconducting state.

Studies on *in situ* and *ex situ* annealed PLD films obtained by the PLD method show that the *in situ* annealed films have considerably suppressed T_c of ~25 K due to oxygen contamination and incomplete crystallization whereas T_c above 39 K has been obtained in *ex situ* annealed PLD films [9-11]. However, the *in situ* procedure using a PLD system requires simpler equipment than that for the *ex situ* procedure and is more suitable for application in multilayer junctions. Literature reviews on the common type of on-axis deposition for both *in* and *ex situ* films prepared by the PLD method have found that the surface quality of these films is very poor, due to many

sub-micron and micron sized particulates attached to the film surfaces [11]. The bad surface quality of this type of film hinders its applications in superconducting junctions and other electronic devices which require uniform and homogeneous interfacial contact between layers.

To avoid the splashing effect which brings the melted droplets or detached fragments from the target to the precursor and reduces the surface smoothness, our group has chosen to apply an off-axis geometry for pulsed laser deposition of MgB_2 thin films [9], which places the normal axis of the substrate surface perpendicular to that of the target surface. Improvements in the surface roughness of films produced by the off-axis method have been confirmed by microstructure detection. One drawback in the off-axis geometry is the reduced growth rate. An increased deposition time seems to be necessary, but bearing in mind that magnesium is very volatile and reactive with oxygen, so as to create the insulating agent MgO throughout the entire procedure, a reasonably high purity vacuum (~8×10^{-8} Torr) must be created before deposition, and the length of time for deposition and annealing must be deliberately decided.

In regard to the annealing conditions, T_c suppression due to poor crystallization always results if the duration is too short, but non-superconducting or phase disrupted films are obtained if annealing is kept going for too long. Optimal annealing conditions for fabrication of *in situ* MgB_2 thin films need to be found before MgB_2 thin films can be produced on a large scale for commercial use. Only one method of producing off-axis *in situ* MgB_2 thin films has been reported in the literature until now

[9], and the samples have a suppressed T_c ~32K. The preparation of *in situ* MgB_2 thin films using off-axis pulsed laser deposition still needs to be optimized.

Experiment

The laser beam was generated by an excimer laser system (Lambda-Physik) operating on KrF gas (λ = 248 nm, 25ns). The laser beam was first passed through a diaphragm to form a rectangular spot and then focused to an elliptical spot of ~7 × 1.5 mm^2 on the target 25mm away from the centre of the substrate by a 700 mm focal length spherical lens. The voltage was adjusted and monitored from time to time during deposition to give an average energy output of 498-522 mJ for each pulse which was then reduced to ~250mJ after passing through the diaphragm, while the replication frequency of the pulses was set to be stable at 10 Hz. The laser beam first hit the Mg target for 3 mins to create a magnesium vapour inside the chamber to reduce the level of contamination by oxygen and then the MgB_2 target for 1 min. The substrate was shielded from the plume during this process.

Deposition was conducted immediately afterwards by sliding off the shielding screen, so that the axis through the surface of the substrate was directly aligned in the centre of the plume, which was generated perpendicularly from the MgB_2 target surface. The time for this deposition was 15 minutes (for a film of ~500nm thickness). Since the films obtained from these experiments were subjected to *in-situ* annealing after the MgB_2 deposition, an additional magnesium layer from the pure Mg target was also deposited onto the fresh film surface for 7mins to compensate for the magnesium loss

through vaporisation by high temperature conduction during the heating up and annealing.

When the deposition was finished, the vacuum was replaced with high purity argon gas with a pressure up to 760 Torr in 3 mins 40s. The reason for this was to provide a high vapour pressure so as to avoid too much Mg loss from near the film surface as the substrate temperature was quickly ramped up. The substrate was heated up to the chosen annealing temperature T_{ann} in 12 mins and maintained at that temperature for the pre-set sintering time τ_{ann}. Then the power was switched off automatically, and the sample was freely cooled down to room temperature at a rate of ~ 55 °C min^{-1}.

To investigate how the quality of our MgB_2 thin films could be improved by an optimal experimental procedure, the same deposition process was repeated but followed by different annealing conditions. T_c of the films was obtained by direct current (DC) magnetization measurements on a SQUID magnetometer system (MPMS, Quantum Design). The sample was mounted on a straw and placed inside the magnetometer, within which an NbTi superconducting coil acting as a magnet was used to apply a magnetic field perpendicular to the sample surface. The system was initially cooled down by liquid helium to 5 K with no applied field (ZFC), then the temperature range was set from 5 K to 38 K, and scans of the magnetic moment of the sample were taken at intervals of every half minute.

Optimization of annealing condition

In this experiment, we first varied the sintering time τ_{ann}, but the annealing temperature T_{ann} was set at a constant 650˚C for the precursor films, until a set of data with significant changes in the superconductivity was observed. The τ_{ann} corresponding to production of the best superconducting film was chosen and applied to other precursor films, which would then be sintered for the same duration but with the annealing different T_{ann}. Another set of data based on the different selected T_{ann} was also extracted, and from these data we tried to establish the optimal annealing conditions and explain how the superconducting properties were affected by the annealing conditions.

Results and Discussion

Figure 5-1(a) shows the magnetic T_cs of a set of MgB_2 films with different τ_{ann} at a fixed T_{ann} of 650˚C. The T_cs were measured with an MPMS system under a perpendicular applied field B_a of 25 Oe. The magnetic moment (emu) of these samples at low temperature (5K-10K) was on the order of 10^{-2} to 10^{-3} (Am^2). It can be seen that the T_c gradually increases with τ_{ann}, but it began to drop when the τ_{ann} exceeded 11 mins. We also tested a film with a τ_{ann} of 90mins, but only a very weak signal of induced magnetic moment was observed at low temperature. It was realised that magnesium could easily undergo a substantial reaction with the background gas and cause phase disruption in the MgB_2 during the annealing process, with the high volatility of the magnesium leading to formation of other phases such as MgB_4, etc. This is probably the reason why weaker superconductivity was generally observed for the samples annealed for a much longer τ_{ann}. Analysis of the microstructure using x-ray diffraction shows almost no peaks corresponding to superconducting MgB_2 for the

films with τ_{ann} outside the range of 5 to 11 mins, but instead, there are many unknown peaks, which indicate the presence of other unknown phases. This suggests that there was incomplete crystallization or re-evaporation of Mg over a long sintering time, as expected.

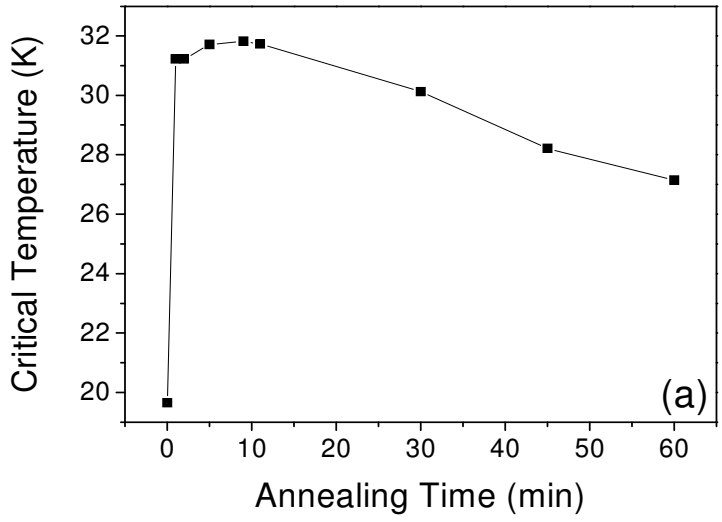

Fig. 5-1 (a) *Change of T_c against the annealing time.*

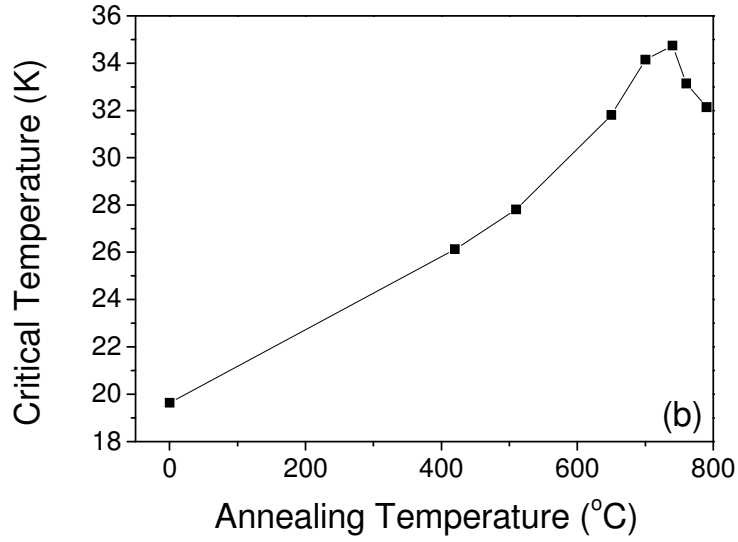

Fig. 5-1 (b) *Change of T_c against the annealing temperature.*

Further analysis of the magnetic transition in our samples was conducted and is shown in Figure 5-2. From Figure 5-2(a), the transition curves of the films obtained with τ_{ann} < 11 mins have not only higher T_c, but also have a sharper transition ΔT, whereas films with longer annealing than this have lower T_c and more broadened ΔT. The narrower ΔT of the former films implies that they are more homogeneous. The reason for broadening in the *M-T* transition is probably the formation of $Mg_{1-x}B_2$ (x < 1) or substitution of boron by oxygen leading to $MgB_{2-x}O_x$. These less purity phases have lower T_c, broadening the transition in the *M-T* measurements. The film which has highest T_c, ~32K, has a τ_{ann} of 9 mins, and the films with τ_{ann} from 5 to 11 mins have T_c slightly higher than those with τ_{ann} < 5mins. The transition widths ΔT of these two types of film are between 7 and 12K. The films with τ_{ann} > 11 mins have a considerably broader ΔT around 16K. The higher T_c would be consistent with the consideration that the grain size increased after longer annealing. The ΔT remains at a reasonable sharpness within this τ_{ann} range of 5 to 11mins and is capable of coexisting with higher T_c. We conclude that the optimal annealing time is between 5 and 11mins.

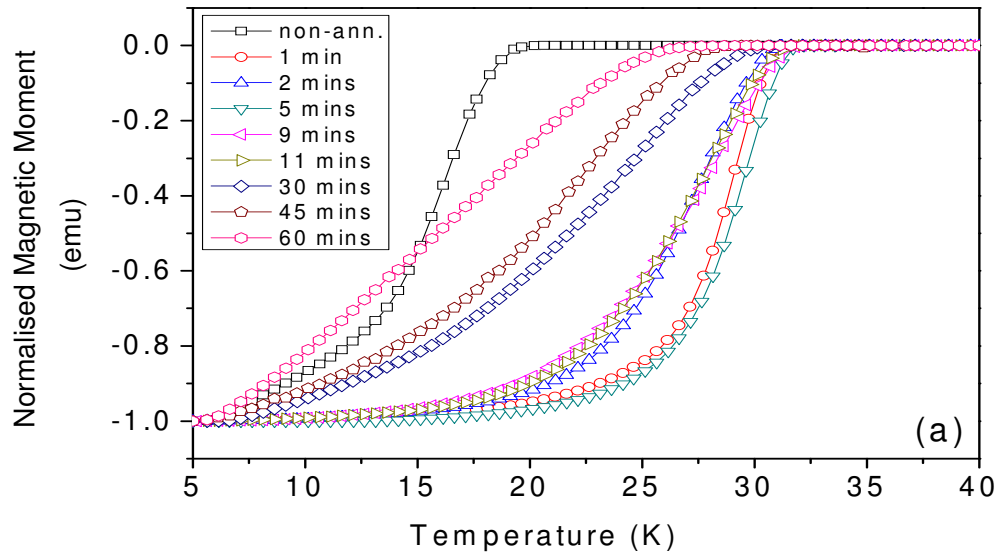

Fig. 5-2(a) *Normalized magnetic transition curves of samples with different annealing time* τ_{ann}.

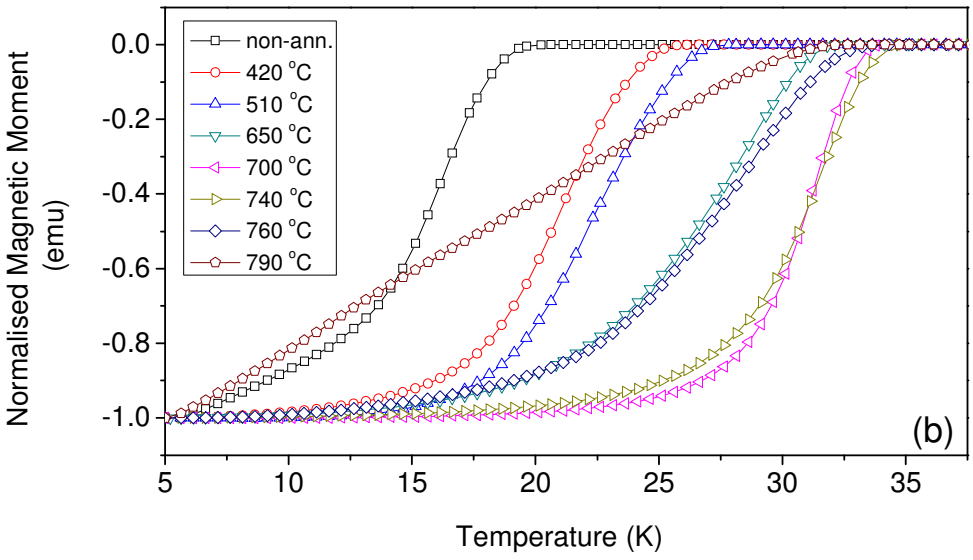

Fig. 5-2(b) *Normalized magnetic transition curves of samples with different annealing temperature* T_{ann}.

Based on these observations a limit should be put on this annealing parameter, since higher T_c films are obtained under this optimized τ_{ann}. The suppression of T_c should be mainly attributed to the increase in the amount of impurities that are formed when the sample is kept longer at high temperature. The film without annealing was examined through MPMS and shows a significant suppression of T_c, due to poor crystallization. Nevertheless, the overall annealing procedure should be as short as possible to avoid evaporation of Mg out of the film.

A similar trend of T_c change, shown in Figure 5-2(b), was revealed with films prepared at different annealing temperatures for the same duration, τ_{ann} = 9 mins. In this trend, the samples were heated up to different T_{ann} in 12 minutes and were held at that temperature for 9 mins throughout the entire annealing process. The heating rate in this case was slightly different for each sample, but the major influence on the superconducting properties came from the increased T_{ann}. From Figure 5-2(b), the T_c increases with T_{ann} up to 740˚C, at T_{ann} > 740˚C, the transition of the curves broadens explicitly, indicating disruption to the MgB_2 phases at over high sintering temperature. In this part of the work, the films obtained with the best superconductivity are #280806 (9 mins, 700˚C) and #131206 (9 mins, 740˚C), with $T_{c\ onset}$s of 34.2K and 34.8K, respectively, which are among the highest $T_{c\ onset}$s of all the *in situ* MgB_2 thin films reported so far. The increase in T_c may indicate improved crystallinity and grain growth at higher sintering temperature.

Since the substrates were cut manually, the size of these samples may be slightly different. In order to investigate the strength of the superconductivity of all these films,

graphs of the T_c curves were also plotted in term of magnetization and are shown in Figure 5-3. The volumes of the samples were worked out by measuring the dimensions of each individual sample. A JOEL JSM-6460A scanning electron microscope was employed for thickness measurement of the samples.

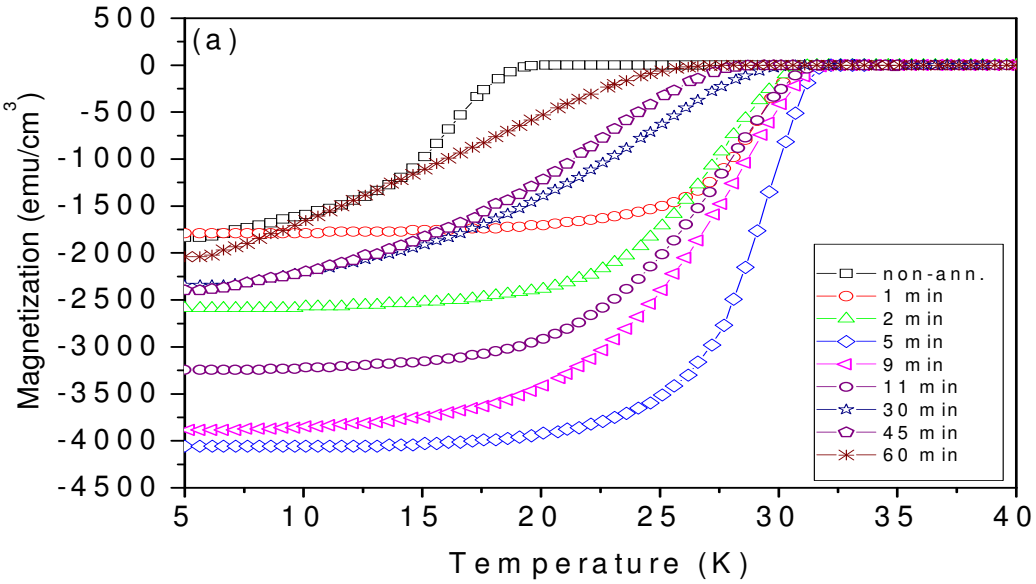

Fig. 5-3 (a) *Transition curves of magnetization against temperature for* τ_{ann} *series.*

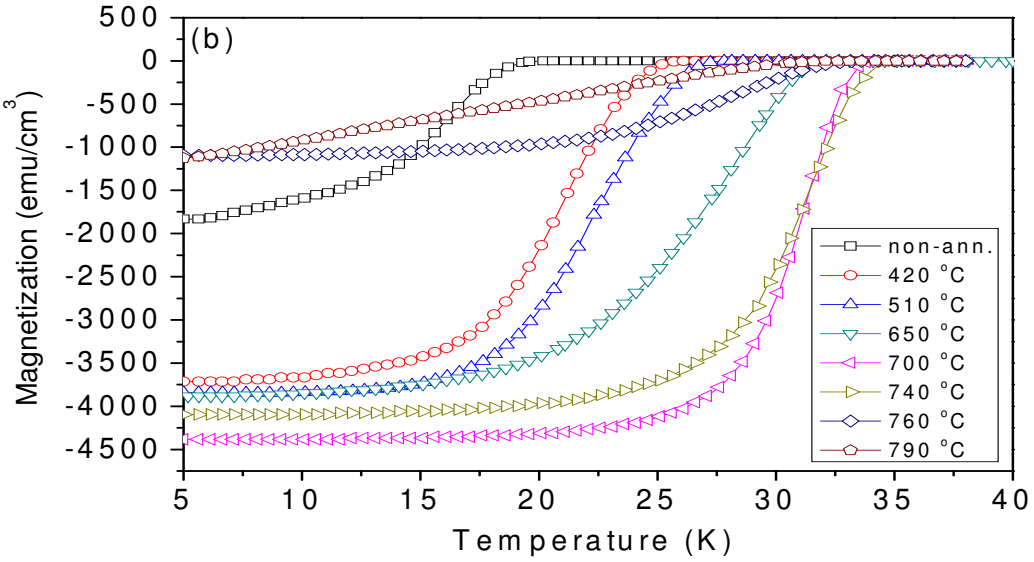

Fig. 5-3 (b) *Transition curves of magnetization against temperature for* T_{ann} *series.*

The results from Figure 5-3(a) once again confirm that the MgB_2 films with a short sintering time 5mins ≤ τ_{ann} ≤ 11mins have better superconductivity than the long τ_{ann} ones, as these samples induce a stronger diamagnetic moment. In Figure 5-3(b), it can be clearly seen that the strength of the diamagnetism of these samples in this series increases with T_{ann} until the T_{ann} exceeds 700˚C, after which it begins to drop.

Although it appears that a higher heating rate will help to enhance the superconductivity, and a high temperature annealing step is needed to form the superconducting phase, there is still a maximum heating rate, which, when exceeded, will result in severe evaporation of magnesium, leading to poor or even non-superconducting samples. In investigations on the influence of the heating rate on T_c of MgB_2 thin films in the previous literature [10], attempts were made to keep samples at T_{ann} of 640°C and 800°C for 10 minutes after rapid heating (110°C/min). However, the films were not superconducting. The change of T_c with T_{ann} observed in Figure 5-1 is consistent with the results obtained from this investigation.

When the T_{ann} was further increased to 760°C, a good $T_{c\ onset}$ at 32.6K was still obtained, but a broadened transition was observed. The broadening of ΔT may due to the higher rate of Mg loss at this temperature, which starts to lower the Mg-B ratio and affect the complete phase formation of pure MgB_2 within the sample. At an even higher T_{ann} of 790°C, both a significantly broadened ΔT and a suppressed T_c are observed. It is well known that a high temperature is necessary to trigger the reaction of magnesium with boron, as well as crystallization, but is difficult to maintain a sufficient amount of magnesium. The evaporation of magnesium also comes from the

decomposition of MgB_2 phase that has already been formed, if the temperature exceeds the decomposition temperature of MgB_2 for $T_{ann} > T_{dec}$. With the 12 minutes fixed ramp time, our samples have heating rates ranging from ~20-50°Cmin^{-1}, which is around the optimised heating rate reported [10]. In comparison with the samples that had undergone rapid heating at 110°C/min, in which the additional thick Mg cap layer made with a 7 mins deposition from the pure magnesium target was not enough to compensate for the loss of Mg before the formation of superconducting MgB_2. This may also explain why the samples obtained with rapid heating were not superconducting. A good balance needs to be achieved between the processes of MgB_2 phase formation, crystallization, and Mg evaporation, which will mostly take place during a high temperature sintering process. Based on the results described above, we considered that the optimal annealing conditions for our ~0.5μm MgB_2 film were now found to be $t_{heat\ up}$= 12 mins, τ_{ann} = 9 mins (for the highest T_c) at T_{ann} ~ 700°C, followed by free cooling down to room temperature at 20°C.

To determine the structure of the samples, x-ray θ-2θ scans for several samples sintered under different annealing conditions were performed and are shown in Figure 5-4. A characteristic XRD pattern of the bare Al_2O_3 sapphire *C*-cut substrate is also shown in the figure. For the good T_c samples, the diffraction patterns mainly show MgB_2 (001) and (002) peaks at 25.2° and 51.8° (2-theta), whereas in the others these peaks are not as strong and are accompanied by peaks resulting from other phases, such as MgB_4 and MgO. In some samples, the T_c is high, and we expected to observe strong detections at 25.2° and 51.8° (2-theta), both from the *c*-oriented MgB_2 phases. However, it is not yet clear why some samples with good T_c do not show strong detection at these angles. One reason might be that the sample sizes which we prepared for X-ray measurements are simply too small for the XRD system.

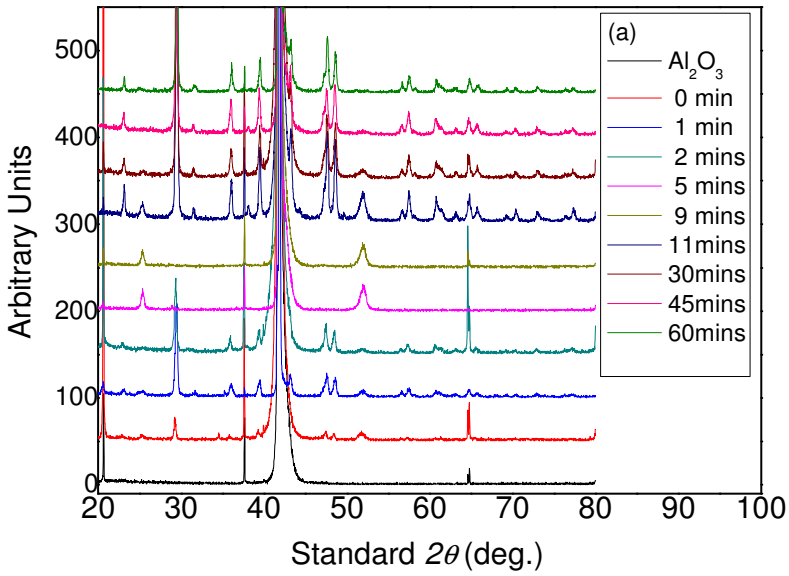

Fig. 5-4 (a) *X-ray diffraction spectra of the samples in the series sintered for different* τ_{ann} (Al_2O_3, 0 *min*, 1 *min*, 2 *mins*, 5 *mins*, 9 *mins*, 11 *mins*, 30 *mins*, 45 *mins* & 60 *mins*. *from bottom to top*).

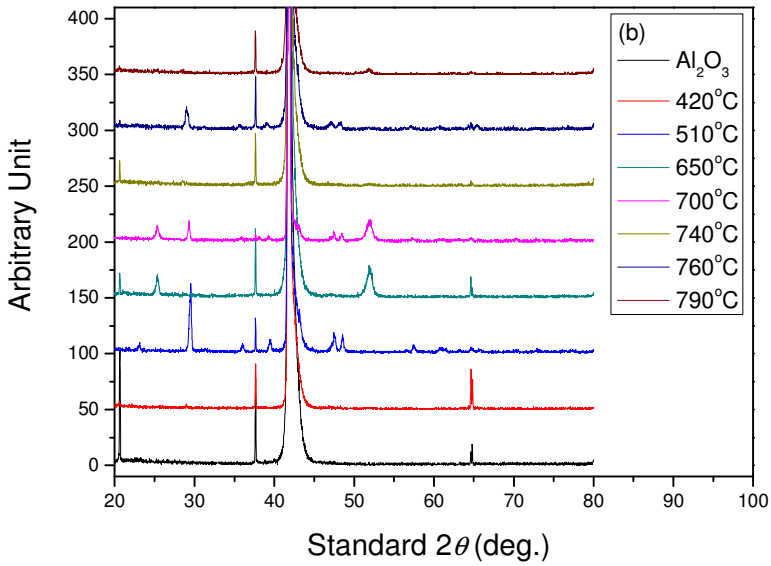

Fig. 5-4 (b) *X-ray diffraction spectra of the samples in the series sintered at different* T_{ann} (Al_2O_3, 420 °C, 510 °C, 650 °C, 700 °C, 740 °C, 760°C & 790°C. *from bottom to top*).

Magnetic measurements were made by the MPMS-5T and the critical current density J_c of our off-axis film #280806m was deduced from magnetization curves at temperatures from 5K to 25K and shown in figure 5-5. The change of magnetic J_c against the applied field B_a in the range from 0-5 T was calculated based on the Bean model, $J_c = 20\Delta M / [a(1 - a / 3b)]$, where ΔM (emu cm^{-3}) represents the magnetization differences $M_+ - M_-$, and a and b (cm) are the length dimensions of the rectangular shaped film, by assuming that the flux penetration all over this type of MgB_2 film is homogeneous. As revealed by magneto-optical imaging [10], the J_c estimated using this model has ignored the fact that the J_c at the outer parts near the edges of the sample might be higher than close to the centre, and the overall J_c value may be overestimated.

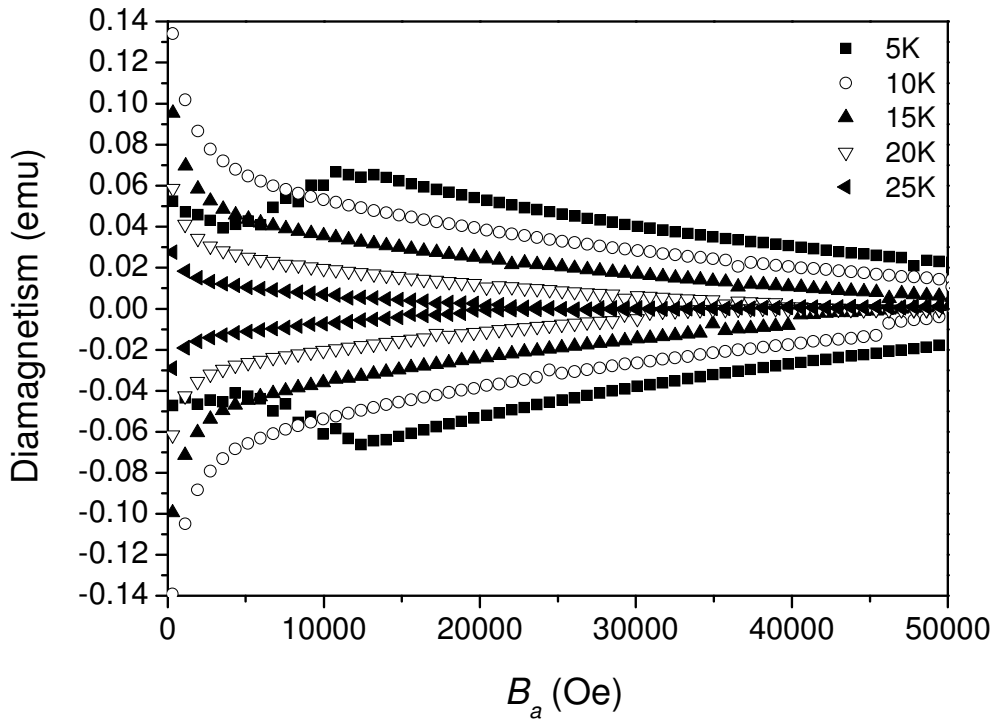

Fig. 5-5 M-H curves of the off-axis film at different temperatures.

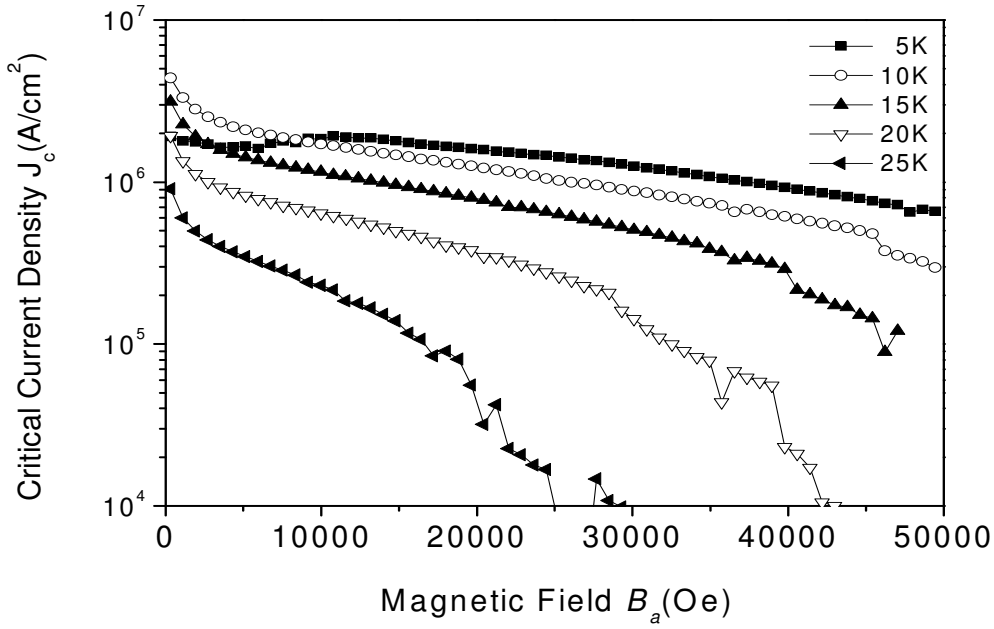

Fig. 5-6 Magnetic J_c versus applied field for the off-axis film (t_{ann}= 9 mins, T_{ann}= 700˚C) at different temperatures.

The calculated magnetic J_c values are presented in Figure 5-6 and show weak field dependence at low temperatures. The highest J_c value observed at 10K in near zero field was about 4.4×10^6 Acm^{-2}. J_c in near zero field at 5K is about 1.9×10^6 Acm^{-2}, whereas the J_c at 5K and 5T drops to about 6×10^5 Acm^{-2}. The strong J_c probably indicates the good interconnectivity between the grains formed inside the off-axis film, and the field dependence could suggest that strong flux pinning was provided by the higher level of disorder at the dense grain boundaries.

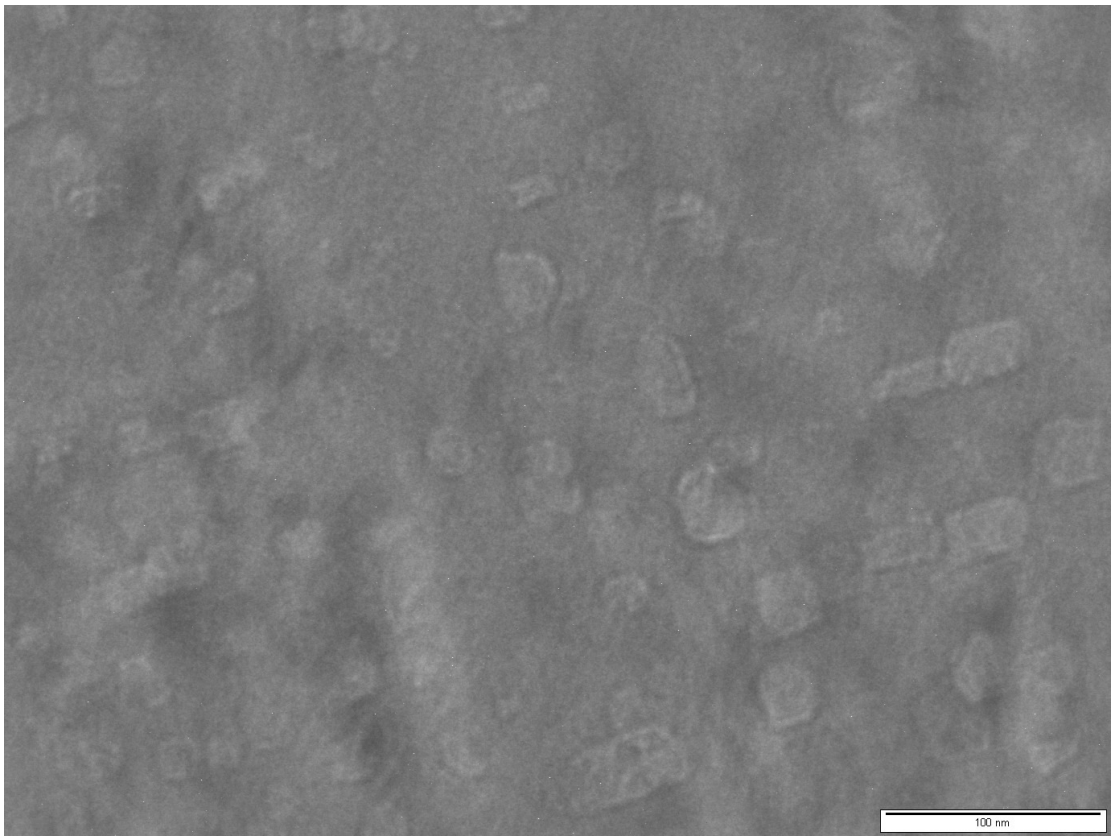

(a)

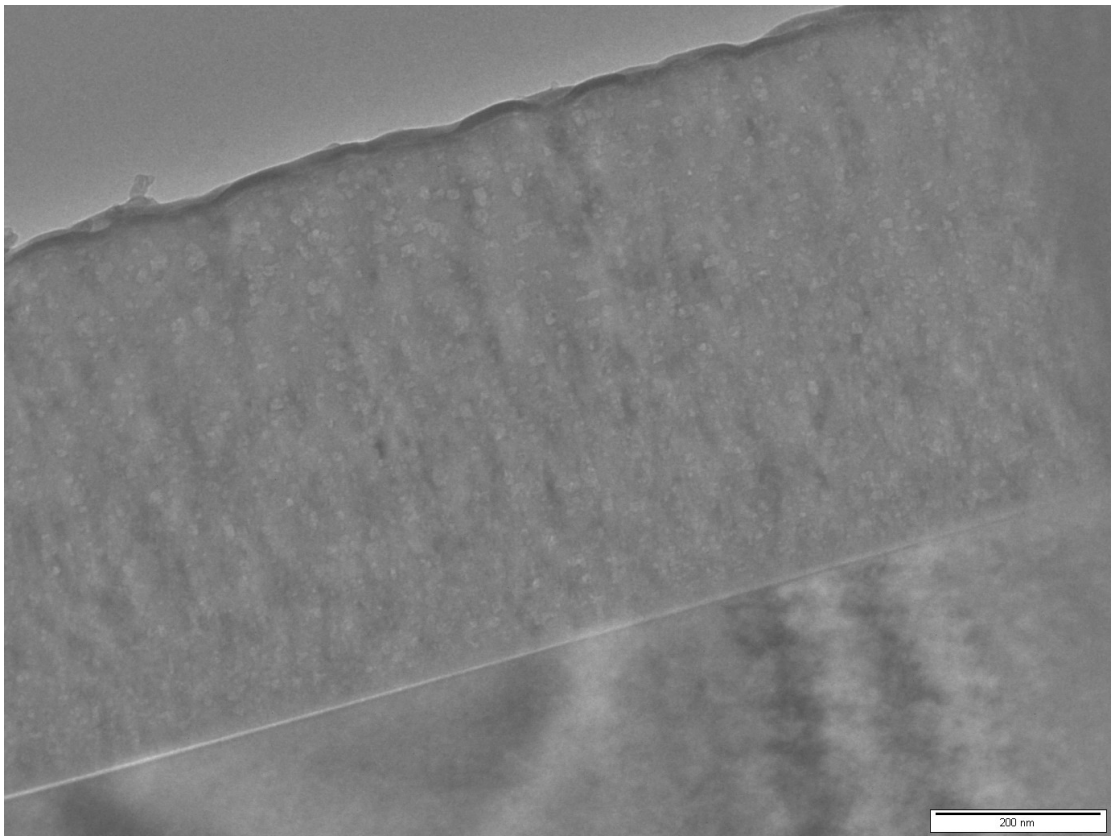

(b)

Fig. 5-7 TEM images of the #280806u sample: (*a*) *the surface, showing the average grain size of 20-30nm;* (*b*) *cross-sectional image showing that the average thickness of the single MgB_2 layer is about 630nm.*

The temperature dependence of the resistivity of the off-axis film #280806m was analysed using the *R-T* curves obtained using the transport method described in Chapter 3. The $T_{c\ \text{onset}}$ of the film is 34.8K, and the zero field resistivity T_c is 34.2 K. These are among the highest reported values for *in situ* PLD produced films so far. However, the T_c observed is lower than the bulk value. This could be attributed to the enhanced scattering induced by lattice distortion and the intra-grain disorder. The residual resistivity just above T_c is about 50 μΩ, and the reason why it is higher than that of MgB_2 single crystals may also be due to higher level of disorder. The resistivity difference $\Delta\rho_{300\text{-}40K}$ of the off-axis films of 13-14 μΩ cm is comparatively low among MgB_2 films. This shows that the effective current carrying area is high and could be due to the dense and well connected MgB_2 grains inside the film. The resistivity in the off-axis film is lower than the on-axis value [9], which confirms that the off-axis films generally have a lower level of disorder than the on-axis films.

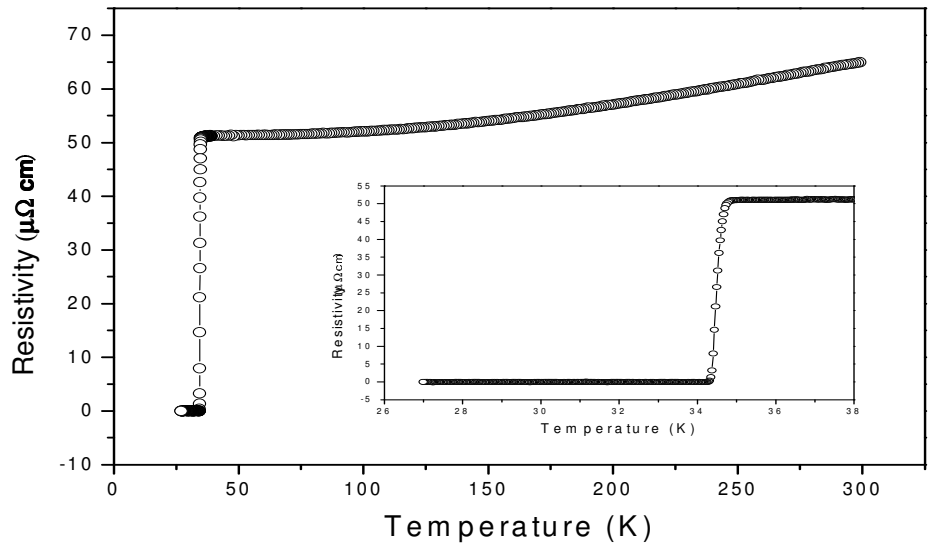

Fig. 5-8 The temperature (K) dependence of the resistivity ρ in #280806m. The inset figure is an enlargement of the transition near T_c.

In the transport measurement, a transport current of about $10Acm^{-2}$ density was induced to flow in a transverse magnetic field, which was applied in both in-plane and out-of-plane perpendicular directions in two different measurements. As the current exerts a force on the vortices, flux motion occurs, and the vortices move from one side of the film to the other. The flux flow produces an electric field perpendicular to the magnetic field, and the flux motion gives rise to loss in the transport current and heat dissipation. In both measurements, the R-T transition curve remains quite sharp and shows no significant transition broadening until 8.7 T, since the regime of flux-flow resistivity is displayed by the resistivity transition width which may indicate that the flux pinning in our *in situ* MgB_2 film remains strong in both field directions.

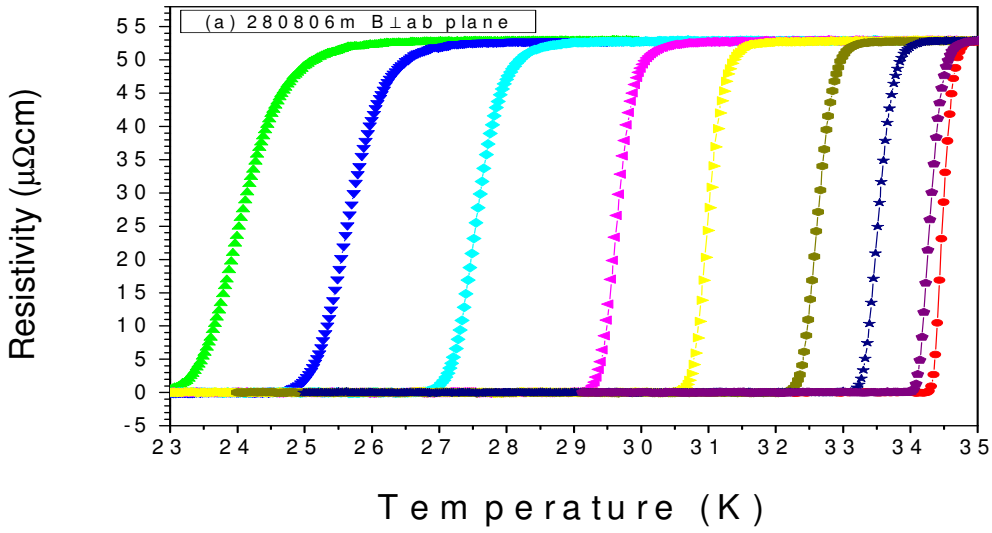

Fig. 5-9(a) *The field dependence of the R-T curves of the MgB_2 film #280806m in* 8.7T, 7T, 5T, 3T, 2T, 1T, 0.5T, 0.1T *and* 0T *from left to right in perpendicular fields.*

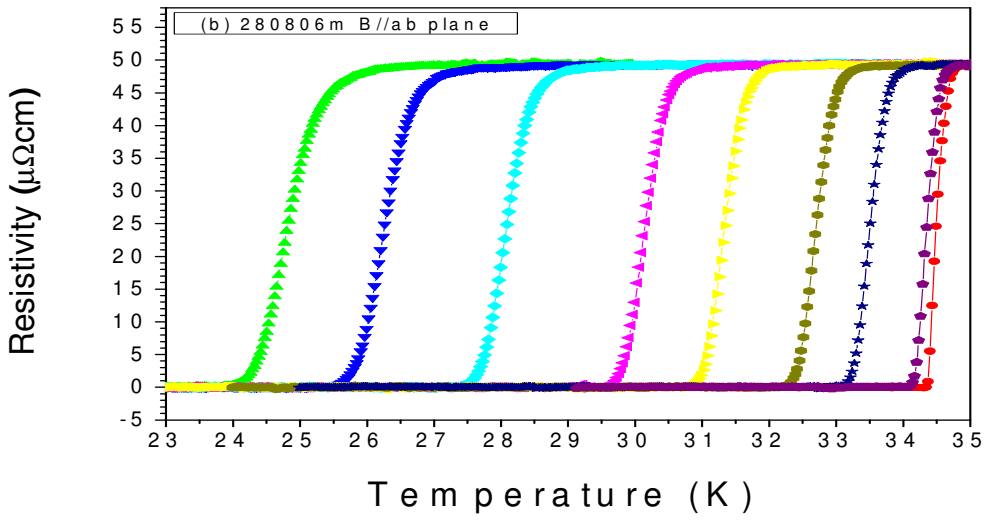

Fig. 5-9(b) *The field dependence of the R-T curves of the MgB_2 film #280806m in* 8.7T, 7T, 5T, 3T, 2T, 1T, 0.5T, 0.1T *and* 0T *from left to right in parallel fields.*

The H_{c2} and H_{irr} curves were derived from the associated transport curves in Figure 5-10, using 90% and 10% of the normal state ρ values for both field directions. In both cases, high *H-T* slopes were revealed. The value of dH_{c2}/dT near T_c is about 0.63ΔT/K for $\mathbf{H} \perp ab$-plane and 0.5ΔT/K for $\mathbf{H} \parallel ab$-plane, but the temperature dependence of the upper critical field is very similar in both B_a directions.

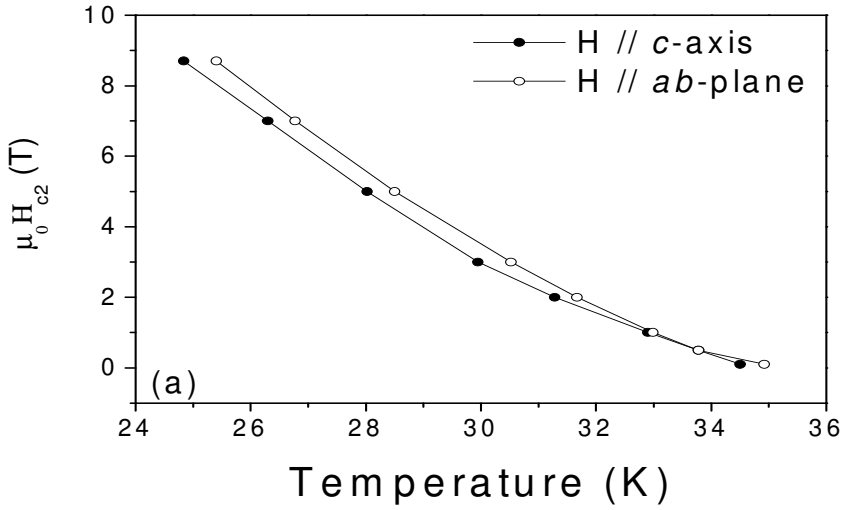

Fig. 5-10 (a) *H_{c2}–T curves derived from T at 90% of the normal state resistivity.*

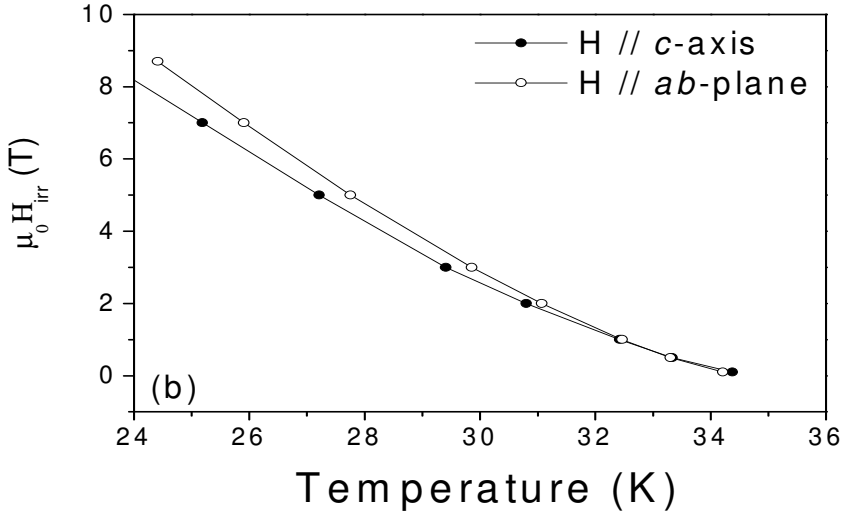

Fig. 5-10 (b) *H_{irr}–T curves derived from T at 10% of the normal state resistivity.*

Normally, high H_{c2} anisotropy is expected in *c*-oriented MgB_2 thin films. The fact that anisotropy is suppressed for both H_{c2} and H_{irr} might indicate the presence of defects in our films, which may have also increased H_{c2} values due to stronger scattering. In addition, the density of grain boundaries could also have contributed to the suppression of the $H_{c2}^{//}/ H_{c2}^{\perp}$ ratio of our film. As T increases, the ratio $H_{c2}^{//}/ H_{c2}^{\perp}$ decreases up to T_c. This behaviour is similar to the usual temperature dependence of $H_{c2}(T)$ in MgB_2 single crystals at low temperatures.

For "dirty" (high level of lattice defects and electron scattering) MgB_2 samples, the H_{c2} anisotropy is small, and the experimental H_{c2}-T curves are approximately linear [12, 13]. Based on this, we roughly extrapolated that the value $H_{c2}(0) \approx 34.5$ T for both field directions at 0 K, using a linear equation, $H_{c2}(0)=H'_{c2}T_c$, where $H'_{c2} = |dH_{c2}/dT|$ near T_c. An estimation of the electron mean-free path l, using the equations for superconductors in GL theory, $H_{c2}(T) = \Phi_0/(2\pi\xi^2)$ and $\xi(T) = 0.855(\xi_0 l)^{1/2}/[1-T/T_c]^{1/2}$ (in the dirty limit), where Φ_0 is the flux quantum unit of a vortex and ξ_0 is taken as the coherence length of a single crystal (~6.0 nm) [14], gives $\xi \approx 2.9$ nm and $l \approx 2.2$ nm at zero temperature.

Conclusions

The off-axis films can endure higher temperature and longer annealing than the on-axis films prepared previously in our group. The most suitable annealing temperature appears to be about 700 °C, and the annealing time from 5 to 9 min judging from the magnetic transition temperature. The zero resistance T_c of 34.5 K is the highest among *in-situ* PLD films reported so far. The precursor film deposited at 250 °C from a stoichiometric MgB_2 target shows noticeable MgB_2 (001) and (002) peaks in XRD, which indicates that MgB_2 phase formation and *c*-axis orientation on the Al_2O_3-C substrate are favoured by off-axis deposition at temperatures as low as 250 °C. In addition, an unconfirmed calcite type impurity phase appears in both under-annealed and over-annealed films.

Reference

[1] Nagamatsu J, Nakagawa N, Muranaka T, Zenitani Y, and A. J, *Nature,* vol. 410, p. 63, 2001.

[2] K. Ueda and M. Naito, "As-grown superconducting MgB_2 thin films prepared by molecular-beam epitaxy " *APPLIED PHYSICS LETTERS,* vol. 79, pp. 2046-2048, 2001.

[3] X. H. Zeng, A. V. Pogrebnyakov, A. Kotcharov, X. X. Xi, and E. M. Lysczek, "*In situ* epitaxial MgB_2 thin films for superconducting electronics," *Nature Materials,* vol. 1, pp. 35-38, 2002.

[4] C Ferdeghini, V Ferrando, G Grassano, W Ramadan, E Bellingeri, V Braccini, D Marr´e, P Manfrinetti, A Palenzona, F Borgatti, R. Felici, and T.-L. Lee, "Growth of c-oriented MgB_2 thin films by pulsed laser deposition: structural characterization and electronic anisotropy," *Supercond. Sci. Technol. ,* vol. 14, pp. 952–957, 2001.

[5] C. Ferdeghini *, V. Ferrando, G. Grassano, W. Ramadan, E. Bellingeri, V. Braccini, D. Marre, M. Putti, P. Manfrinetti, A. Palenzona, F. Borgatti, R. Felici, and C. Aruta, "Anisotropy in c-oriented MgB_2 thin films grown by pulsed laser deposition," *Physica C* vol. 378–381, pp. 56–60, 2002).

[6] C. Ferdeghini *, V. Ferrando, G. Grassano, W. Ramadan, V. Braccini, M. Putti, P. Manfrinetti, and A. P. b, "Transport properties of c-oriented MgB_2 thin films grown by pulsed laser deposition," *Physica C* vol. 372–376, pp. 1270–1273, 2002.

[7] Dragana Mijatovic *, Alexander Brinkman, Guus Rijnders, Hans Hilgenkamp, Horst Rogalla, and D. H. A. Blank, "Superconducting thin films of MgB_2 by pulsed-laser deposition," *Physica C,* vol. 372–376, pp. 1258–1261, 2002.

[8] H.M. Christen, H.Y. Zhai, C. Cantoni, M. Paranthaman, B.C. Sales, C. Rouleau, D.P. Norton, D.K. Christen, and D. H. Lowndes, "Superconducting magnesium diboride films with $T_c \approx 24$ K grown by pulsed laser deposition with in situ anneal," *Physica C,* vol. 353, pp. 157-160, 2001.

[9] Yue Zhao, Mihail Ionescu, J. Horvat, and S. X. Dou, "Off-axis MgB_2 films using an *in situ* annealing pulsed laser deposition method," *Supercond. Sci. Technol.,* vol. 18, pp. 395–399, 2005.

[10] Yue Zhao, Mihail Ionescu, Alexey V Pan, Shi Xue Dou, and E. WCollings, "*In situ* annealing of superconducting MgB_2 films prepared by pulsed laser deposition," *Supercond. Sci. Technol. ,* vol. 16 pp. 1487–1492, 2003.

[11] Yue Zhao, Mihail Ionescu, Josip Horvat, and S. X. Dou, "Comparative study of in situ and ex situ MgB_2 films prepared by pulsed laser deposition," *Supercond. Sci. Technol. ,* vol. 17, pp. S482–S485, 2004.

[12] S. L. Bud'ko, C. Petrovic, G. Lapertot, C. E. Cunningham, P. C. Canfield, M.-H. Jung, and A. H. Lacerda, *Phys. Rev. B,* vol. 63, p. 220503(R), 2001.

[13] A. Gurevich, S. Patnaik, V. Braccini, K. H. Kim, C. Mielke, X. Song, L. D. Cooley, S. D. Bu, D. M. Kim, J. H. Choi, L. J. Belenky, J. Giencke, M. K. Lee, W. Tian, X. Q. Pan, A. Siri, E. E. Hellstrom, C. B. Eom, and D. C.

Larbalestier, "Very high upper critical fields in MgB2 produced by selective tuning of impurity scattering," *Supercond. Sci. Technol.,* vol. 17, p. 278, 2004.

[14] Y. Eltsev, S. Lee, K. Nakao, N. Chikumoto, S. Tajima, N. Koshizuka, and M. Murakami, *Phys. Rev. B,* vol. 65, p. R140501, 2002.

Chapter 6

Investigation of influence on superconducting properties by selective Si addition

In this chapter we report on the influence of silicon addition on the superconducting properties of MgB_2 thin films made by pulsed laser deposition followed by in situ annealing using the optimized conditions in previous chapter. In order to increase the performance and sustain the superconductivity of MgB_2 at higher magnetic field, many efforts have been made to enhance the pinning force of this material in its superconducting state. This is a crucial issue for this newly discovered superconductor. Pure MgB_2 has a clear disadvantage as compared to existing high field superconductors, owing to its low upper critical fields in both the parallel $H_{c2}^{\parallel}$ and the perpendicular $H_{c2}^{\perp}$ directions. The high temperature superconductors (HTS) in present use have upper critical fields H_{c2} well beyond 50 T, but these HTS conductors suffer from intrinsic current blockage across grain boundaries and high H_{c2} anisotropy. In practice, the weak linked nature of practical HTS-conductors is overcome by crystallographic texture, but conductors also have to be made in tape form to compensate for the high H_{c2} anisotropy before they can be applied in high magnetic field. Other superconductors based on niobium mixtures can be easily fabricated into wires, which are capable of generating high magnetic fields of a few tens of Tesla, but they are confined to work at only very low temperatures of a few Kelvin.

To this end, additions by doping various elements or compounds into different forms of MgB_2 have been adapted to increase its H_{c2} [1-7], and this provides a domain for

MgB_2 to be well suited for high-field magnet applications at around 30K, where other types of superconductors will be unable to challenge it.

Introduction

Researchers in our group at the University of Wollongong have been using Si, which is a substance that is highly reactive with Mg, forming Mg_2Si during a high temperature sintering process of around 600˚C [6-8]. Based on the previous literature, Si does not seem to cause significant intra-grain scattering directly, but changes in the intra-grain scattering properties due to refinements in MgB_2 grain boundaries in regions of high Si density have been considered. MgB_2 films have generally higher J_c than that of bulk material. Since our *in-situ* annealed off-axis films which had been sintered for considerably shorter times have small, but well-linked grains, the density of grain boundaries is quite high, and this may have increased the flux pinning. It is interesting to see whether by adding controlled amounts of Si into *in-situ* annealed MgB_2 films can further increases the pinning force.

In this chapter, we mainly concentrate on the improvement of superconducting performance at low temperature and discuss several important features, including whether adding a small amount of Si can lead to a combined effect to enhance the pinning force, while not significantly depressing the T_c under the optimized annealing condition for off-axis deposited MgB_2 films.

Experiment

The preparation work for off-axis MgB_2 thin film deposition with Si addition is similar to that described in previous chapter. The 250 mJ/pulse KrF laser beam (λ=248 nm) trimmed from the 500 mJ/pulse original beam was focused to a 7×1.5 mm^2 spot on the target. The substrate surface was aligned parallel to the axis of the plume during the deposition [9]. The average distance between the target and the substrate is about 25 mm and the replication frequency of the pulses was set to be 10 Hz. During the deposition, the substrate was kept at 250˚C, and the chamber was filled with argon gas up to 120mTorr.

In this work, three targets were used: an MgB_2 target (84% density), a pure Mg target, and a Si single crystal target. These targets were mounted onto a carousel, and the addition of Si during the deposition of the film was conducted by a target switching method. Si was added into the sample by sequentially ablating the MgB_2 and Si targets. For each of our samples, the Si target was ablated for a different time, leading to different addition levels. An additional Mg cap layer ~ 800nm thick was also deposited on the film surface for each sample to compensate Mg loss, since these Si-added samples were also destined to undergo a high temperature sintering process during which MgSi and MgB_2 phases were formed.

When deposition finished, the vacuum was filled with argon gas up to a pressure of 760 Torr in 3 min 40 sec. The reason for this is to provide a high vapour pressure, so as not to evaporate too much Mg from the film surface during annealing. The samples were all heated from 250 °C up to 700 °C in 12 mins and maintained at that temperature for 9 mins, according to our previous work described in Chapter 5. Then

the power was switched off automatically, and the samples were freely cooled down to room temperature at a rate of ~ 55 °C min^{-1}.

The average thickness of the *in-situ* annealed films is approximately 400 nm, according to cross-section image observation by TEM. The different Si contents added into the films were nominally determined by the Si deposition time, using the calibration from the Si growth rate of ~0.2nm s^{-1} at 10Hz on a bare substrate, and were checked using EDS.

To investigate whether improvements were made by this Si-addition deposition followed by *in-situ* annealing, T_c of the films was obtained by DC magnetization measurements on a SQUID magnetometer system (MPMS, Quantum Design). The samples were mounted on a straw and placed inside the magnetometer with the applied magnetic field of 25 Oe perpendicular to the sample surface. The magnetic transition was measured by ZFC routine. The *R-T* transport measurement was carried out using the standard four-probe method, on a PPMS-9T (Quantum Design) system. Magnetic field was applied in both parallel and perpendicular directions to the film surface. Both the H_{c2}-*T* and H_{irr} -*T* curves were plotted from points selected at 90% and 10% of the normal resistivity at T_c onset, respectively.

We tested the differences in superconducting properties between samples with different Si content which is calculated by assuming that only the two MgB_2 and MgSi phases were present. Due to the existence of other phases, such as oxides, Mg deficiency, or excess Mg in the films, the discrepancy between the nominal and the

detected value could be large. However, in this thesis, we only refer to the detected Si contents.

Results and discussion

We calculated the Si content in the MgB_2 films by Energy Dispersive Spectroscopy (EDS) shown in figure 6-1, by assuming that only MgB_2, Mg_2Si phases, and oxygen impurities were present in the *in situ* annealed films. Due to the existence of oxygen and other impurities as expected, the discrepancy in the nominal and observed Si contents from EDS was large. XRD spectra (Fig. 6-2) show that a film with higher Si content induces higher intensity from the impurity peaks. However, no obvious Mg_2Si phase was detected, perhaps due to that the signal from the small proportion of highly dispersed Mg_2Si in the MgB_2 films is difficult to be pickup by XRD. The nominal and detected Si contents, and the magnetic T_c and J_c are listed in Table 6-1.

Sample #	280806m	140906m	150906m
Nominal Si content (wt %)	0	5	23.5
Detected Si content (wt %)	_	5.7	15.8
Magnetic $T_{c\ \text{onset}}$ (K)	34.2	29.6	28.1

Table 6-1 Si content and corresponding measured magnetic properties in the MgB_2 films.

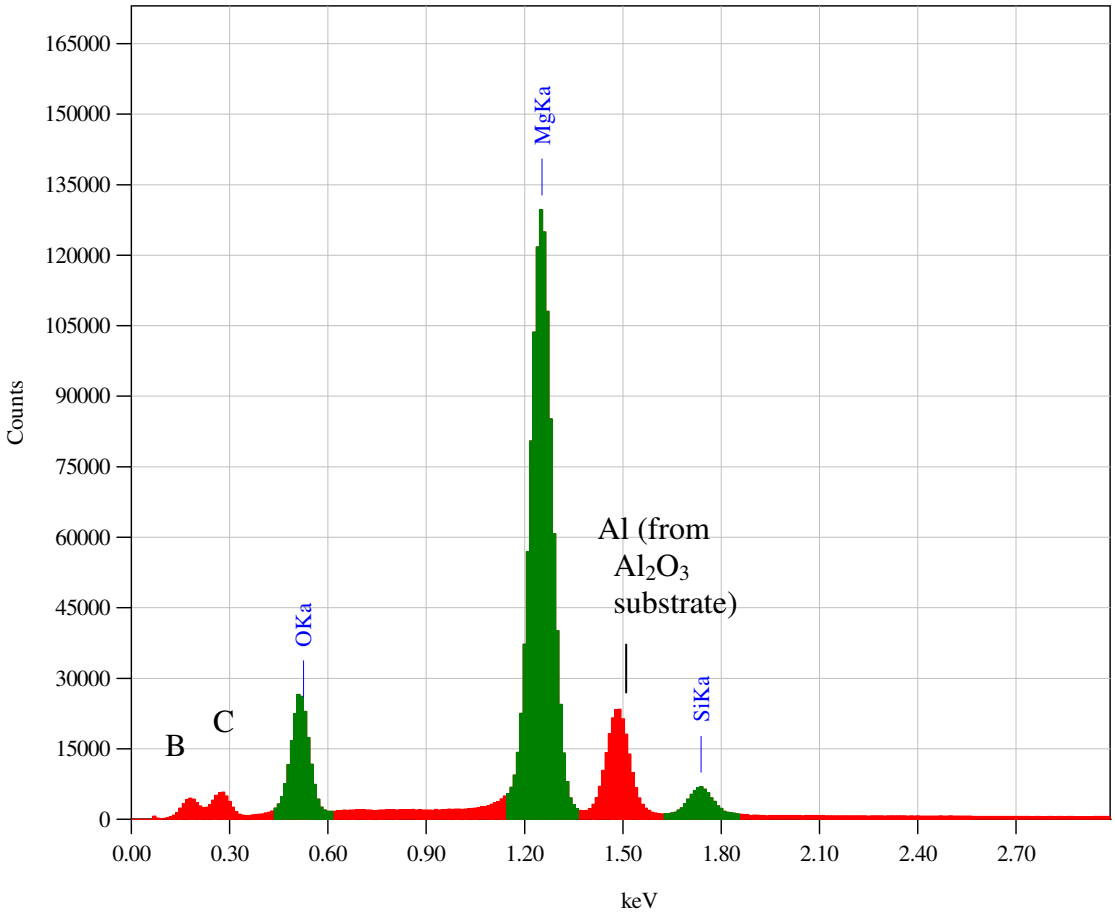

Fig. 6-1(a) *EDS spectrum of 5.7% detected Si content in sample #140906m.*

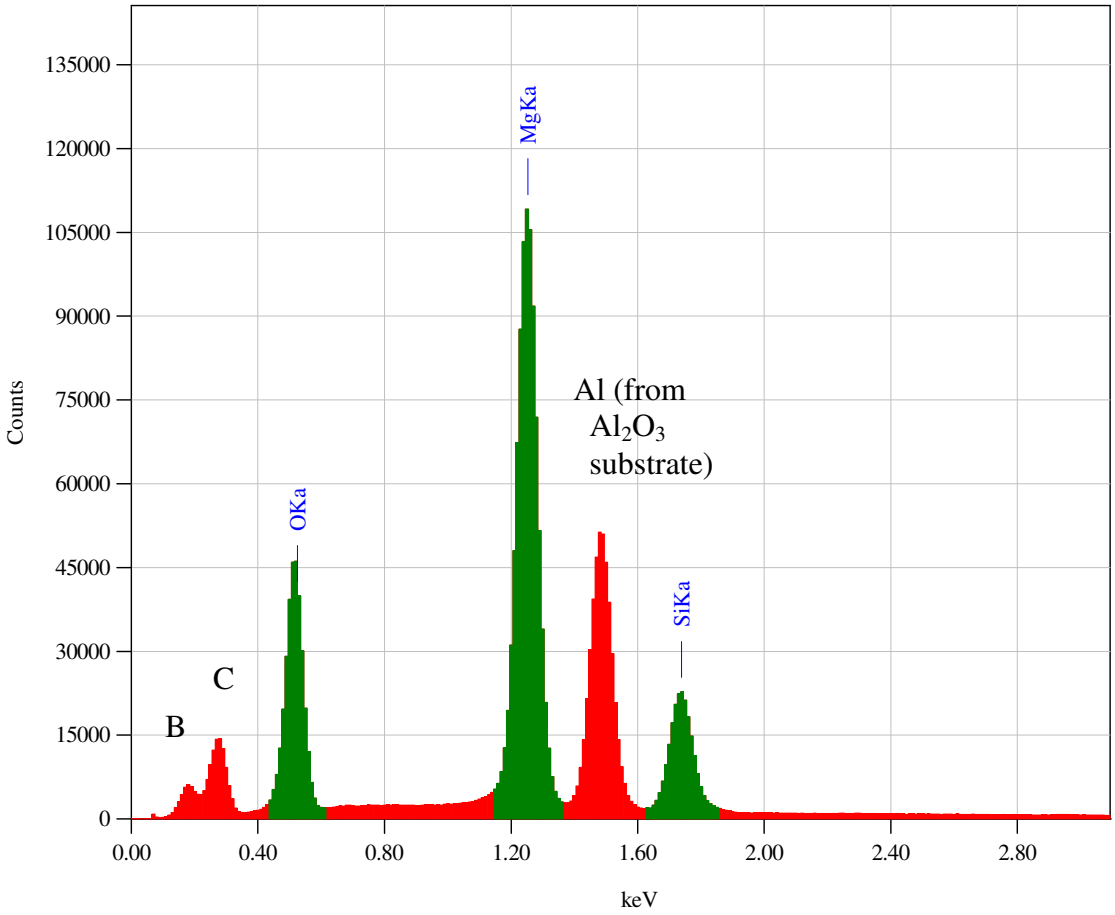

Fig. 6-1(b) *EDS spectrum of 15.8% detected Si content in sample #150906m.*

The Si deposited on each layer is approximately the equivalent of a 2.5 nm layer for 5s deposition. Figure 6-3 shows the surfaces and mappings of the Si distribution by EDS in our Si-added MgB_2 films. The Si distribution appears to be quite homogeneous with respect to the droplets in both the 5.7% and 15.8% films. Based on this observation, we assume that the Si content is spatially homogeneous and that a substantial reaction between Si and Mg might have taken place in each dual layer inside the films.

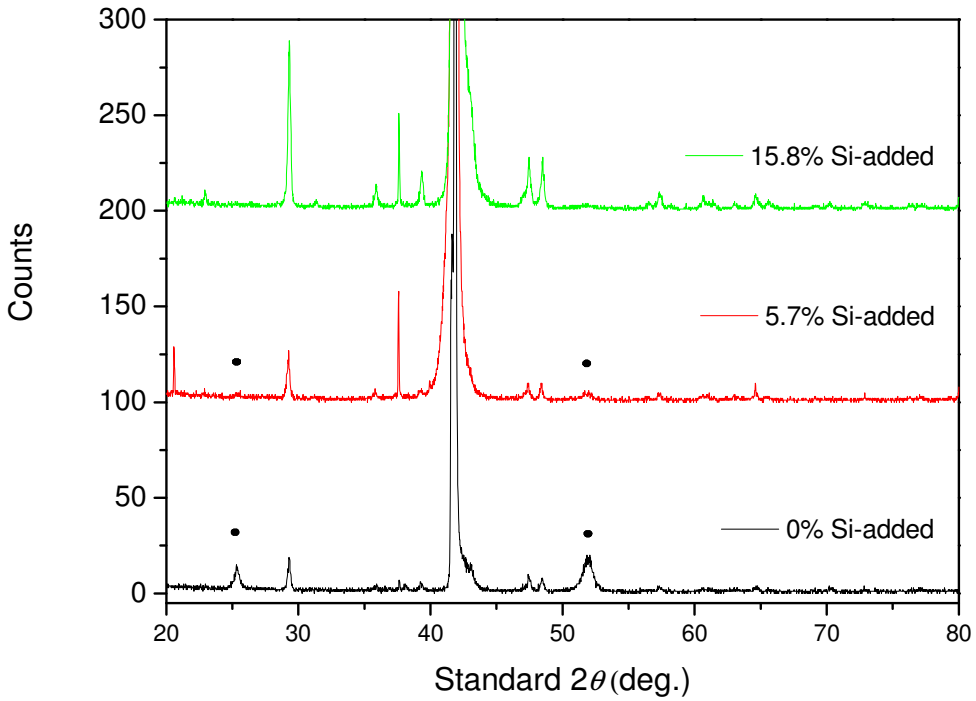

Fig. 6-2 XRD spectra show an increased level of impurities with higher Si addition. The detection of the MgB_2 (001) and (002) peaks at 25.2° and 51.9° are indicated by the dots. The 5.7% Si added sample still shows small detection at these two angles, whereas in the 15.8% Si added sample no detection of these peaks was observed at all.

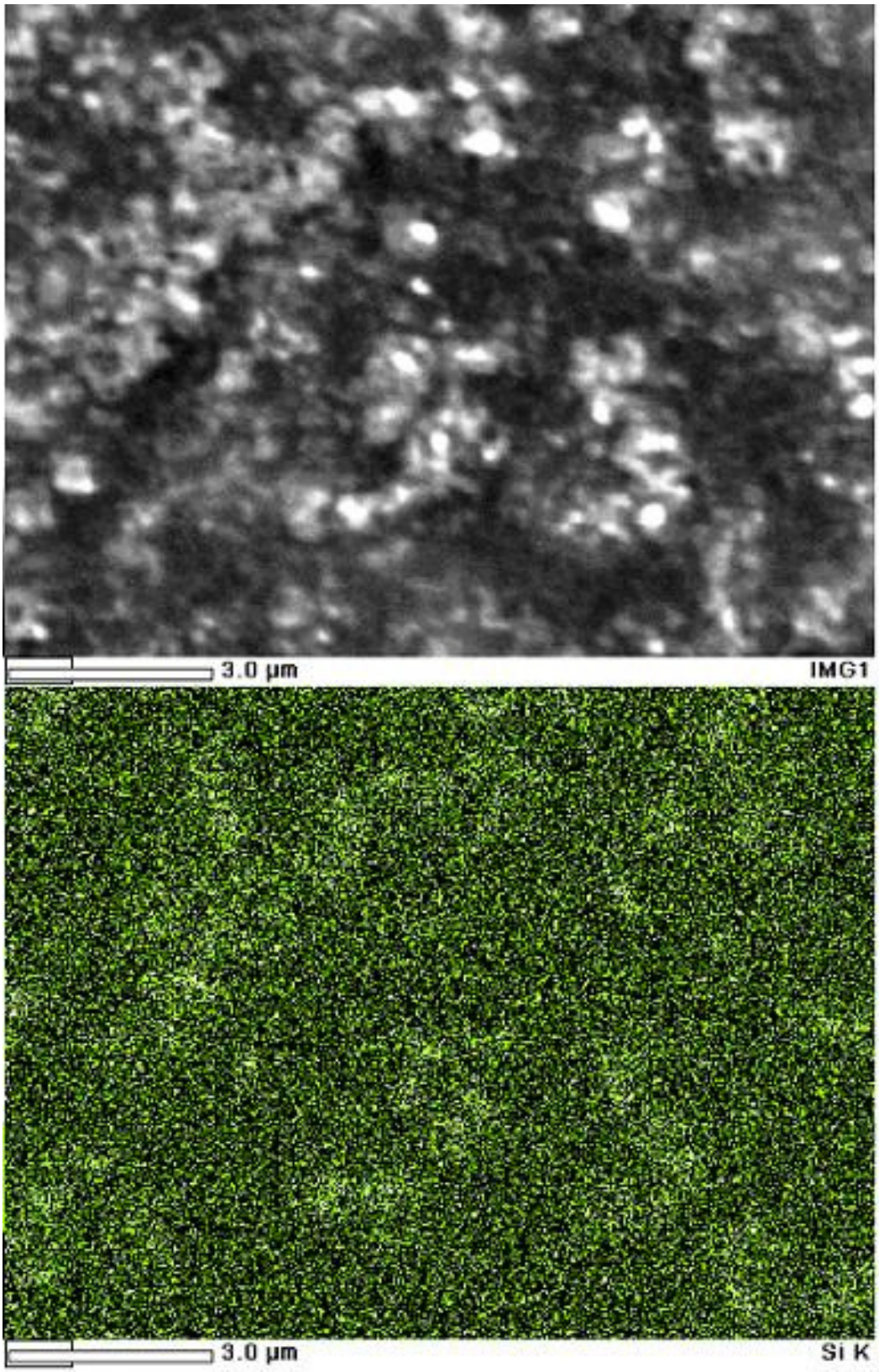

Fig. 6-3(a) *EDS surface image* (*top*) *and Si mapping* (*bottom*) *of the 5.7% Si added* MgB_2 *film.*

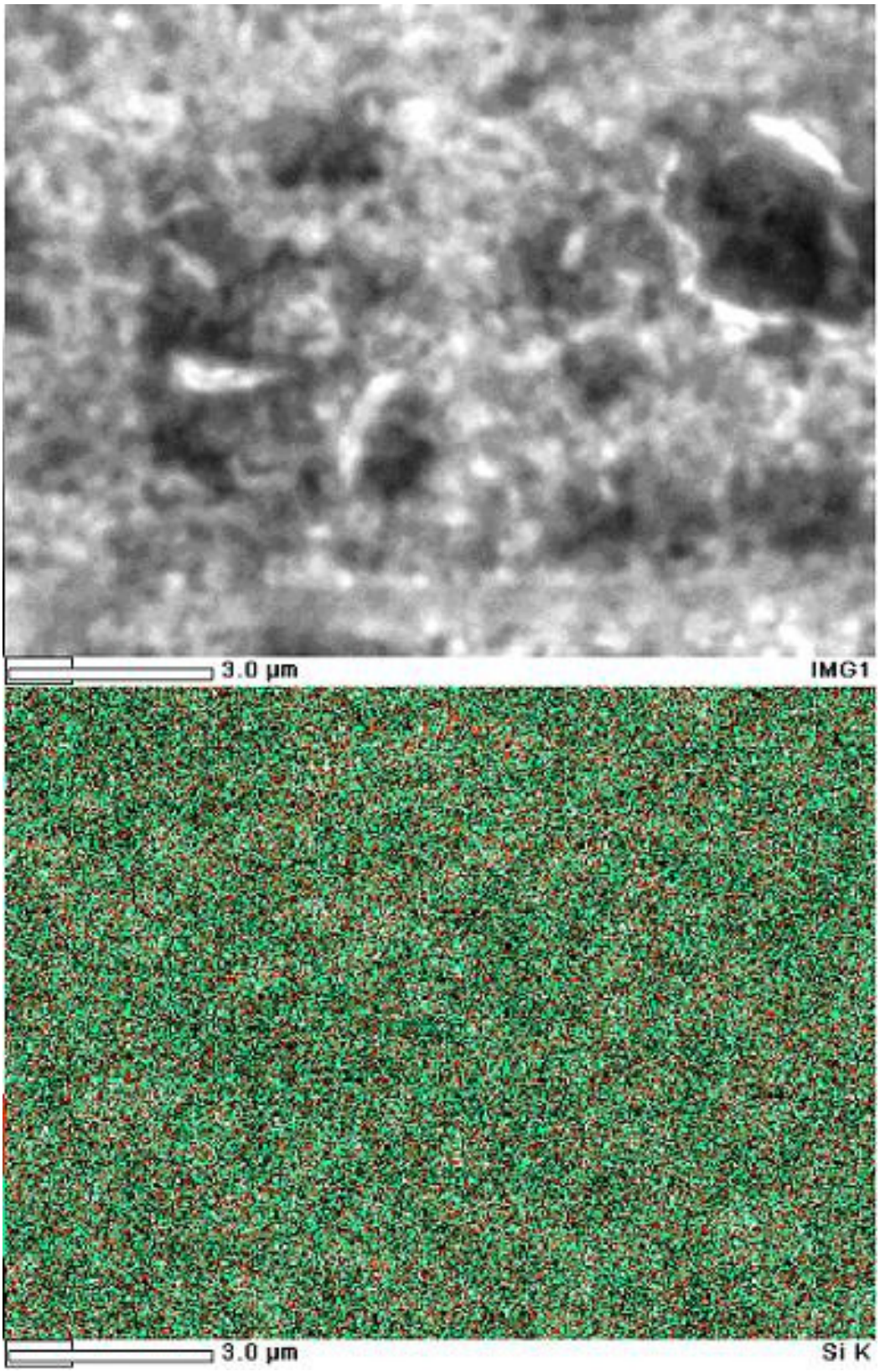

Fig. 6-3(b) *EDS surface image* (*top*) *and Si mapping* (*bottom*) *of the 15.8% Si added* MgB_2 *film.*

The ZFC magnetization curves for the Si-added and MgB_2 films are shown in figure 6-4. Both the 5.7% and 15.8% Si added MgB_2 films have suppressed T_cs of about 29.6K and 28.1K respectively. This could be because contamination induced a higher level of disorder in the films. From figure 6-4 we also found that a further increase in Si level results in a slight broadening of the transition width. A TEM cross-sectional image of the 15.8% Si-added MgB_2 film taken at 40k times magnification shows that the majority of the film had formed grains between 40-60nm in size, which are slightly larger than the grains observed in the pure MgB_2 film in chapter 5. This seems to agree with the fact that Si is conducive to MgB_2 phase formation under suitable annealing conditions [10]. On the other hand, an apparently layered part is also seen in the film adjacent to the substrate, indicating the re-crystalizaton is somehow blocked near the substrate. It is interesting to that the microstrure in different depth of the film is so different. The difference in the inner stain along the depth might be a possible reason. Further investigations in future works are needed to clarify the mechanism behind it.

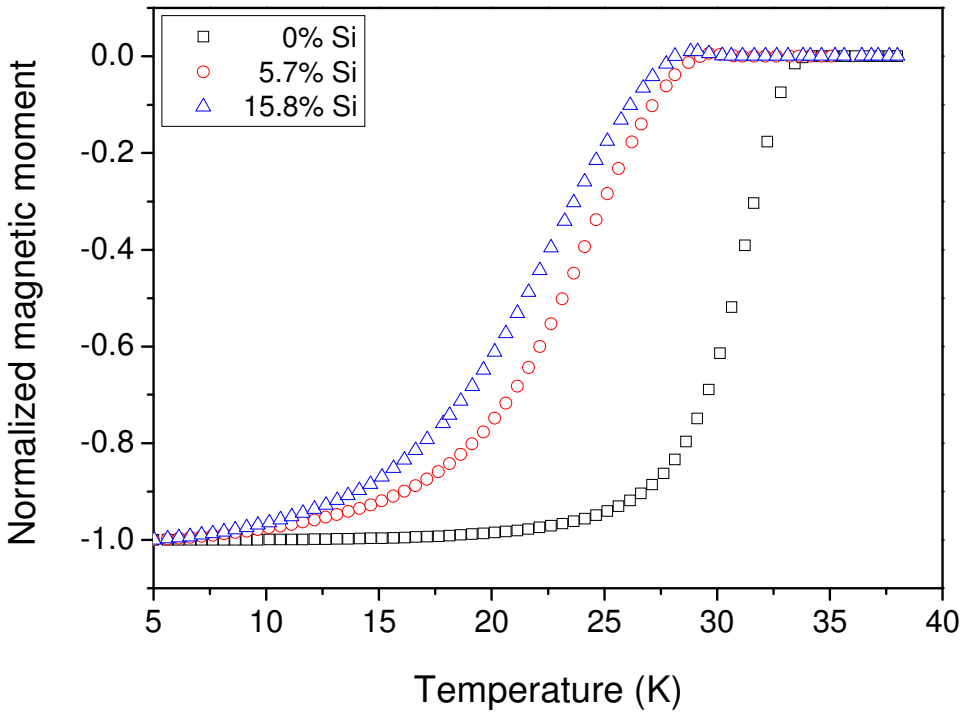

Fig. 6-4 DC magnetization curves of films with different level of Si addition in ZFC measurements.

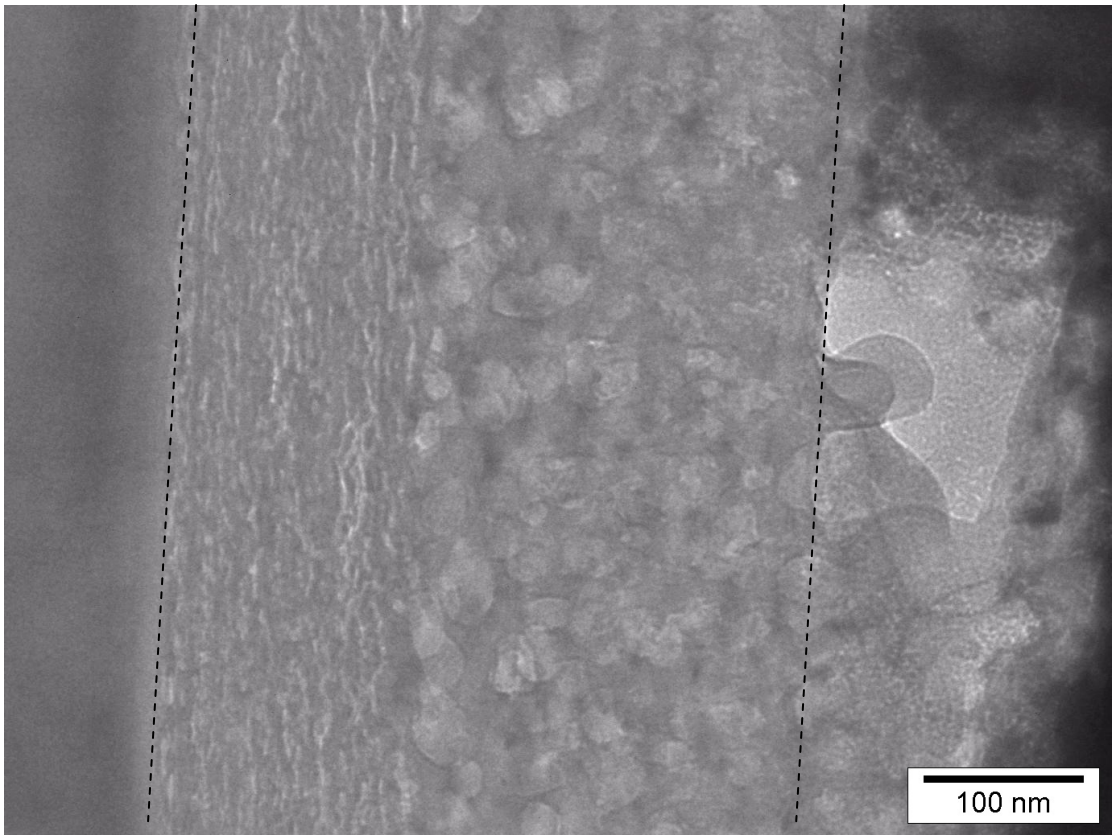

Fig. 6-5 TEM cross-sectional image showing grain structures inside the 15.8% Si added MgB_2 film. The middle part is the MgB_2 film and the Al_2O_3 substrate is at the left-hand side.

The change in J_c with different Si additions at 5K is shown in Figure 6-6. From this observation, we did not obtain higher critical current density in the Si added MgB_2 films. At a field of 0.3-0.5T, the J_c values for the 5.7% Si-added film is slightly lower than for the 0% Si film, probably due to the reduction in effective current carrying area by the Si addition. However, the J_c of the 5.7% Si-added film appears to remain slightly more constant in an applied field than that of the 0% Si film, while the J_c value of the 15.7% Si added film is significantly suppressed. This is especially clear when the applied field strength is low < 2T. The difference in the current density J_c values between 1T and 5T for the 5.7% Si added and 0% Si films are 7.4×10^5 and

1.3×10^6 A/cm^2, respectively. However, the difference observed is small, and improvement in J_c by selective Si addition is usually only obvious at very low temperature. Further investigations on the upper-critical field and pinning properties were carried out using a four probe transport current method, as shown in Figures 6-7 & 6-8.

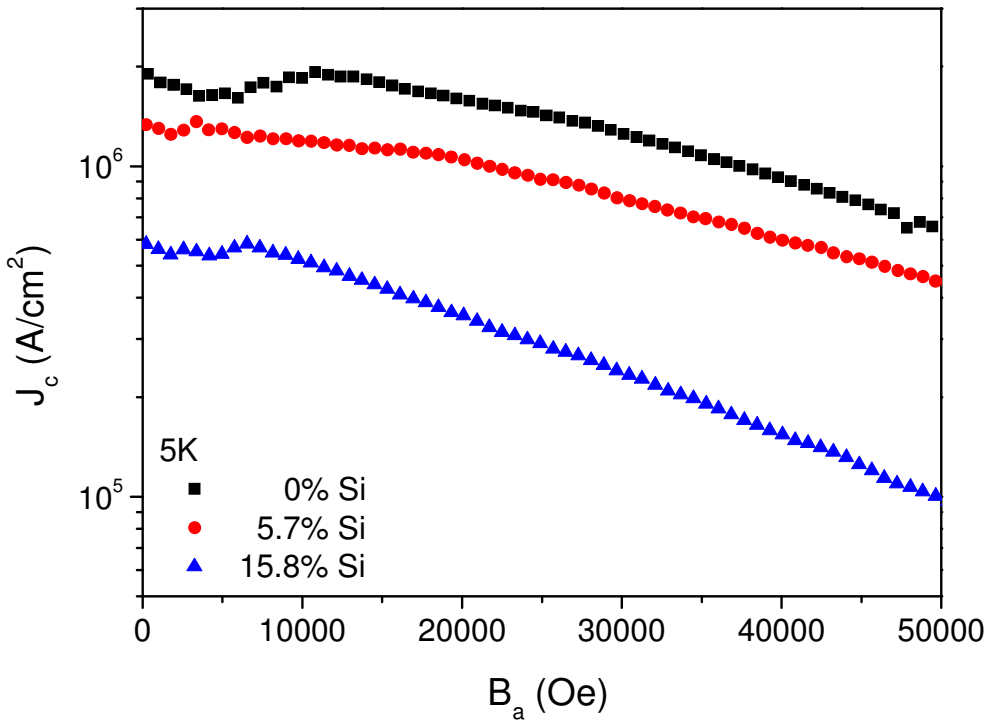

Fig. 6-6 Change of J_c of different levels of Si added films against applied magnetic field at 5K.

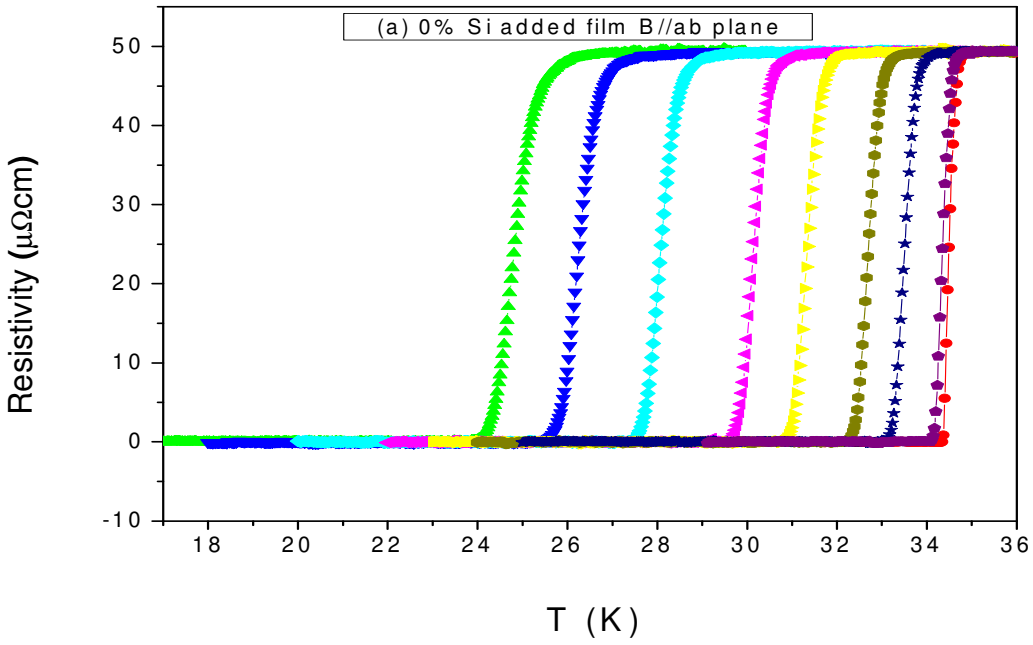
(a) 0% Si added film B//ab plane
Resistivity (μΩcm)
T (K)
50
40
30
20
10
0
-10
18
20
22
24
26
28
30
32
34
36

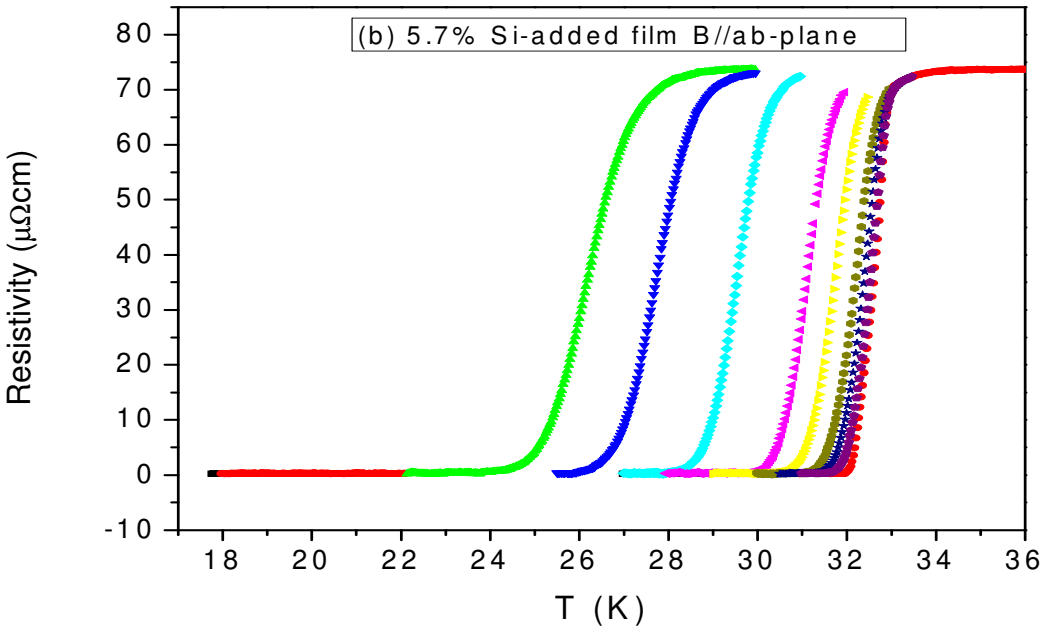
(b) 5.7% Si-added film B//ab-plane
Resistivity (μΩcm)
T (K)
80
70
60
50
40
30
20
10
0
-10
18
20
22
24
26
28
30
32
34
36

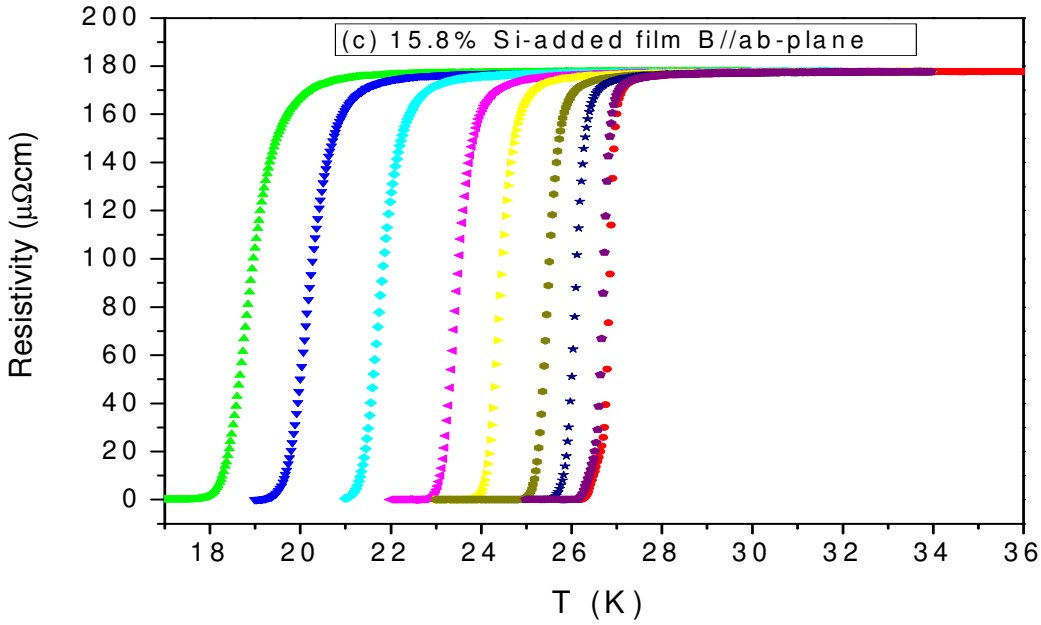

Fig. 6-7 The resistivity versus temperature curves for (a) *0% Si,* (b) *5.7%, and* (c) *15.8% Si-added films in fields parallel to the ab-plane* (*from right to left 0T, 0.1T, 0.5T, 1T, 2T, 3T, 5T, 7T and 8.7 T*).

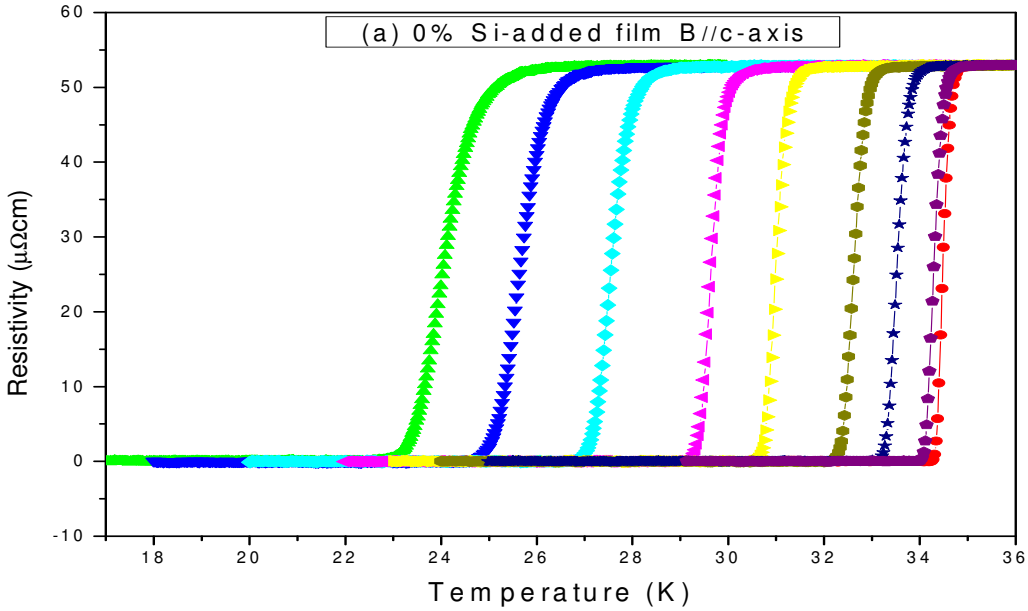
(a) 0% Si-added film B//c-axis
Resistivity (μΩcm)
Temperature (K)
60
50
40
30
20
10
0
-10
18
20
22
24
26
28
30
32
34
36

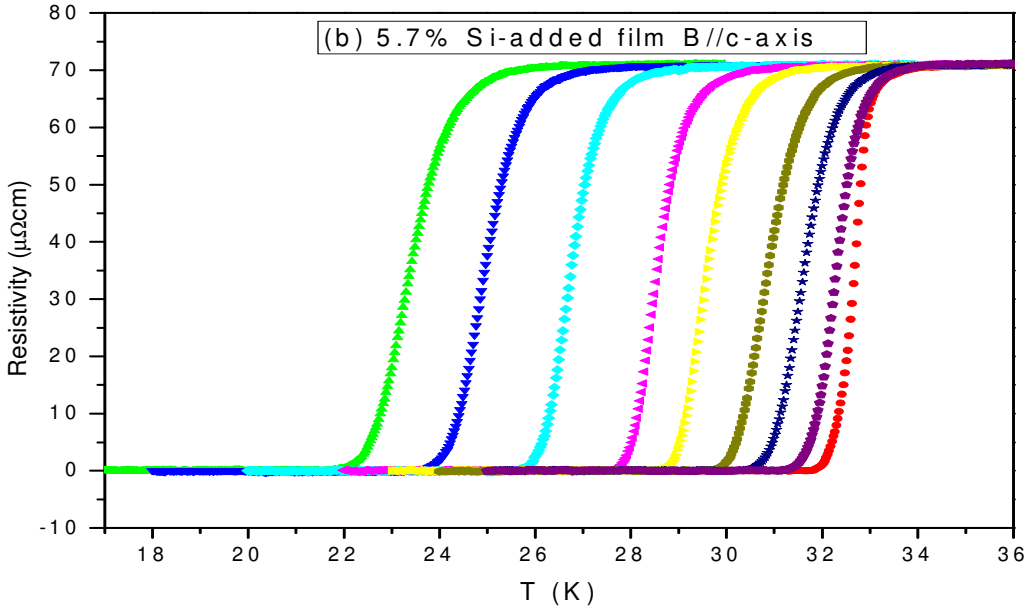
(b) 5.7% Si-added film B//c-axis
Resistivity (μΩcm)
T (K)
80
70
60
50
40
30
20
10
0
-10
18
20
22
24
26
28
30
32
34
36

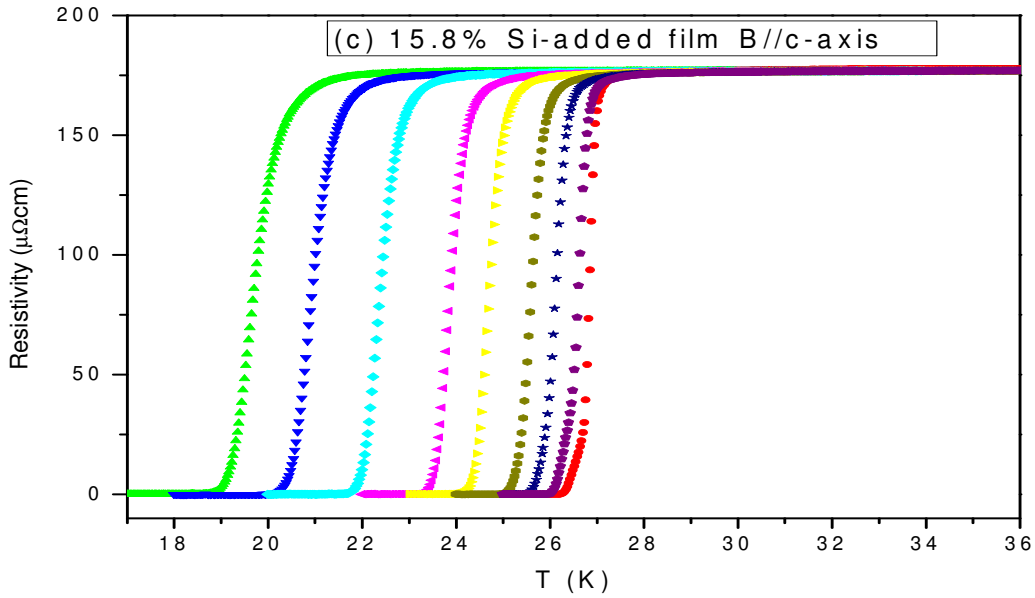

Fig. 6-8 The resistivity versus temperature curves for (a) *0% Si,* (b) *5.7%, and* (c) *15.8% Si-added films in fields perpendicular to the ab-plane* (*from right to left 0T, 0.1T, 0.5T, 1T, 2T, 3T, 5T, 7T and 8.7 T*).

The temperature dependence of the resistivity of the three films (0% Si, 5.7% Si, and 15.8% Si) in 0 to 8.7T applied fields is shown in Figures 6-7 and 6-8. The resisitivity T_c of the 5.7% Si-added film in zero field is slightly suppressed by ~2K compared with the 0% Si MgB_2 film. For the case of the field parallel to the *ab*-plane in Fig. 6-7, it can be clearly seen that the $T_{c\ onset}$ values in high fields are up-shifted for the 5.7% Si-added sample. In the perpendicular field condition (Fig. 6-8), the T_c values of 5.7% Si added film in high fields are similar to the 0% Si film, indicating better pinning in parallel applied fields. The whole set of data has slid down to lower T_c for the 15.8% Si-added sample in both cases. This may indicate that the irreversibility field H_{irr} was enhanced by the selective 5.7% Si addition but higher level of Si addition (15.8%)

suppressed the T_c severely due to the introduction of a greater volume of non-superconducting phase. The anisotropy of the 5.7% Si-added films is larger than the 0% Si-added film. Usually additions by different elements will increase the level of scattering and reduce the anisotropy of the MgB_2, making it a single gap superconductor, but in our case the Si addition may enhanced the crystallization of MgB_2 [10] and caused the film more two-gap featured, closer to that of single crystal.

The increase in normal state resistivity with Si content can be attributed to the reduction of effective current carrying area or an increased defect level in the Si-added film. The residual resistivity ratio RRR ($\rho_{297\text{-}40K}$) for all the samples is about at the same level from 1.05 to 1.2, but the room temperature resistivity values of our Si added films ρ_{297K} ~ 80 to 300 μΩcm are on an intermediate level for MgB_2 [11], indicating that the level of disorder inside the MgB_2 grains is high probably due to the existence of other defects.

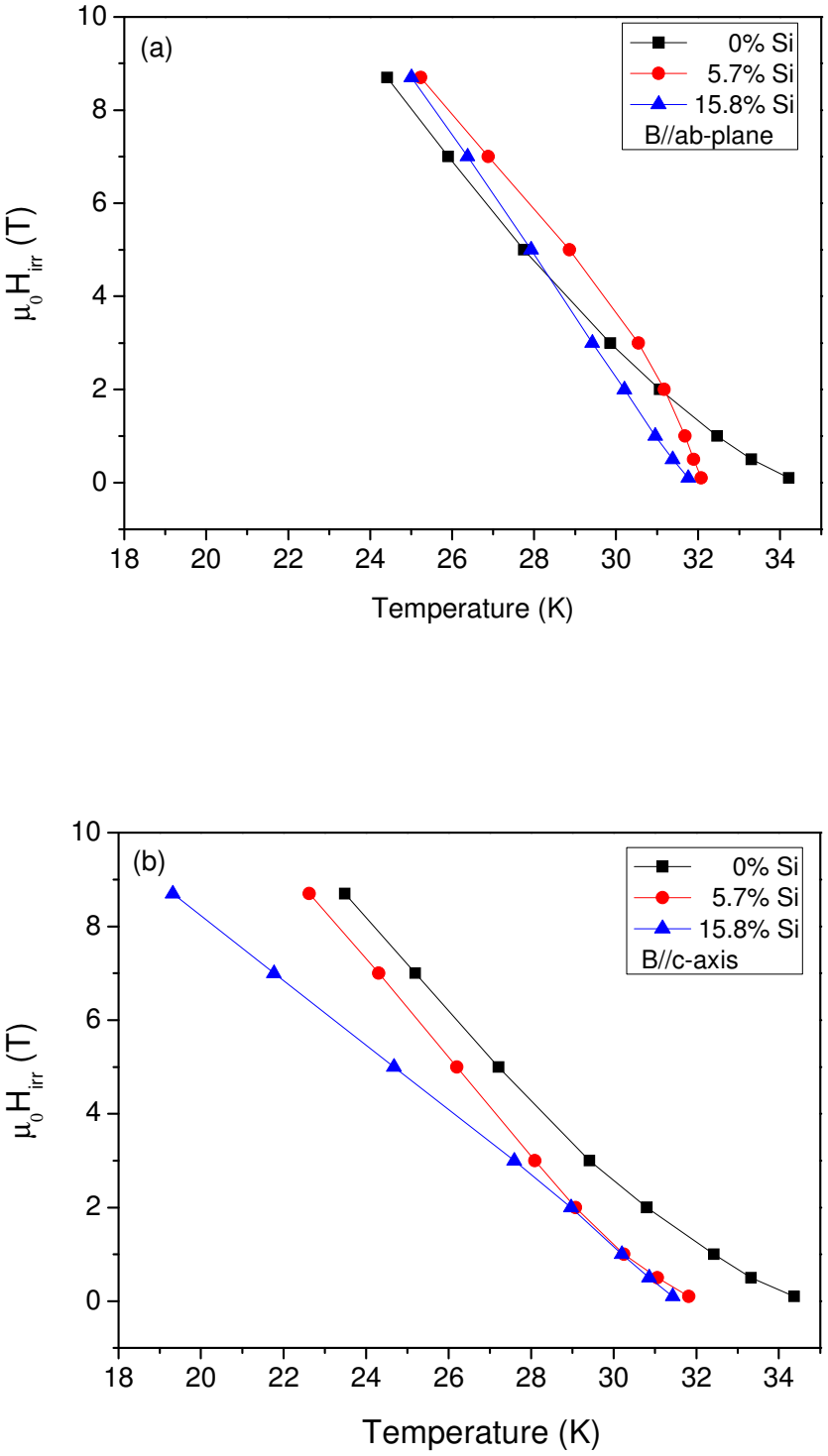

Fig. 6-9 The irreversibility fields of the pure and Si-added MgB_2 films in both (a) *fields parallel to the ab-plane, and* (b) *fields perpendicular to the ab-plane.*

The irreversibility fields of the Si-added and pure MgB_2 films are shown in Figure 6-9, using the 10% $\rho(T_c)$ values in the transport *R-T* curves. In the *H//ab* condition, the H_{irr} values of the selective 5.7% Si-added films are clearly higher, indicating some enhancement of pinning by the Si. However, it's observed that in the field perpendicular case the difference in H_{irr} is a lot reduced. This once again indicates that the anisotropy in the Si-added films is higher.

The observation of this 2D behaviour of the irreversible field H_{irr} can be explained with the geometrical factor of the films. Our Si-added MgB_2 films were prepared by alternate deposition of MgB_2 and Si layers, although the thin Si interlayers usually break during the high temperature sintering process, the defects therein like Mg_2Si which can act as the pinning centres are considered to have two-dimensional structure and the pinning properties are different in both applied field directions. The flux is easier to move in the perpendicular field case due to short flux thread and immense space, and vice versa in the parallel case. In our pure MgB_2 film the pinning is mainly attributed to the fine grains and high level of disorder, thus the 2D geometrical factor is not obvious. But in the Si-added films, the major volume is occupied by larger grains, the pinning force should consequently be lower. The geometrical factor then plays an important role in the H_{irr} behaviour.

Moreover, the Mg_2Si layers typically have thickness of a few nm in the *c*-axis, of the same order as $\xi_{ab}(0)$ of pure MgB_2, the decoupling of vortices is relatively strong when the field is in the *c*-axis direction [12, 13]. So the H_{irr} values at different fields are suppressed in the perpendicular case. However, when the field is applied parallel

to the *ab*-plane, the vortices are probably trapped in these non-superconducting Mg_2Si, providing strong flux pinning. The 2D behaviour of H_{irr} thus becomes obvious.

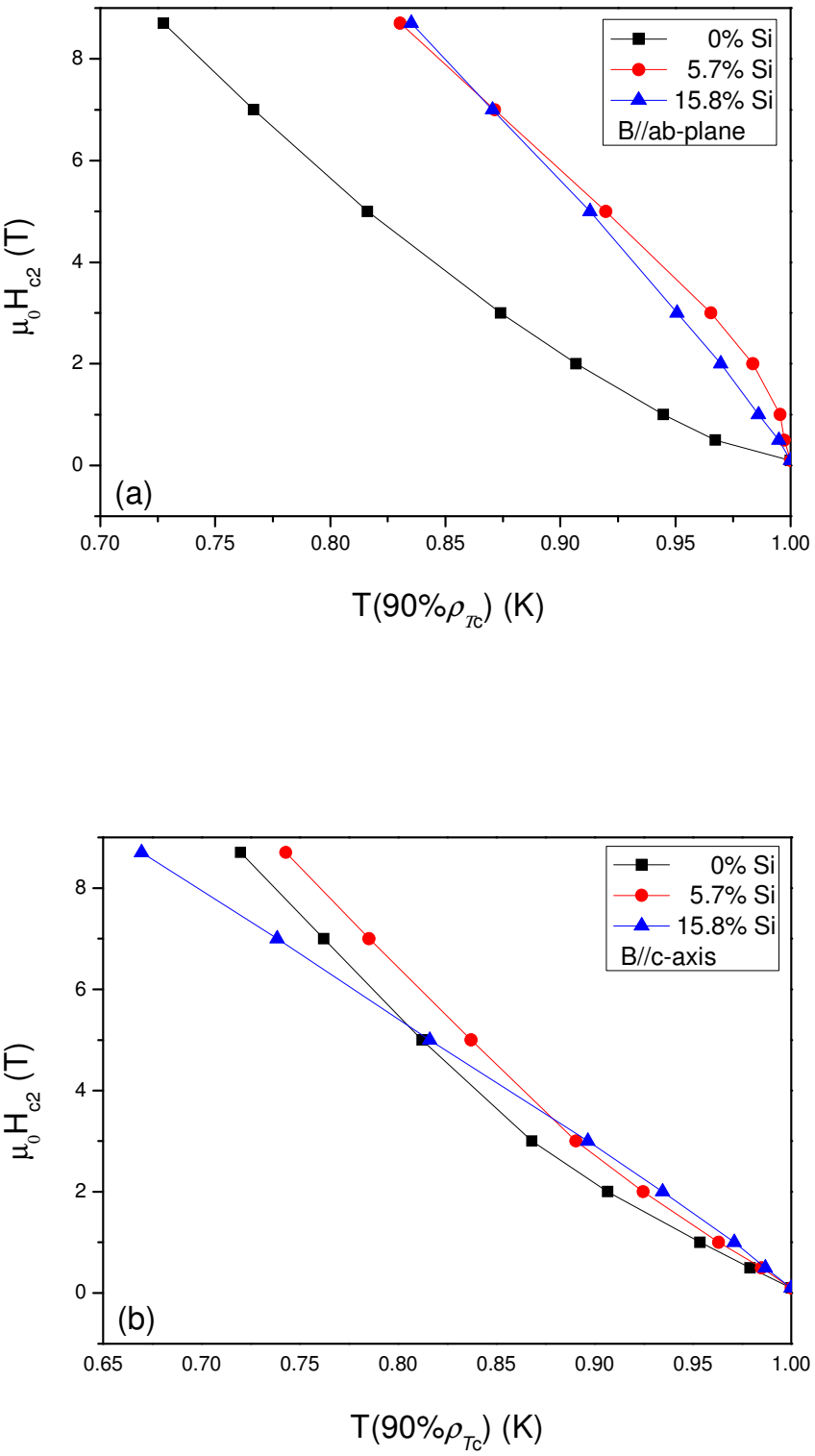

Fig. 6-10 The upper critical fields of the pure and Si-added MgB_2 films in fields both (a) *parallel and* (b) *perpendicular to the ab-plane.*

We observed a similar trend in the $H_{c2}(T)$ curves of the films. The increase in the $H_{c2}(T)$ values for the Si-added films in the parallel field case may indicate some degree of enhancement of the intra-band scattering. This scattering may come from other imperfections in the lattice planes or Mg vacancies introduced by the Si addition. Based on the equations derived from GL theory for dirty limit in chapter 1, the parameter $a(T) \approx a_0[(T/T_c)-1]$ varies approximately linear with temperature for $T \leq T_c$ in superconducting state, $|a(T)|$ decreases as the temperature approaches T_c, and $\xi(T)$ increases as $\xi(T) = [\hbar^2/2m^* |a(T)|]^{1/2} \sim |a(T)|^{-1/2}$. However, in the parallel field case, the scattering effect could raised the resistivity ρ and also reduced the coherence length $\xi(T)$ by shortening the electronic mean free path l_e of the cooper electrons, the $H_{c2}(T)$ was then increased as $\xi(T) = [\Phi_0/2\pi H_{c2}(T)]^{1/2} \sim H_{c2}(T)^{-1/2}$.

We again used the linear approximation $H_{c2}(0) = [dH_{c2}/dT]T_c$, for T below but near T_c, to evaluate the upper critical field at 0K. The values $H_{c2}(0)$ extrapolated in parallel field for 0%, 5.7% and 15.8% Si-added films are 35.5T, 50.3T and 53.1T respectively. Estimation of the electronic mean free paths at zero temperature using the GL equations, $\xi(T) = 0.855(\xi_0 l_e)^{1/2}/[1-T/T_c]^{1/2}$ and $\xi(0) = 0.855(\xi_0 l_e)^{1/2} = [\Phi_0/2\pi H_{c2}(0)]^{1/2}$ and by taking the single crystal $\xi_0 \sim 6.0$nm gives $\xi(0) \approx$ 3nm, 2.6nm & 2.5nm and $l_e \approx$ 2.1nm, 1.5nm & 1.4nm for 0%, 5.7% and 15.8% Si-added films respectively.

Conclusion

MgB_2 thin films with selective amounts of Si addition were tested. We found that small improvements in the field dependence of J_c could be obtained by a moderate amount of 5.7% Si addition. This could be due to the increased H_{c2} at low temperature and some enhanced flux pinning from the presence of Mg_2Si phases, which act as pinning centres in addition to the grain boundaries. Both the T_c value and the J_c value of the Si-added films are lower than the pure MgB_2 film in this work. An enhanced anisotropy H_{irr} is also observed in the Si-added film. The work has shown that the possibility to increase effective flux pinning and optimal J_c improvement with small Si additions should not be ruled out.

Reference

[1] A Gurevich, S Patnaik, V Braccini, K H Kim, C Mielke, X Song, L D Cooley, S D Bu, D M Kim, J H Choi, L J Belenky, J Giencke, M K Lee, W Tian, X Q Pan, A Siri, E E Hellstrom, C B Eom, and D. C. Larbalestier, "Very high upper critical fields in MgB_2 produced by selective tuning of impurity scattering," *Supercond. Sci. Technol. ,* vol. 17 pp. 278–286, 2004.

[2] S. Li, T. White, K. Laursen, T. T. Tan, C. Q. Sun, Z. L. Dong, Y. Li, S. H. Zho, J. Horvat, and S. X. Dou, "Intense vortex pinning enhanced by semicrystalline defect traps in self-aligned nanostructured MgB_2," *APPLIED PHYSICS LETTERS,* vol. 83, pp. 314-316, 2003.

[3] S. X. Dou, S. Soltanian, J. Horvat, X. L. Wang, S. H. Zhou, M. Ionescu, H. K. Liu, P. Munroe, and M. Tomsic, "Enhancement of the critical current density and flux pinning of MgB_2 superconductor by nanoparticle SiC doping," *APPLIED PHYSICS LETTERS,* vol. 81, pp. 3419-3421, 2002.

[4] Sergey Lee *, Takahiko Masui, Ayako Yamamoto, Hiroshi Uchiyama, and S. Tajima, "Crystal growth of C-doped MgB_2 superconductors: accidental doping and inhomogeneity," *Physica C* vol. 412–414 pp. 31–35, 2004.

[5] X.L. Wang*, S. Soltanian, M. James, M.J. Qin, J. Horvat, Q.W. Yao, H.K. Liu, and S. X. Dou, "Significant enhancement of critical current density and flux pinning in MgB_2 with nano-SiC, Si, and C doping," *Physica C,* vol. 408–410, pp. 63–67, 2004.

[6] Y Zhao, M Ionescu, J Horvat, A H Li, and S. X. Dou, "Si addition in in situ annealed MgB_2 thin films by pulsed laser deposition," *Supercond. Sci. Technol. ,* vol. 17 pp. 1247–1252, 2004.

[7] Y. Zhao, S. X. Dou, M. Ionescu, and P. Munroe, "Significant improvement of activation energy in MgB_2/Mg_2Si multilayer films," *APPLIED PHYSICS LETTERS* vol. 88, 2006.

[8] Y. Zhao, M. J. Qin, S. X. Dou, M. Ionescu, and P. Munroe, "Transport properties of multilayered MgB_2/Mg_2Si superconducting thin film," *JOURNAL OF APPLIED PHYSICS,* vol. 99, 2006.

[9] Yue Zhao, Mihail Ionescu, J. Horvat, and S. X. Dou, "Off-axis MgB_2 films using an *in situ* annealing pulsed laser deposition method," *Supercond. Sci. Technol.,* vol. 18, pp. 395–399, 2005.

[10] L D Cooley, Kyongha Kang, R F Klie, Qiang Li, A M Moodenbaugh, and R. L. Sabatini, "Formation of MgB_2 at low temperatures by reaction of Mg with B_6Si," *Supercond. Sci. Technol. ,* vol. 17, pp. 942–946, 2004.

[11] J. M. Rowell, "The widely variable resistivity of MgB_2 samples," *Supercond. Sci. Technol.,* vol. 16, pp. R17-R27, 2003.

[12] J. R. Clem, "Anisotropy and two-dimensional behaviour in the high-temperature superconductors," *Supercond. Sci. Technol. ,* vol. 11 pp. 909–914, 1998.

[13] J. L. Martin, M. Velez, and J. L. Vicent, "Multilayer pinning in *a*-axis-oriented $EuBa_2Cu_3O_7/PrBa_2Cu_3O_7$ superconducting superlattices," *Phys. Rev. B,* vol. 52, pp. R3872-R3875, 1995.

Summary

In this thesis, we studied *in situ* MgB_2 thin film produced by an off-axis pulsed laser deposition (PLD) synthesis technique. Highly smooth and *c*-axis oriented superconducting MgB_2 thin films were successfully prepared and tested with a view to future applications in superconducting electronics for this new binary superconducting compound. In each experiment, deposition was carried out in an optimized 120 mTorr high purity Ar background gas and was then followed by an *in situ* annealing process in a 760 Torr Ar atmosphere. The effect of *in situ* annealing conditions on pulsed laser deposited MgB_2 films was investigated. It was found that the superconducting properties depend in a crucial way on the annealing conditions.

The T_c dependence of the *in situ* annealed MgB_2 films was tested by changing various process parameters: background gas, annealing temperatures, and dwell times. High T_c was generally obtained for films with short dwell times. But the XRD θ-2θ scans of these films show fairly good crystallization, according to the clear *c*-axis oriented peaks for the films. The optimized film processing conditions were determined, and good quality *in situ* films were obtained with reproducibility. The films without annealing show no superconductivity.

The J_c-H curves of the *in situ* films were obtained using the hysteresis loops of magnetic moment versus applied field at different temperatures, by assuming homogeneous magnetic flux penetration. This observation shows that the J_c has weak field dependence in high fields. The overall J_c properties of our high T_c *in situ*

annealed film are good and are derived from the good inter-grain connectivity combined with strong pinning.

The zero resistance T_c value of the best off-axis film reached 34.3 K, with a narrow transition width of 0.2 K. The films showed almost no anisotropy in H_{c2}-T curves, when parallel and perpendicular fields were applied relative to the film surface. The slope of the H_{c2}-T curves is ~1 T/K, which is still among the highest reported values.

A large slope of the H_{c2}-T curve was obtained for the *in situ* annealed film, and the H_{c2} anisotropy was comparatively small, indicating quite intense scattering. The microstructural differences in our films were observed by XRD and TEM. The small grain (<60nm) size and particular level of impurities detected in the *in situ* annealed MgB_2 films are decisive for the significant improvement of J_c and H_{c2}.

In order to enhance the performance of the MgB_2 films, different amounts of Si were added into MgB_2 thin films by sequential laser ablation of a stoichiometric MgB_2 target and a Si target. The T_cs of the Si added MgB_2 thin films were lower than for the normal un-doped MgB_2 film. For the ~5.7wt% Si addition, the field dependence of the magnetic J_c was found to be slightly lower compared to the un-doped film. The slopes of the H_{irr}(T) and H_{c2}(T) curves of the 5.7wt% Si-added MgB_2 film were higher than for the un-doped film. The residual resistivity ratios are 1.05 and 1.2 for the un-doped and 5.7wt% Si films, respectively. The field dependence of the resistivity-temperature curves was measured, and the transition width was increased for the 5.7wt% Si film, due to the increase in non-superconducting volume.

With the aid of the off-axis PLD method established by this work, we have fabricated MgB_2 (or Si-added) thin films with fine and homogeneous crystal structure. The combined high qualities of our off-axis films, namely good T_c value, improved J_c performance in high fields, high H_{c2}-T slope of ~1 T/K, and high degree of surface smoothness, represent a step forward in the process of incorporating the MgB_2 superconducting thin films into electronic devices.

Publication list

Refereed Papers:

[1] Y. Zhao, Y. Wu, S. X. Dou, T. Tajima, and O. S. Romanenko, "Deposition of MgB_2 Thin Films on Nb Substrates Using an in situ Annealing PLD Method," *Materials Science Forum*, vol. 546-549, pp. 2027-2030, 2007.

[2] Y. Zhao, Y. S. Wu, C. Kong, D. Wexler, M. Vos, M. Went, and S. X. Dou, "Phase Evolution in PLD MgB_2 Films During the In situ Annealing Process," *Supercond. Sci. Technol.*, 20, S468-S471, 2007.

[3] Y. S. Wu, Y. Zhao, D. Wexler, and S. X. Dou, "Optimization of in situ MgB_2 films using the off-axis PLD method with different annealing conditions" accepted by *Physica C*.

Conference:

[1] M. Went, M. Vos, Y. Zhao, Y. Wu, and S. X. Dou, "Electron Rutherford Backscattering as a surface analytical tool: A case study of MgB_2 films," presented at 31st Condensed Matter and Materials Meeting, Wagga Wagga, NSW, Australia, Feb. 2007.

[2] Y. S. Wu, Y. Zhao, S. X. Dou, “Optimization of annealing conditions of off-axis PLD MgB_2 films” presented at Annual Student Open-Day, University of Wollongong, Australia, 2006.